

OPTICALLY ACTIVE PHONONS AND ELECTRONIC
TRANSITIONS IN RARE-EARTH TRI-FLUORIDES

by

JOHN FREDERIC PARRISH

B.S. Loyola University of Los Angeles
(1964)

S.M. Massachusetts Institute of Technology
(1967)

SUBMITTED IN PARTIAL FULFILLMENT

OF THE REQUIREMENTS FOR THE

DEGREE OF DOCTOR OF

PHILOSOPHY

at the

MASSACHUSETTS INSTITUTE OF

TECHNOLOGY

i.e. FEB. 1970
(October, 1969)

Signature redacted

Signature of Author.
Department of Physics, October 3, 1969

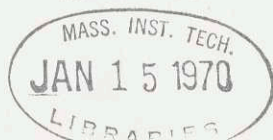
Signature redacted

Certified by
Thesis Supervisor

Signature redacted

Accepted by
Chairman, Departmental Committee
on Graduate Students

Archives



OPTICALLY ACTIVE PHONONS AND ELECTRONIC
TRANSITIONS IN RARE-EARTH TRI-FLUORIDES

John Frederic Parrish

Submitted to the Department of Physics, October 3,
1969 in partial fulfillment of the requirements for
the degree of doctor of philosophy

ABSTRACT

The frequencies of the principal poles and zeros of the far infrared, anisotropic dielectric response functions of the four lightest tysonite lanthanide fluorides have been calculated from the polarized, far infrared reflectance spectra of single crystals of LaF_3 , CeF_3 , PrF_3 , and NdF_3 measured from 30 cm^{-1} to 600 cm^{-1} at room temperature and near the boiling points of liquid nitrogen and helium. Low temperature (liquid helium) transmittance spectra of these same materials, some doped with other lanthanide ions, have also been measured. Four different electronic transitions are observed below 100 cm^{-1} for Pr^{3+} , Nd^{3+} , and Er^{3+} ions in the tysonite host lattices. The electronic transitions of Nd^{3+} and Er^{3+} are associated with Kramers doublets and have been Zeeman split in magnetic fields up to 70 kilogauss.

The group theoretical properties of the far infrared lattice and electronic spectra are approximated fairly well by a hexagonal $P6_3/mcm$ (D_{6h}^3) structure in which the lanthanide ions occupy six sites with mm (C_{2v}) point group symmetry. The exact selection rules are most consistent with a trigonal-hexagonal $P\bar{3}c1$ (D_{3d}^4) structure in which the lanthanide ions occupy six sites with 2 (C_2) point group symmetry. The reported magnetic resonance measurements can be reconciled with the trigonal $P\bar{3}c1$ space group by assuming that the samples are twinned.

Spurious effects are measurable in the nominally π -polarized reflectance and transmittance spectra due to a slight misalignment of the optic axis with respect to the propagation vector. One of these effects allows strong LO (longitudinal optic) resonances of the dielectric response functions to be studied in transmission as if they were weak TO (transverse optic) resonances in the orthogonal component of the dielectric response tensor.

Thesis Supervisor: Clive Howe Perry
Title: formerly Assistant Professor of Physics (M.I.T.)
presently Associate Professor of Physics (Northeastern
University)

ACKNOWLEDGEMENTS

The author is grateful to Professor Clive H. Perry for suggesting this topic and guiding the work to completion.

Special thanks are extended to Professor Robert P. Lowndes for sharing his experimental measurements and interpretations. Professors Perry and Lowndes and the other members of the Solid State Spectroscopy Group, Dr. Jeanne H. Fertel, Dr. Eugene F. Young, Dirk J. Muehlner, and Neal E. Tornberg, have made an invaluable, indirect contribution to this work during the many hours of mutually enlightening discussions.

The author was assisted by Richard W. Stimets in the use of the facilities of the Francis Bitter National Magnet Laboratory, M.I.T., which were generously offered by Professor Benjamin Lax and Kenneth J. Button. Professor Richard C. Lord has shown interest in this work and is Director of the Spectroscopy Laboratory, M.I.T., in which most of the experimental measurements were taken. The facilities of the Research Laboratory of Electronics, M.I.T., the Center for Materials Science and Engineering, M.I.T., and the Department of Physics, Northeastern University were also of great value.

Materials and technical support were provided in part by the Joint Services Electronics Program (Contract No. DA 28-043-AMC 02536(E)), NASA (Grant No. NGR 22-009-(237)), and the U.S. Air Force (ESD Contract AF 19(628)-6066). Personal support was

provided by a National Science Foundation graduate fellowship from September 1964 to September 1968. From September 1968 to September 1969 the Department of Physics, M.I.T., provided partial scholarship support.

Even with such valuable assistance, however, it would have been difficult to complete this work without the loving encouragement and emotional support received from Miss Donna M. Connolly. For the continuing encouragement and financial assistance received from them during the many years of his education, the author is especially grateful to his parents.

1.1	The Debye-Hückel-Hellmuth Function	10
1.2	Direct-Current Analysis	11
1.3	Classical Oscillation Systems	12
1.4	Nonlinear Oscillation Systems	13
CHAPTER II THE ELECTROMAGNETIC FIELD		14
2.1	General Properties of Electromagnetic Fields	15
2.2	Energy and Momentum in Electromagnetic Fields	16
2.3	Wave Propagation of Light with Anisotropic Media	17
2.4	Reflection and Refraction at an Interface between Two Media	18
2.5	Interference and Diffraction of Light	19
2.6	The Lorentz Force	20
CHAPTER III MECHANICS OF POINT PARTICLES		21
3.1	The Lagrangian Formalism	22
3.2	The Hamiltonian Formalism	23
3.3	Canonical Transformations	24
3.4	Small Oscillations	25
3.5	Relativistic Mechanics	26
3.6	Scattering of Particles	27
3.7	Angular Momentum	28

TABLE OF CONTENTS

	<u>Page</u>
ABSTRACT	ii
ACKNOWLEDGEMENTS	iii
LIST OF FIGURES	vii
LIST OF TABLES	ix
CHAPTER I INTRODUCTION	1
CHAPTER II EXPERIMENTAL AND THEORETICAL TECHNIQUES	6
2.1 Spectroscopy Laboratory: Instrumentation	6
2.2 Francis Bitter National Magnet Laboratory: Instrumentation	16
2.3 The Dielectric Response Function	19
2.4 Kramers-Kronig Analysis	28
2.5 Classical Oscillator Synthesis	31
2.6 Measuring Uniaxial Dielectric Response	36
CHAPTER III THE TYSONITE LATTICE	45
3.1 General Physical Properties	45
3.2 X-ray and Neutron Diffraction	48
3.3 Bragg Diffraction of Light from Accoustic Phonons	50
3.4 Infrared and Raman Activity due to Optical Phonons: Previous Studies	52
3.5 Infrared Activity due to Optical Phonons: Current Study	56
3.6 The Lattice Space Group	81
CHAPTER IV LANTHANIDE IONS IN TYSONITE	94
4.1 The Rare Earths	94
4.2 Crystal Field Splitting	101
4.3 Far Infrared Stark Levels: Experimental Survey	106
4.4 Paramagnetic Rotation	110
4.5 EPR and NMR	113
4.6 Infrared Spectra: A Literature Survey	117
4.7 Polarized Far Infrared Spectra	122

Table of Contents (continued)

	<u>Page</u>
4.8 Far Infrared Zeeman Splitting	142
4.9 Lanthanide Site in the Tysonite Space Group	152
CHAPTER V SUMMARY	160
REFERENCES	168
BIOGRAPHICAL NOTE	176
1.1 Lanthanide contraction of the crystal field splitting	27
1.2 Spectroscopic symbols of f^n in SO_4 , $7F_4$, and $7F_2$ in the D-symmetry	30
1.3 Low temperature crystal field spectroscopy of LaF_3 , CaF_2 , PrF_3 and SmF_3	32
1.4 High resolution spectroscopy of LaF_3 at La^{3+} , $7F_4$, and $7F_2$ in the D-symmetry	38
1.5 Low temperature crystal field spectroscopy of LaF_3 , PrF_3 , SmF_3 , and EuF_3	44
1.6 Low temperature crystal field spectroscopy of LaF_3	74
1.7 Low temperature crystal field spectroscopy of CaF_2	78
1.8 High resolution spectroscopy of LaF_3 at La^{3+} , $7F_4$, $7F_2$, and $7F_0$	87
1.9 Nonlinear optical properties of LaF_3 (127)	90
CHAPTER IV. LANTHANIDE IONS IN TYSONITE	
4.1 f^n crystal field splitting in LaF_3 , CaF_2 , PrF_3 , and SmF_3	104
4.2 f^n crystal field splitting in LaF_3 , PrF_3 , SmF_3 , and EuF_3	108

LIST OF FIGURES

	<u>Page</u>
CHAPTER II EXPERIMENTAL AND THEORETICAL TECHNIQUES	
2.1 Plan view of the modified FS-520 Fourier spectrophotometer	8
2.2 Relative efficiencies of mylar beam splitters as a function of frequency and thickness	11
2.3 Block diagram of the Fourier spectroscopy data processing system	15
2.4 Infrared active TO and LO frequency locators for NdF_3 reflectance spectra	39
CHAPTER III THE TYSONITE LATTICE	
3.1 Lanthanide contraction of the tri-fluorides	47
3.2 Reflectance spectra of LaF_3 at 290°K , 78°K , and 7°K in the π -polarization	59
3.3 Low temperature π -polarized reflectance spectra of LaF_3 , CeF_3 , PrF_3 and NdF_3	62
3.4 Reflectance spectra of LaF_3 at 290°K , 78°K , and 7°K in the σ -polarization	65
3.5 Low temperature σ -polarized reflectance spectra of LaF_3 , CeF_3 , PrF_3 , and NdF_3	68
3.6 Low temperature absorption coefficient spectra of LaF_3	76
3.7 Low temperature absorption coefficient spectra of CeF_3	78
3.8 Plan view of the $\overline{\text{P}3\text{c}1}$ structure proposed for tysonite. ⁽⁵⁴⁾	87
3.9 Bimolecular pseudocell of tysonite. ⁽³³⁾	90
CHAPTER IV LANTHANIDE IONS IN TYSONITE	
4.1 Nd^{3+} electronic transition in LaF_3 , CeF_3 , PrF_3 , and NdF_3	126
4.2 Er^{3+} electronic transition in LaF_3 , CeF_3 , PrF_3 , and NdF_3	132

List of Figures (Continued)

	<u>Page</u>
4.3 Pr ³⁺ electronic transitions in LaF ₃ , CeF ₃ , PrF ₃ , and NdF ₃	136
4.4 Low temperature absorption coefficient spectra of PrF ₃	140
4.5 Zeeman spectra of Nd ³⁺ electronic transition in LaF ₃	145
4.6 Zeeman splitting of Er ³⁺ electronic transition in LaF ₃	149
4.7 Magnetic ordering permitted in the P $\bar{3}$ cl and P $\bar{3}$ 'c'l magnetic space groups	158
CHAPTER V SUMMARY	
5.1 Frequencies of the Pr ³⁺ , Nd ³⁺ , and Er ³⁺ electronic transitions below 100 cm ⁻¹ as a function of the tysonite host lattice	165

LIST OF TABLES

	<u>Page</u>
 CHAPTER III THE TYSONITE LATTICE	
3.1	Poles and Zeros of the π -polarized dielectric response function-- A_{2u} lattice vibrations of the four lightest tysonite lanthanide fluorides 63
3.2	Poles and zeros of the σ -polarized dielectric response function-- E_u lattice vibrations of the four lightest tysonite lanthanide fluorides. 70
3.3	Miscellaneous features of the dielectric response functions of the four lightest tysonite lanthanide fluorides 72
3.4	Number of optically active phonons in the proposed tysonite lattices 83
 CHAPTER IV LANTHANIDE IONS IN TYSONITE	
4.1	Group properties of the f^n configurations 98
4.2	Predicted low energy Stark levels in tysonite 121
4.3	Nd^{3+} electronic transition in LaF_3 , CeF_3 , PrF_3 , and NdF_3 127
4.4	Er^{3+} electronic transition in LaF_3 , CeF_3 , PrF_3 , and NdF_3 133
4.5	Pr^{3+} electronic transitions in LaF_3 , CeF_3 , PrF_3 , NdF_3 137
4.6	Permitted polarizations of electronic transitions at the lanthanide sites in the proposed tysonite lattices 153
4.7	Group properties of the $P3c1$ magnetic space groups 156

CHAPTER I

INTRODUCTION

The partially filled 4f electron shell of the lanthanide (rare-earth) elements is so well screened from its external environment that, when the ions are held in a suitable host lattice, electronic transitions of the type $4f \rightarrow 4f$ are expected to give sharp spectral lines. Moreover, some of the known $4f \rightarrow 4f$ transitions lie within the far infrared region of the spectrum. Consequently, there is currently strong motivation to assess the potential of these low energy transitions for use in solid state, far infrared lasers.

Laser transitions have been observed in the near infrared region of the spectrum between the LSJ levels of trivalent lanthanide ions in tysonite lattices,^(1,2) and the tysonite lanthanide fluorides appear to have great potential as solid state laser hosts. The materials are hard to scratch,⁽³⁾ are insoluble in most common reagents,^(3,4) have a thermal expansion coefficient close to that of pure copper,⁽⁴⁾ have a volumetric concentration of lanthanide ions almost as high as in the pure metals, and have several other physical properties which are desirable and convenient. Moreover, although not all of the lanthanide fluorides crystallize in the form of tysonite, up to at least one mole percent of any of the lanthanide ions may be substitutionally contained within the tysonite lattice of one of the four lightest

lanthanide fluorides.⁽⁵⁾ Unfortunately the precise crystal structure of tysonite has been in considerable dispute and only a very few of the critical lattice frequencies have been unambiguously identified, in spite of the many near infrared spectra reported for lanthanide ions in tysonite lattices.

Therefore, now that reasonably large single crystals of the four lightest tysonite lanthanide fluorides are available, the far infrared anisotropic dielectric properties of LaF_3 , CeF_3 , PrF_3 , and NdF_3 have been studied and are reported herein. Most of the strong features of the far infrared dielectric response can be explained in terms of the infrared active fundamental phonon modes of the proposed $\overline{\text{P3cl}} (\text{D}_{3d}^4)$ crystal structure. Others are associated with infrared active electronic transitions of the lanthanide ions in a host lattice. However, several features have been observed which can not be explained in terms of any ordinary first order electromagnetic interactions. Some of these require a slight reformulation of the traditional description of the experimentally measured, first order dielectric properties of anisotropic crystals, whereas others can be explained in terms of second order phonon-phonon and electron-phonon interactions. Several explanations are proposed to account for the reported magnetic resonance results which are at variance with the proposed $\overline{\text{P3cl}}$ crystal structure.

All of the far infrared spectra reported in this thesis were observed by means of Michelson interferometry and reduced to

physical parameters by conventional theoretical techniques of solid state spectroscopy. The instrumentation used at the Spectroscopy Laboratory and the Francis Bitter National Magnet Laboratory are described in the first two sections of Chapter II. Then, the dielectric response function, $\epsilon(\omega)$, is discussed in detail in order to delimit its applicability and to determine its most useful and characteristic parameters. These parameters are also related to the principle theoretical techniques of Kramers-Kronig analysis and classical oscillator synthesis. Finally, a discussion of the special experimental and theoretical problems associated with measuring the dielectric response tensor of uniaxial crystals reveals a weak coupling of the nominally transverse material electromagnetic wave (mixed photon-phonon particle wave) to the longitudinal optic (LO) frequencies of the orthogonal components of the dielectric response tensor. Although it is a general property of all strongly anisotropic crystals, apparently this effect has not been previously reported.

Chapter III considers the macroscopic properties of the four lightest lanthanide fluorides which depend upon averages over many unit cells of the tysonite lattice. The first four sections review the published data on the general physical properties, X-ray and neutron diffraction, velocity of sound, Raman scattering, and infrared dielectric properties of the tysonite lanthanide fluorides. The next section displays the current far

infrared dielectric properties of oriented samples of LaF_3 , CeF_3 , PrF_3 , and NdF_3 at room temperature, liquid nitrogen temperature, and liquid helium temperature. Spurious experimental effects are identified which are due to the special problems associated with the measurement of the dielectric response tensor of uniaxial crystals, and the infrared and Raman results are related to the group theoretical properties of the lattice space group of tysonite. The $\overline{\text{P3c1}} (D_{3d}^4)$ lattice space group seems to be the most consistent with the macroscopic electric and mechanical properties of the four lightest tysonite lanthanide fluorides.

The microscopic electric and magnetic properties and the point group symmetry of the atomic sites of the tysonite space-group are considered in Chapter IV. Five sections are necessary to discuss the significant research which has been done previously. Unfortunately, an ab initio calculation is not yet possible for the crystal field splitting of the LSJ levels of the 4f electrons. Nevertheless, an experimental survey reveals three far infrared (below 100 cm^{-1}) electronic transitions for praseodymium, neodymium, and erbium in a lanthanum trifluoride host lattice. Based upon this survey and the published near infrared spectra of other lanthanide ions in tysonite, polarized far infrared spectra have been observed and are reported herein for Ce^{3+} (LaF_3 only), Pr^{3+} , Nd^{3+} , Sm^{3+} (LaF_3 only), and Er^{3+} in the four lightest tysonite lanthanide fluorides. Zeeman split electronic spectra in magnetic fields up to seventy kilogauss

are reported for Nd^{3+} and Er^{3+} in LaF_3 . The current experimental measurements and much of the published data tend to support the trigonal $\bar{P}3c1$ space group for which the lanthanide ion occupies a site with C_2 point group symmetry which is closely approximated by a twisted C_{2v} site. The apparent hexagonal symmetry observed in magnetic resonance experiments can be most easily explained by a multiply twinned $\bar{P}3c1$ structure. The final chapter summarizes the conclusions of this thesis.

CHAPTER II

EXPERIMENTAL AND THEORETICAL TECHNIQUES

2.1 Spectroscopy Laboratory: Instrumentation

All of the far infrared spectra reported in this thesis were observed by means of Fourier transform spectroscopy using far infrared Michelson interferometers. Several excellent reports and books (see for example references 6, 7, 8, and 9) have been written on the theory of Fourier transform spectroscopy. Consequently, the theoretical details and the commonly used data reduction techniques for extracting useful spectra will not be repeated here. The basic far infrared instruments at the M.I.T. Spectroscopy Laboratory and the Francis Bitter National Magnet Laboratory and the associated sample holders and cryostats are described in the first two sections of this chapter. The remainder of the chapter is devoted to the theoretical analysis and synthesis techniques used to extract physical parameters from the observed spectra.

A modified R.I.I.C. (Research and Industrial Instruments Company) FS-520 Fourier Spectrophotometer is the principle far infrared instrument used in the M.I.T. Spectroscopy Laboratory to take the spectra reported in later chapters. A plan view of the basic instrument is shown in Figure 2-1. For measurements up to 400 cm^{-1} the source chamber contains a mercury-arc lamp with a dimpled quartz envelope. From 250 cm^{-1}

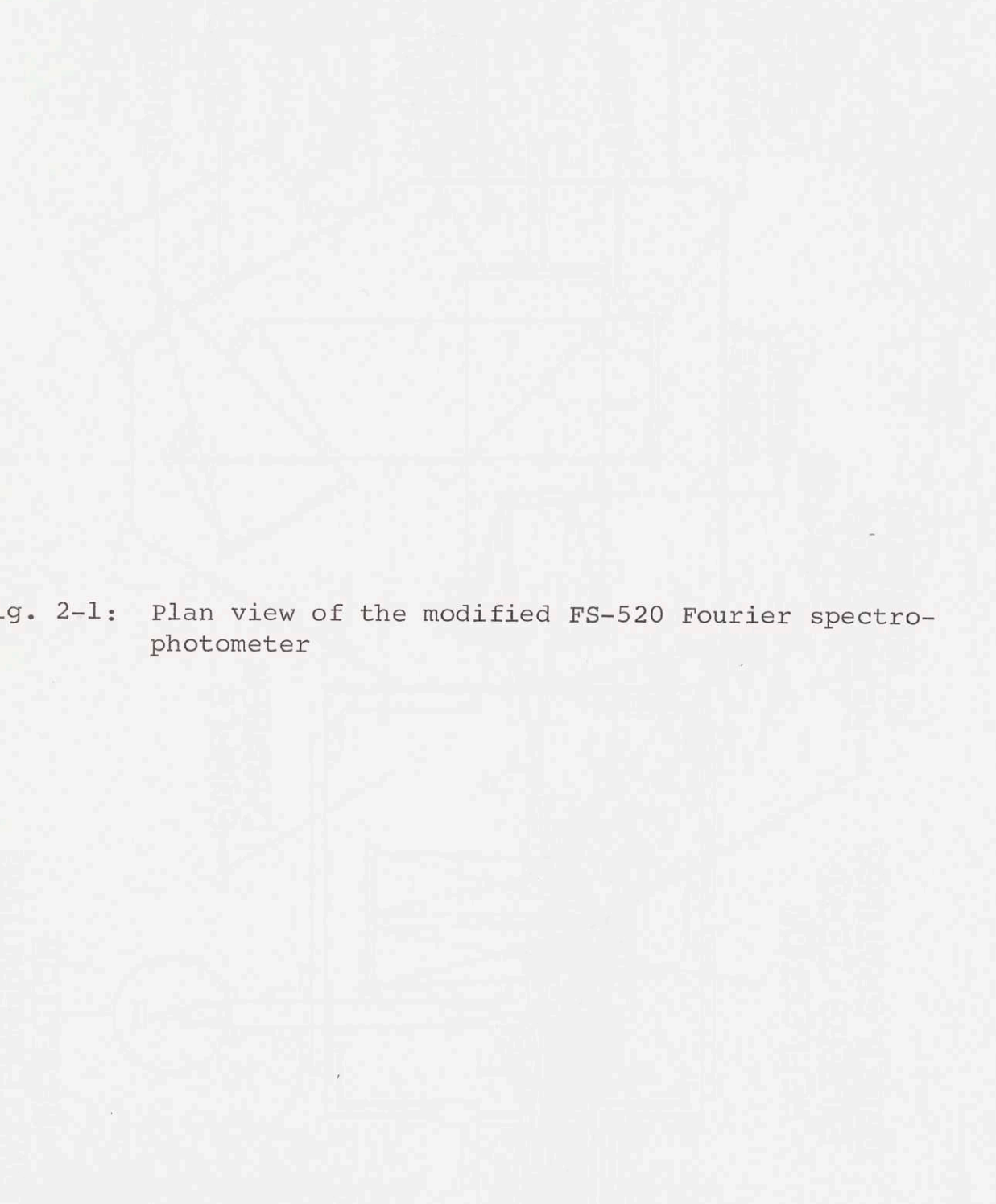
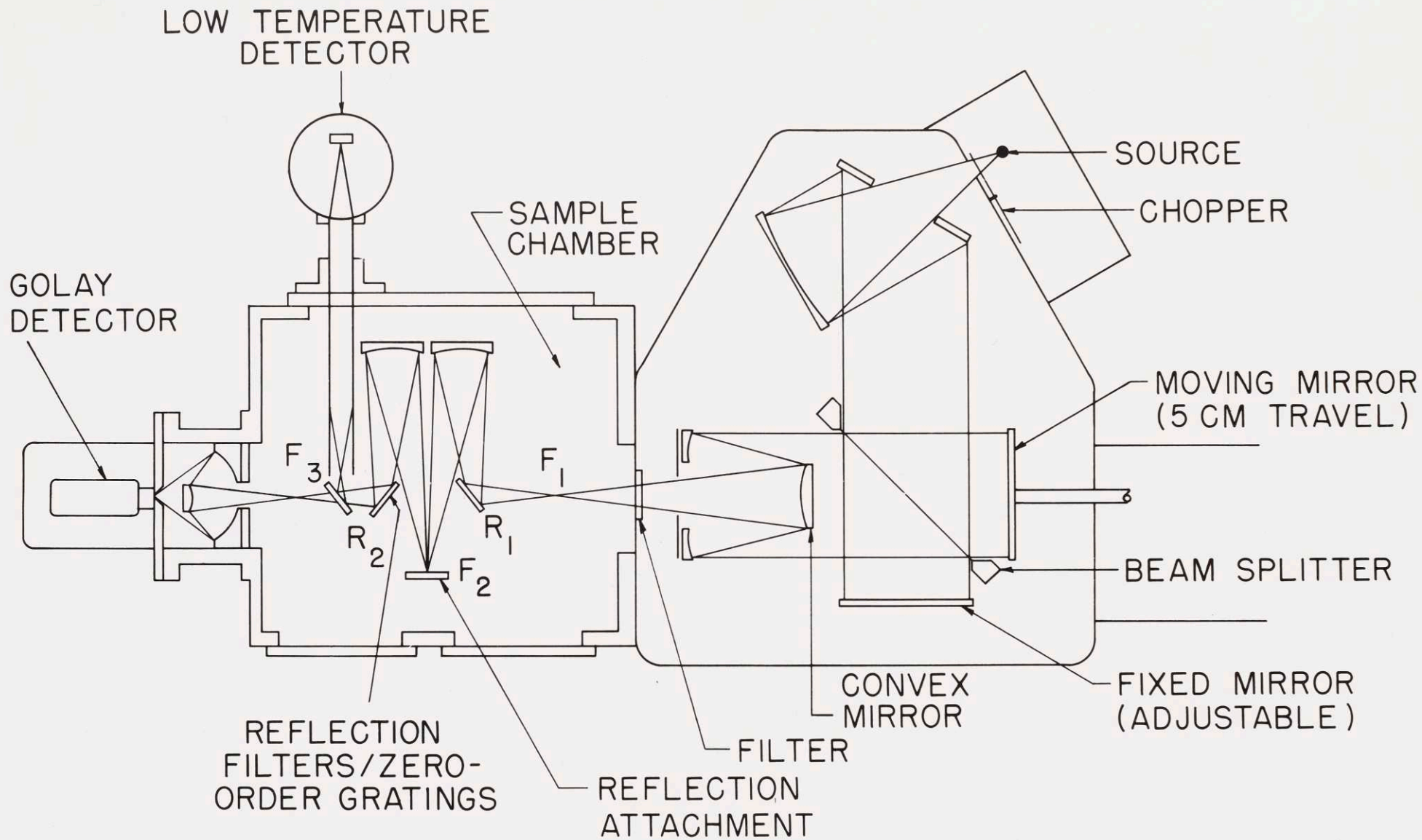


Fig. 2-1: Plan view of the modified FS-520 Fourier spectrophotometer

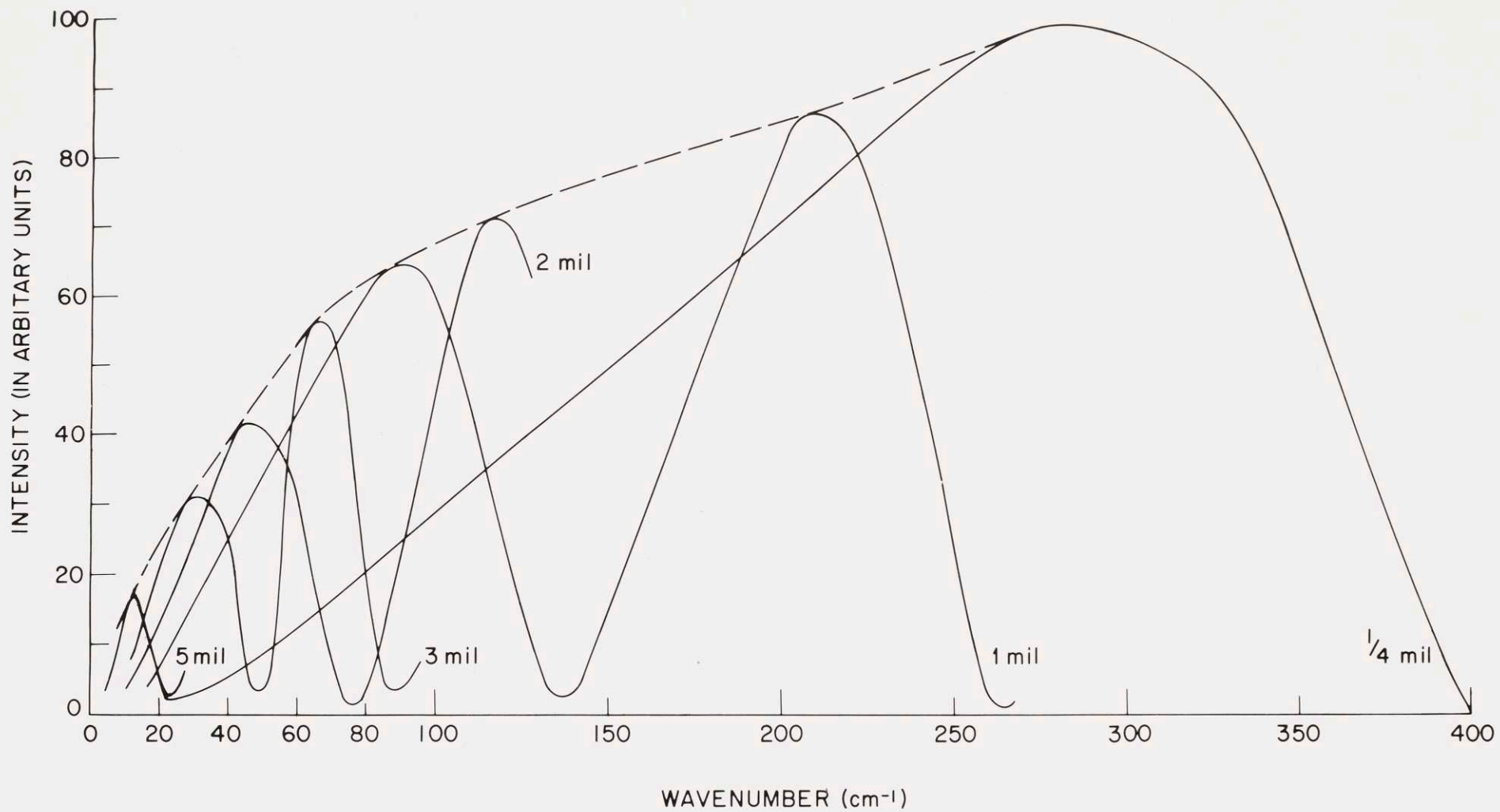


to beyond 750 cm^{-1} a wide Globar source gives more satisfactory results. The beam splitter is a sheet of mylar clamped between machined metal rings. The detector is either a liquid helium cooled gallium doped germanium bolometer (Texas Instruments) or a Golay cell.

Figure 2-2 shows the relative beam splitter efficiencies as a function of frequency for the thicknesses of mylar commonly available. Measurements are generally taken only within the first loop of the beam splitter response--Yoshinaga filters⁽⁶⁾ are used to remove the unwanted radiation at higher frequencies. Measurements taken with four different beam splitters and their associated filters⁽⁶⁾ are reported in this thesis. A 1.0 mil (25.4 micron) beam splitter is used from 20 to 100 cm^{-1} , 0.5 mil (12.7 μm) from 50 to 250 cm^{-1} , 0.25 mil (6.35 μm) from 150 to 400 cm^{-1} , and 0.15 mil (3.81 μm) from 150 to 750 cm^{-1} . The path difference sampling interval is eight microns ($f_{\text{max}} = 625 \text{ cm}^{-1}$) up to 400 cm^{-1} and four microns ($f_{\text{max}} = 1250 \text{ cm}^{-1}$) for measurements beyond 400 cm^{-1} .

Transmittance samples are placed either at focus F1 or focus F3 shown in Figure 2-1. Reflectance samples replace the mirror at focus F2. The instrument is reported to be approximately 70% polarized in the vertical direction.⁽⁶⁾ Nevertheless, in order to obtain more accurate polarized reflectance and transmittance spectra, one of two different one-dimensional wire

Fig. 2-2: Relative efficiencies of mylar beam splitters as a function of frequency and thickness

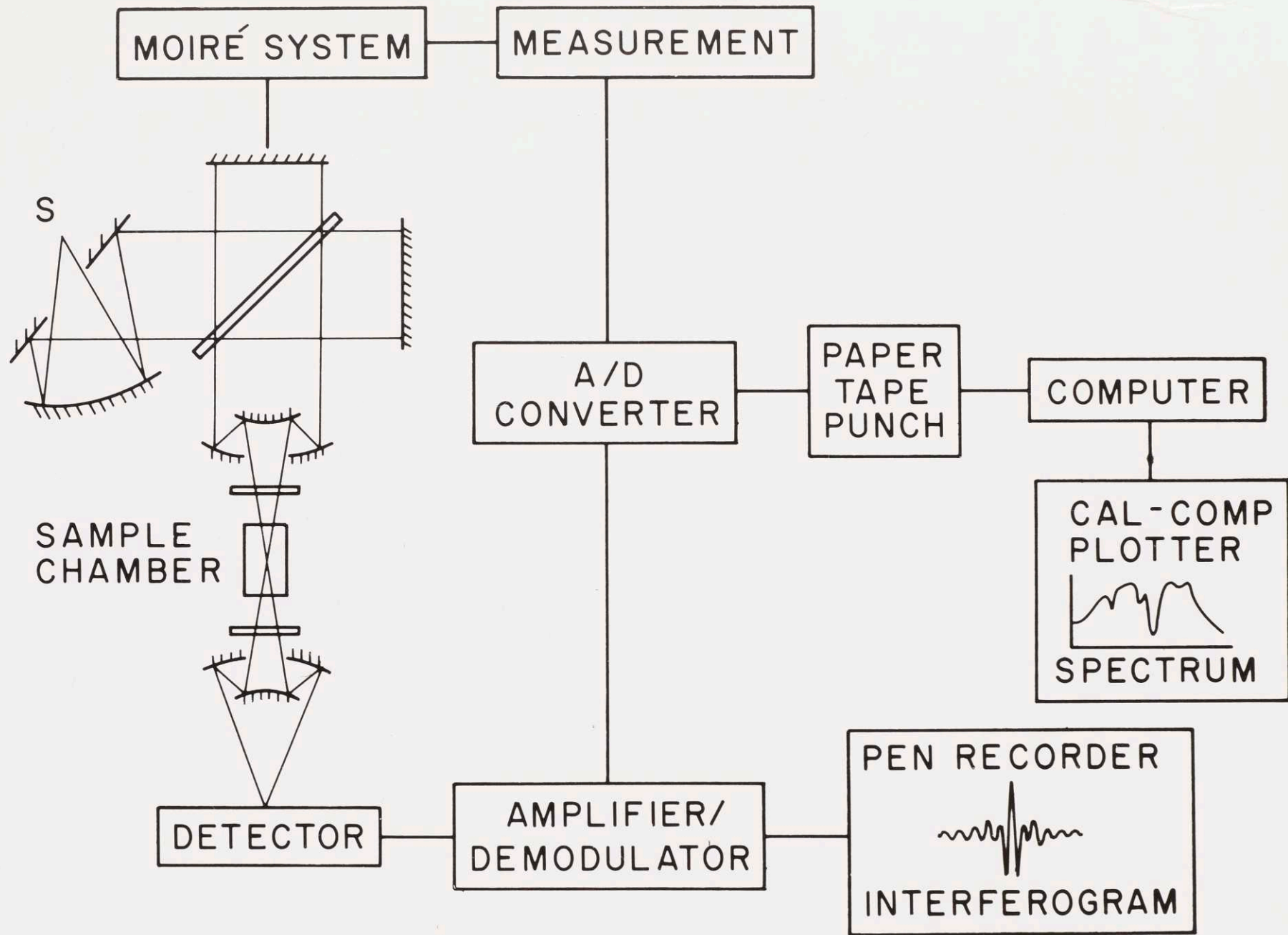


grid polarizers is placed at either F1 or F3. A wire grid polarizer with a grating spacing of $0.5 \mu\text{m}$ on a Kel-F substrate, kindly loaned to the Spectroscopy Laboratory by G. Bird of the Polaroid Corporation, is used between 10 cm^{-1} and 400 cm^{-1} . Beyond 400 cm^{-1} absorption bands of the Kel-F substrate obscure the spectra and a Perkin Elmer polarizer on a silver chloride substrate is used from 250 cm^{-1} to beyond 1000 cm^{-1} . Both polarizers must be used to study the reflectance of the tysonite lanthanide fluorides.

A piece of black polyethelene is placed between the sample chamber and the interferometer chamber in order to filter out both visible and ultraviolet radiation from the Hg-arc quartz lamp. The Yoshinaga filters are generally placed at the output of the sample chamber and immediately in front of the detector. The chemical composition of the filters used in the Spectroscopy Laboratory are described in a review article by C. H. Perry, R. Geick, and E. F. Young.⁽⁶⁾ A Golay detector with a diamond window can be used at any frequency accessible to the FS-520. However, a significant improvement (10-20 db) in the signal to detector noise level can be realized below 250 cm^{-1} by using a helium cooled Ga doped Ge bolometer manufactured by Texas Instruments (TI). A cold quartz window and black polyethelene in the TI detector absorb all of the radiation above 250 cm^{-1} so that additional filtering is usually not necessary for the 0.5 mil beamsplitter. The Golay detector

is used for spectra extending from 150-750 cm^{-1} . The filtering for this high frequency region often consists of only black and white polyethelene or a Perkin Elmer interference filter with a high frequency cut off near 750 cm^{-1} .

A block diagram of the interferometer signal processing system is shown in Figure 2-3. The radiation from the far infrared source is modulated by a metal chopper with either three or five blades. For all of the spectra reported herein, the chopper motor is powered by a fixed frequency, 60 Hz line. The 15 Hz or 25 Hz output of the detector drives the input of a remote preamplifier from a PAR (Princeton Applied Research) HR-8 lock-in amplifier. The amplified and demodulated DC output of the HR-8 drives a chart recorder for monitoring the interferogram and an R.I.I.C. 12 bit analogue to digital converter. A Moire fringe system is used to monitor the position of the movable mirror which moves at a constant speed. Every 8 μm of path difference (or 4 μm for double photocell sampling) the Moire fringe detector sends a pulse to the A-D converter. The A-D converter then samples the value of the interferogram at that instant and quantizes it into a three digit hexadecimal integer which is punched by an ADDO punch into three columns of an 8-level paper tape (7-level paper tape is now standard for the Solid State Spectroscopy Laboratory at Northeastern University, Boston, Massachusetts).



Selected portions of the resulting punched paper tape are fed through an IBM-047 punched paper tape to punched card converter, which punches the hexadecimal integers into standard 80 column IBM cards in the standard IBM-360 FORTRAN-IV FORMAT (20Z4), or the hexadecimal integers are read from the paper tape by a small computer, translated into decimal integers, and recorded onto IBM compatible magnetic tape in the standard FORTRAN FORMAT(16I5). The punched cards or magnetic tape are then processed on an IBM-7094, IBM-360, or a CDC-3500 computer, which takes the Fourier transform of the interferogram and calculates the percent reflectance or transmittance by dividing the sample spectrum by the current background spectrum. Currently, the spectra are plotted on the line printer rather than on the Cal-Comp plotter. A copy of the CDC-3500 FORTRAN-IV program written by the author which accepts hexadecimal or decimal integer data on either punched cards or magnetic tape can be obtained from Professor C. H. Perry, Northeastern University, Boston, Massachusetts.

2.2 Francis Bitter National Magnet Laboratory: Instrumentation

All of the equipment and supplies used at the Francis Bitter National Magnet Laboratory were kindly loaned to the author by Richard W. Stimets, Benjamin Lax, and Kenneth J. Button. The basic far infrared Michelson interferometer is built by Grubb-Parsons. Rather than scanning the movable mirror at a constant

speed as done in the FS-520, it is stepped forward at integer multiples of five microns and the value of the interferogram is measured and quantized while both mirrors are stationary. The Hg-arc quartz lamp source is powered by a DC supply and chopped by a metal blade chopper. The modulated output of the interferometer is focused into a gold-plated brass and stainless steel light pipe which channels the far infrared radiation horizontally over to and then vertically down through the center of an electromagnet. The detector is a pumped liquid helium cooled doped-germanium bolometer placed at the end of the light pipe below the electromagnet. The output of the detector is preamplified by a Tektronix 122 preamplifier, and amplified and demodulated by a PAR lock-in amplifier. The DC output of the lock-in amplifier is sent to either a chart recorder used to monitor the interferogram during alignment or to a Hewlett-Packard integrating digital voltmeter connected to a Tally paper tape punch.

After the step-drive system has located the movable mirror the selected integral multiple of five microns from the previous position, the system waits one second for mechanical and electrical transients to decay and then sends a pulse to the integrating digital voltmeter which integrates the noisy DC signal for the desired length of time. The value of the interferogram at that point is quantized into a four digit decimal integer which is punched into four columns of an eight level paper tape with a space code between each four digit integer. The resulting punched

paper tape is then processed just like those generated by the FS-520 with due regard for the changes in data format.

The reflectance and transmittance samples are placed in the vertical portion of the light pipe near the center of the magnet. The detector is located several inches below the sample and outside the core of the magnet. The entire lower portion of the light pipe, including the sample and the detector, is immersed in liquid helium contained within a double glass dewar system in which the outer dewar is filled with liquid nitrogen. The liquid helium is pumped well below its lambda point, consequently all of the joints in the light pipe are sealed with gold O-rings in order to prevent the light pipe from filling with superfluid helium. Typical operating temperatures for the liquid helium bath, and presumably also for the detector and sample which are separated from the helium bath by only a thin brass wall, are between 1.0°K and 1.7°K .

Due to the lattice bands of tysonite, the transmittance samples absorb radiation between 100 cm^{-1} and 600 cm^{-1} . Consequently the 1.0 mil ($25.4\text{ }\mu\text{m}$) beam splitter with a black polyethylene filter is used for all transmittance measurements. The sampling interval is 40 microns ($f_{\text{max}} = 125\text{ cm}^{-1}$) in transmission. However, for reflectance spectra up to approximately 200 cm^{-1} , the 0.5 mil ($12.7\text{ }\mu\text{m}$) beam splitter, black polyethylene, 1.0 mm of fused quartz, and a 20 micron ($f_{\text{max}} = 250\text{ cm}^{-1}$) sampling interval is used.

Two different electromagnets, 2P and 2S, were used at the Francis Bitter National Magnet Laboratory. Each of them generates approximately 6.8 Gauss per Ampere. For magnetic fields up to 70 Kilogauss only one of the four generators is used. However, for the high intensity fields used to study the PrF_3 samples, one half of the generator facilities (almost five Megawatts) of the laboratory are in use.

2.3 The Dielectric Response Function

Many of the interactions of electromagnetic radiation with matter can be expressed most concisely in terms of a linear dielectric response function. Consequently, when studying the properties of a solid by means of its interaction with electromagnetic radiation, it is instructive to delimit the applicability of the dielectric response function, $\epsilon(\omega)$, by deriving it from Maxwell's equations and auxiliary conditions. Such a procedure will show that it can be applied to the processes of reflection, transmission, absorption, and elastic scattering of electromagnetic radiation, but it can not be applied directly to those processes in which the frequency of the scattered radiation differs from that of the incident radiation, as in Raman scattering. Moreover, by considering $\epsilon(\omega)$ to be an analytic function, the following derivation makes explicit the characteristic parameters of the dielectric response function, which can be completely

specified by a scaling coefficient and the locations of all of the poles and zeros of the function in the complex frequency domain. It is also shown that upper and lower bounds can often be placed on the estimates of the characteristic frequencies of $\epsilon(\omega)$ based upon the experimentally determined values of $\epsilon(\omega)$.

From Maxwell's equations:

$$\vec{D}(\vec{r}, t) = \vec{E}(\vec{r}, t) + 4\pi\vec{P}(\vec{r}, t)$$

If one is working with "small" electric fields, \vec{P} and \vec{D} may be approximated by linear functions of \vec{E} . Using the most general form for the linear operator $L_{sq}(\vec{r}, t; \vec{r}', t')$:

$$D_s(\vec{r}, t) = \sum_{q=1}^3 \int_{-\infty}^{+\infty} dt' \int_{\text{all space}} d^3 r' L_{sq}(\vec{r}, t; \vec{r}', t') E_q(\vec{r}', t')$$

$$\text{where } \vec{D}(\vec{r}, t) = \sum_{s=1}^3 \hat{s} D_s(\vec{r}, t) \quad \hat{s} \equiv \hat{x}, \hat{y}, \hat{z}$$

and $L_{sq}(\vec{r}, t; \vec{r}', t')$ is an element of the general linear operator relating $\vec{D}(\vec{r}, t)$ to $\vec{E}(\vec{r}', t')$. Moreover, since one must work with physically realizable quantities, that is, since all of the physical quantities are bounded in both space and time, the spatial and temporal Fourier transforms of \vec{D} , \vec{E} , and \vec{P} must all exist.

Therefore, one may define:

$$D_s(\vec{r}, t) = (2\pi)^{-2} \int_{-\infty}^{+\infty} d\omega \int_{\text{all } \vec{k}} d^3 k \mathcal{D}_s(\vec{k}, \omega) \exp(i\vec{k} \cdot \vec{r} - i\omega t)$$

similarly

$$E_S(\vec{r}, t) = (2\pi)^{-2} \int_{-\infty}^{+\infty} d\omega \int_{\text{all } \vec{k}} d^3k \mathcal{E}_S(\vec{k}, \omega) \exp(i\vec{k} \cdot \vec{r} - i\omega t)$$

where it is necessary that

$$D_S(\vec{k}, \omega) = D_S^*(-\vec{k}, -\omega) \quad \text{and} \quad \mathcal{E}_S(\vec{k}, \omega) = \mathcal{E}_S^*(-\vec{k}, -\omega)$$

in order that $D_S(\vec{r}, t)$ and $E_S(\vec{r}, t)$ be REAL functions.

If one further assumes that the material being considered is uniform (not isotropic) and does not have any spatial or temporal boundaries, a rather lengthy and not very instructive proof by the author⁽¹⁰⁾ will show that:

$$D_S(\vec{k}, \omega) = \sum_{q=1}^3 L_{sq}(\vec{k}, \omega) \mathcal{E}_q(\vec{k}, \omega)$$

where

$$L_{sq}(\vec{k}, \omega) = \int_{-\infty}^{+\infty} dt \int d^3r L_{sq}(\vec{r}, t; 0, 0) \exp(-i\vec{k} \cdot \vec{r} + i\omega t)$$

$$\text{and } L_{sq}(\vec{k}, \omega) = L_{sq}^*(-\vec{k}, -\omega)$$

in order that $\vec{D}(\vec{r}, t)$ and $\vec{E}(\vec{r}, t)$ be REAL functions.

Note that \vec{k} and ω are merely parameters in the equation relating the Fourier transforms of the electric field and the electric displacement. There is no way to change the direction, the wavelength, or the frequency of an electromagnetic disturbance within the linear dielectric material. The introduction of a spatial boundary allows one to change the direction and wavelength of an electromagnetic disturbance. If the change is discontinuous

in a plane, Fresnel's equations describe the interaction between the different values of \vec{k} most conveniently. However, there is no way to mix different frequency components unless \mathcal{L}_{sq} changes as a function of time (as in the Doppler shift generated by a moving spatial boundary) or unless terms which are nonlinear in \vec{E} and \vec{D} are included in the expansion. Thus $\mathcal{L}_{sq}(k, \omega)$ and the resulting $\epsilon(\omega)$ defined below, together with appropriate spatial boundary conditions, will describe ordinary reflectance, transmittance, and elastic scattering processes but will not apply to nonlinear interactions such as harmonic generation or Raman scattering.

The rest of this derivation will be restricted to propagating electromagnetic disturbances in nonmagnetic materials for which Maxwell's equations put very severe limitations on the frequencies, ω , associated with a given wavevector, \vec{k} . For isotropic (or cubic) materials: $k^2 = \omega^2 c^2 \mathcal{L}(\vec{k}, \omega)$ and \vec{k} is an implicit function of ω . In this case; the isotropic dielectric response function $\epsilon(\omega)$ is defined as the value of $\mathcal{L}(\vec{k}, \omega)$ such that $\mathcal{L}(\vec{k}, \omega) = k^2 / \omega^2 c^2$. A similar but much more complicated expression can be defined for the general dielectric response function tensor, $\mathcal{E}_{sq}(\omega)$, but the discussion may be limited to the isotropic dielectric response function, $\epsilon(\omega)$, without loss in generality.

For an isotropic material, the Fourier transforms of \vec{E} and \vec{D} may be replaced by functions of frequency only, the wavevector

dependence is implicitly contained within $\epsilon(\omega)$. Since $\mathcal{E}_s(\omega)$ and $\mathcal{D}_s(\omega)$ are physical quantities which can have no essential singularities in the complex ω -plane, $\epsilon(\omega)$ can have no essential singularities. All of the poles and zeros of $\epsilon(\omega)$ must be isolated, and in order that $\epsilon(\omega) = \epsilon^*(-\omega)$, they must be symmetrically distributed about the imaginary axis of the ω -plane. Consequently, a pole or a zero of $\epsilon(\omega)$ must either lie on the imaginary ω -axis or be paired with a complementary pole or zero of $\epsilon(\omega)$. In other words, if there is a pole or a zero of $\epsilon(\omega)$ at $\omega_1 = \omega_r + i\omega_i$, there must be a complementary pole or zero at $\omega_2 = -\omega_r + i\omega_i$. Moreover, the poles and zeros of $\mathcal{E}_s(\omega)$ must occur at frequencies such that the magnitude of the time dependent term $\mathcal{E}_s(\omega)\exp(-i\omega t)$ is either constant or exponentially damped. Therefore, the imaginary component of the frequencies of any poles or zeros of \mathcal{E}_s must be less than or equal to zero. The same conclusion holds for the imaginary component of the frequencies of any poles or zeros of \mathcal{D}_s . Consequently, because of the multiplicative relationship, all of the poles and zeros of $\epsilon(\omega)$ must also be in the lower half of the complex ω -plane and $\epsilon(\omega)$ is analytic in the entire upper half plane.

Since the relation between \mathcal{E}_s and \mathcal{D}_s is reciprocal, one may write:

$$\mathcal{D}_s(\omega) = \epsilon(\omega) \mathcal{E}_s(\omega)$$

or:

$$\mathcal{E}_S(\omega) = \epsilon^{-1}(\omega) \mathcal{D}_S(\omega) = \eta(\omega) \mathcal{D}_S(\omega).$$

For materials which are not electrically isotropic, $\eta_{sq}(\omega)$ is the tensor inverse of $\epsilon_{sq}(\omega)$. The poles and zeros of $\epsilon(\omega)$ lead to solutions of Maxwell's equations which may be described as transverse ($\vec{D} \times \vec{k} \neq 0$) or longitudinal ($\vec{D} \times \vec{k} = 0$). A pole of $\epsilon(\omega)$ and a zero of $\eta(\omega)$ occurs whenever there exists a frequency, ω_t , called a transverse optic (TO) frequency, such that $\mathcal{E}_S(\omega_t) = 0$ although $\mathcal{D}_S(\omega_t) \neq 0$. Likewise, a pole of $\eta(\omega)$ and a zero of $\epsilon(\omega)$ occurs whenever there exists a frequency, ω_l , called a longitudinal optic (LO) frequency, such that $\mathcal{D}_S(\omega_l) = 0$ although $\mathcal{E}_S(\omega_l) \neq 0$.

Once the poles and zeros of the dielectric response function have been located, it may be expressed in terms of a product of complementary poles and zeros. For single mode behavior:

$$\epsilon(\omega) = \epsilon_\infty (\omega - \omega_l) (\omega - (-\omega_l^*)) / (\omega - \omega_t) (\omega - (-\omega_t^*))$$

Letting $\omega_L^2 = |\omega_l|^2$, $\Gamma_L = -2\text{Im}[\omega_l]$, $\omega_T^2 = |\omega_t|^2$, and

$$\Gamma_T = -2\text{Im}[\omega_t] : \epsilon(\omega) = \epsilon_\infty (\omega_L^2 - \omega^2 - i\omega \Gamma_L) / (\omega_T^2 - \omega^2 - i\omega \Gamma_T)$$

where $\epsilon_\infty = \epsilon(\omega \rightarrow \infty)$ and all of the coefficients are both REAL and POSITIVE. This latter formula can also be written as:

$$\epsilon(\omega) = \epsilon_\infty ((\omega_L^2 - \omega_T^2) - i\omega(\Gamma_L - \Gamma_T)) / (\omega_T^2 - \omega^2 - i\omega \Gamma_T) + \epsilon_\infty$$

which is analogous to the expression commonly derived for a

damped classical oscillator, except that the numerator of this expression (the classical oscillator strength) can be complex if $\Gamma_L \neq \Gamma_T$.

Using the above expressions for $\epsilon(\omega)$, one can conveniently determine limits on the imaginary components of the frequencies of the poles and zeros. In order that the magnitude of a plane wave propagating through a dielectric medium either remain constant or be exponentially damped with respect to time, $\text{Im}[\epsilon(\omega)] \geq 0$ and $\text{Im}[\eta(\omega)] \leq 0$ for $\omega \geq 0$. Therefore, for single mode behavior: $\text{Im}[\epsilon(\omega)] \geq 0$ as $\omega \rightarrow \infty$ or $\omega \rightarrow 0$.

$$\epsilon(\omega) \xrightarrow{\omega \rightarrow \infty} \epsilon_\infty (\omega + i\Gamma_L) / (\omega + i\Gamma_T) \xrightarrow{\omega \rightarrow \infty} \epsilon_\infty (1 + i(\Gamma_L - \Gamma_T) / \omega).$$

Therefore, since ϵ_∞ is REAL, $\Gamma_L - \Gamma_T \geq 0$ or $\Gamma_L \geq \Gamma_T$.

$$\text{Similarly, } \epsilon(\omega) \xrightarrow{\omega \rightarrow 0} \epsilon_\infty (\omega_L^2 - i\omega\Gamma_L) / (\omega_T^2 - i\omega\Gamma_T)$$

$$\text{or } \epsilon(\omega) \xrightarrow{\omega \rightarrow 0} \epsilon_\infty (\omega_L^2 / \omega_T^2) (1 + i\omega(\Gamma_T / \omega_T^2 - \Gamma_L / \omega_L^2)).$$

$$\text{Therefore, } \Gamma_T / \omega_T^2 - \Gamma_L / \omega_L^2 \geq 0 \text{ or } \Gamma_T / \omega_T^2 \geq \Gamma_L / \omega_L^2.$$

For a general dielectric response function which is expressed as a product of N complementary poles and zeros:

$$\epsilon(\omega) = \epsilon_\infty \prod_{j=1}^N ((\omega_{Lj}^2 - \omega^2 - i\omega\Gamma_{Lj}) / (\omega_{Tj}^2 - \omega^2 - i\omega\Gamma_{Tj})).$$

As the necessary conditions for a physically possible component of the dielectric response function, all of the above relationships generalize to the following: 1) in order that $\epsilon(\omega)$ be

bounded as $\omega \rightarrow 0$ and $\omega \rightarrow \infty$, there must be the same number of zeros as there are poles; 2) the imaginary parts of the frequency of all poles and zeros must be smaller than zero, i.e.

$$\Gamma_{Tj} \geq 0 \quad \text{and} \quad \Gamma_{Lj} \geq 0 ;$$

$$3) \quad \sum_{j=1}^N \Gamma_{Lj} \geq \sum_{j=1}^N \Gamma_{Tj} ; \quad \text{and finally}$$

$$4) \quad \sum_{j=1}^N \Gamma_{Tj} / \omega_{Tj}^2 \geq \sum_{j=1}^N \Gamma_{Lj} / \omega_{Lj}^2 .$$

If one measures a dielectric response function exhibiting single mode behavior, the value of ω_T^2 and Γ_T can be estimated from the behavior of the $\text{Im}[\epsilon(\omega)] = \epsilon''$ and ω_L^2 and Γ_L can be estimated from the behavior of $-\text{Im}[\eta(\omega)] = -\eta''$. There is a peak in the value of $\epsilon''(\omega)$ in the neighborhood of ω_T . Similarly there is a peak in the value of $-\eta''(\omega)$ in the neighborhood of ω_L . The following proof shows that for single mode behavior, ω_T lies between the frequencies of the peaks of $\omega \cdot \epsilon''(\omega)$ and $\epsilon''(\omega)/\omega$. Likewise, ω_L lies between the frequencies of the peaks of $-\omega \cdot \eta''(\omega)$ and $-\eta''(\omega)/\omega$. Γ_T and Γ_L are measured by the half widths of the peaks in the functions defined above.

The peak in $\omega \cdot \epsilon''(\omega)$ occurs when $\frac{\partial (\omega \cdot \epsilon'')}{\partial \omega} = 0$. Evaluating the frequency derivative of this function at the frequency ω_T :

$$\left. \frac{\partial (\omega \cdot \epsilon'')}{\partial \omega} \right|_{\omega=\omega_T} = 2\epsilon_{\infty} \omega_T (\Gamma_L - \Gamma_T) / \Gamma_T^2$$

Therefore:
$$\left. \frac{\partial (\omega \cdot \epsilon'')}{\partial \omega} \right|_{\omega=\omega_T} \geq 0$$

for all allowed values of Γ_T and Γ_L because

$$(\omega_L^2 / \omega_T^2) \Gamma_L \geq \Gamma_L \geq \Gamma_T \geq 0$$

as shown above for single mode behavior. In a like manner, evaluating the frequency derivative of $\epsilon''(\omega)/\omega$ at the frequency ω_T :

$$\left. \frac{\partial (\epsilon''/\omega)}{\partial \omega} \right|_{\omega=\omega_T} = 2\epsilon_\infty \left((\Gamma_L - \Gamma_T) / \Gamma_T^2 - (\omega_L^2 - \omega_T^2) / \Gamma_T \omega_T^2 \right)$$

Therefore:

$$\left. \frac{\partial (\epsilon''/\omega)}{\partial \omega} \right|_{\omega=\omega_T} \leq 0$$

for all allowed values of Γ_T and Γ_L . The peak of $\omega \cdot \epsilon''(\omega)$ occurs at ω_T if $\Gamma_L = \Gamma_T$ and the peak of $\epsilon''(\omega)/\omega$ occurs at ω_T if $\Gamma_L = (\omega_L^2 / \omega_T^2) \Gamma_T$. Otherwise, ω_T lies between the peaks of these two dielectric functions. If ω_1 is defined as the frequency at which the peak in $\epsilon''(\omega)/\omega$ occurs and ω_2 is defined as the frequency at which the peak in $\omega \cdot \epsilon''(\omega)$ occurs, then

$$\omega_1 \leq \omega_T \leq \omega_2$$

for single mode behavior. Moreover, since $\eta(\omega) = \epsilon^{-1}(\omega)$ inverts the behavior of ω_L and ω_T , it can be easily shown that

$$\omega_3 \leq \omega_L \leq \omega_4$$

for single mode behavior, where ω_3 is defined as the frequency at which the peak in $-\eta''(\omega)/\omega$ occurs and ω_4 is the frequency at which the peak in $-\omega \cdot \eta''(\omega)$ occurs. $\omega_L = \omega_3$ if $\Gamma_L = (\omega_L^2/\omega_T^2) \Gamma_T$ and $\omega_L = \omega_4$ if $\Gamma_L = \Gamma_T$.

In addition, the above relation for ω_T and ω_L may be expected to hold approximately for nearly isolated modes in a multimode dielectric response function. In this case ϵ_∞ is replaced by an effective high frequency dielectric constant which incorporates the effects of all modes at a higher frequency than the desired pole-zero pair. $\epsilon_\infty(\text{effective}) =$

$$\epsilon_\infty \prod_{j=m+1}^N (\omega_{Lj}^2 / \omega_{Tj}^2) \text{ for the } m\text{-th mode.}$$

The following section shows that if the dielectric response function is accurately approximated by the classical oscillator model, then the upper bounds upon ω_T and ω_L , namely ω_2 and ω_4 , are the most accurate locators for the TO and LO modes. That is, ω_T and ω_L can be located by peaks in $\omega \cdot \epsilon''(\omega)$ and $\omega \cdot \eta''(\omega)$, Γ_T and Γ_L can be measured by the half widths of the peaks.

2.4 Kramers-Kronig Analysis

Fresnel's equations governing the reflectance of electromagnetic radiation from a plane dielectric surface show that the experimentally measured value of the reflectance is equal to the magnitude of a complex number. In other words,

$$R_{\text{exp}} = (r \cdot \exp(i\varphi)) \cdot (r \cdot \exp(i\varphi))^* . \text{ Taking the principal complex}$$

logarithm of both numbers, $\ln(R_{\text{exp}}) = 2 \ln(r)$ and $\ln(r \cdot \exp(i\varphi)) = \ln(r) + i\varphi = \frac{1}{2}\ln(R_{\text{exp}}) + i\varphi$. Since, based upon the information in preceding section, it can be shown that $r \cdot \exp(i\varphi)$ is nonzero and analytic in the upper half of the complex frequency plane, the real and imaginary parts of $\ln(r \cdot \exp(i\varphi))$ can be related to one another by a Hilbert transform. (11) The special case of the Hilbert transform used to analyze reflectance spectra is called the Kramers-Kronig transform and states that:

$$\varphi(\omega) = (\omega/\pi) \int_0^{\infty} (\ln(R(\Omega)) - \ln(R(\omega)))/(\Omega^2 - \omega^2) d\Omega.$$

The largest contribution to $\varphi(\omega)$ usually occurs in the region where Ω is approximately equal to ω , so that the experimental reflectance, $R(\Omega)$, does not actually have to be measured from zero to infinite frequencies in order to accurately estimate $\varphi(\omega)$. Nevertheless, the experimental reflectance, $R(\Omega)$, must be extrapolated to a constant value at both very high and very low frequencies in order that the wings of the integral make a negligible contribution. One of the more conveniently mechanized evaluations of this integral is attributed to E.A. Guillemin. (12) The logarithm of $R(\Omega)$ is approximated by straight line segments connecting $R(\Omega_i)$ at Ω_i with $R(\Omega_{i+1})$ at Ω_{i+1} . This piecewise linear function is then integrated by parts twice to yield a summation expressed in terms of the amplitude of the

discontinuity in the first derivative, $DTWO(\Omega_i)$, of $\ln(R(\Omega_i))$.

$$\varphi(\omega) = -\frac{1}{\pi} \sum_i DTWO(\Omega_i) ((\omega + \Omega_i) \ln |\omega + \Omega_i| + (\omega - \Omega_i) \ln |\omega - \Omega_i|) .$$

Once the phase angle, $\varphi(\omega)$, has been evaluated, various formulas⁽¹³⁻¹⁶⁾ can be used to calculate the real and imaginary parts of the dielectric response function. For the two reflectance channels of a cubic or isotropic material, the formulas derived by D.W. Berreman⁽¹⁶⁾ are convenient. Letting $r \cdot \exp(i\varphi) = (Z-1)/(Z+1)$ one can solve for Z and substitute into the appropriate formula in terms of the angle of incidence θ :

$$\epsilon(\omega) = Z^2 \cos^2 \theta + \sin^2 \theta ,$$

for the electric field perpendicular to the plane of incidence, and:

$$\epsilon(\omega) = (Z^2 / 2 \cos^2 \theta) (1 \pm (1 - (4 \cos^2 \theta \sin^2 \theta) / Z^2)^{1/2}) ,$$

for the electric field parallel to the plane of incidence.

Unfortunately, there is an ambiguous sign in the second formula and a mechanized solution for $\epsilon(\omega)$ may not always yield the true solution. However, the first formula is unambiguous and also corresponds to the most convenient experimental setup. A copy of the Kramers-Kronig program for calculating the dielectric response function from the reflectance measured with the electric field perpendicular to the plane of incidence can be obtained from Professor C. H. Perry at Northeastern University, Boston, Massachusetts.

The absolute accuracy of the resulting $\epsilon(\omega)$ depends rather strongly upon the absolute accuracy of the experimental measurements. However many of the useful parameters of $\epsilon(\omega)$ can be determined rather accurately from the shape or functional variation of $\epsilon(\omega)$. As shown in the preceding section and displayed in Figure 2-4, the poles of $\epsilon(\omega)$ can be located rather well (usually better than $\pm 2\text{cm}^{-1}$) by peaks in the imaginary part of $\omega \cdot \epsilon(\omega)$ and the zeros of $\epsilon(\omega)$ can be located by peaks in the imaginary part of $-\omega \cdot \eta(\omega) = -\omega \cdot \epsilon^{-1}(\omega)$. The half widths of the poles and zeros, and thereby their distance from the real frequency axis, can be measured by the half width of the corresponding peaks. The resulting poles and zeros (corresponding to TO and LO resonances) can then be used in conjunction with an effective high frequency dielectric constant to synthesize the reflectance spectrum as described in the next section.

2.5 Classical Oscillator Synthesis

Perhaps the most accurate formula for synthesizing the dielectric response function, and thereby the reflectance and transmittance of a material, is the complex pole and zero formulation derived earlier. Usually only a single complementary pair of poles and zeros (two complex frequencies or four parameters) are required for each reststrahlen peak and the summation restrictions on the damping constants are not especially difficult to satisfy. Dwight W. Berreman and F. C. Unterwald⁽¹⁷⁾

have used this formulation to synthesize the reflectance spectra of LaCl_3 and PrCl_3 with excellent results. However, they do find that the addition of an extra pole-zero pair very close together and rather far from the real frequency axis improves the fit between the synthetic and experimental dispersion curves. Presumably, this additional, rather weak, and moderately damped resonance in the dielectric response function represents a weighted average of many higher order absorption mechanisms near the lattice modes of the real crystal. This area of investigation appears ripe for additional discoveries and should be pursued further. However, the remainder of this section will examine the relationships between the more accurate pole-zero formulation and the classical dispersion formulations derived for resonances in the electric susceptibility.

There are several, conventional, theoretical derivations relating the macroscopic dielectric response function to harmonic resonances in the microscopic electric polarizability and thereby resonances in the dielectric response function. Single mode behavior results from a single harmonic resonance in the microscopic electric polarizability. For single mode behavior: (18-20)

$$\epsilon(\omega) = \epsilon_\infty + S^2 / (\omega_T^2 - \omega^2 - i\omega \Gamma_T) ,$$

where all of the parameters are both REAL and POSITIVE. S is the electric dipole strength of the resonance, ω_T is the transverse optic frequency of the resonance, and Γ_T is the

phenomenological transverse damping constant. A simple algebraic transformation shows that the single mode classical oscillator formula can be rewritten in terms of a product of complementary poles and zeros.

$$\epsilon(\omega) = \epsilon_{\infty} \frac{((\omega_T^2 + S^2/\epsilon_{\infty}) - \omega^2 - i\omega\Gamma_T)}{(\omega_T^2 - \omega^2 - i\omega\Gamma_T)}$$

By inspection: $\omega_L^2 = \omega_T^2 + S^2/\epsilon_{\infty}$ and $\Gamma_L = \Gamma_T$. Thus the single mode classical oscillator formula corresponds to the single mode general dielectric response function for which $\Gamma_L = \Gamma_T$ and $\omega_L \geq \omega_T$, the other parameters are unrestricted as long as they are both real and positive.

The classical oscillator model can be generalized to a sum of N independent resonances. (20, 21)

$$\epsilon(\omega) = \epsilon_{\infty} + \sum_{j=1}^N \frac{S_j^2}{(\omega_{Tj}^2 - \omega^2 - i\omega\Gamma_{Tj})}$$

It is trivial to show that when there is more than one resonance, it is not necessarily true that $\omega_{Lj}^2 = \omega_{Tj}^2 + S_j^2/\epsilon_{\infty}$ and $\Gamma_{Lj} = \Gamma_{Tj}$. However, it can be shown that $\omega_{Tj} \leq \omega_{Lj} \leq \omega_{Tj+1}$

and $\sum_{j=1}^N \Gamma_{Lj} = \sum_{j=1}^N \Gamma_{Tj}$ as long as the parameters are real

and positive. Moreover,

$$\lim_{\omega \rightarrow \omega_{Tj}} (\omega - \omega_{Tj}) \cdot \epsilon(\omega) = -S_j^2 / (\omega_{Tj}^2 - \Gamma_{Tj}^2/4)^{\frac{1}{2}}$$

is REAL. Thus, the multimode independent classical oscillator formula corresponds to the restricted multimode general dielectric response function for which

$$\omega_{Tj} \leq \omega_{Lj} \leq \omega_{Tj+1} \quad , \quad \sum_{j=1}^N \Gamma_{Lj} = \sum_{j=1}^N \Gamma_{Tj} \quad ,$$

and the amplitude of the pole at $\omega = \omega_{Tj}$ is REAL.

Unfortunately, A.S. Barker and J.J. Hopfield⁽²²⁾ have shown that the classical oscillator formulas stated above are not adequate to synthesize the reflectance of BaTiO₃, SrTiO₃, and KTaO₃. For these high dielectric constant materials a system of mechanically coupled harmonic oscillators must be used to approximate the electric susceptibility. Two harmonic oscillators coupled by a dashpot yield:^(22,23)

$$\epsilon(\omega) = \epsilon_{\infty} + \frac{S_1^2 (\omega_2^2 - \omega^2 - i\omega(\Gamma_2 + \gamma_{12})) - 2i\omega\gamma_{12} S_1 S_2 + S_2^2 (\omega_1^2 - \omega^2 - i\omega(\Gamma_1 + \gamma_{12}))}{(\omega_1^2 - \omega^2 - i\omega(\Gamma_1 + \gamma_{12})) (\omega_2^2 - \omega^2 - i\omega(\Gamma_2 + \gamma_{12})) + \omega^2 \gamma_{12}^2}$$

If $\gamma_{12} = 0$, this formula reduces to the sum of two independent classical oscillators. With some laborious algebraic manipulations it is possible to show that this formula can be written as a product of two pairs of complementary poles and zeros for which:

$$\omega_{T1}^2 \omega_{T2}^2 = \omega_1^2 \omega_2^2 \quad , \quad \omega_{T1}^2 + \omega_{T2}^2 = \omega_1^2 + \omega_2^2 + \gamma_{12}^2 \quad ,$$

and

$$\Gamma_{T1} + \Gamma_{T2} = \Gamma_1 + \Gamma_2 + 2\gamma_{12} .$$

Likewise:

$$\Gamma_{L1} + \Gamma_{L2} = \Gamma_{T1} + \Gamma_{T2}, \quad \omega_{L1}^2 \omega_{L2}^2 = (\omega_1^2 + S_1^2/\epsilon_\infty)(\omega_2^2 + S_2^2/\epsilon_\infty) - (S_1 S_2/\epsilon_\infty)^2$$

and

$$\omega_{L1}^2 + \omega_{L2}^2 = \omega_{T1}^2 + \omega_{T2}^2 + S_1^2/\epsilon_\infty + S_2^2/\epsilon_\infty .$$

Using a matrix formulation, these results can be extended to more than two coupled modes and the equality between $\sum_{j=1}^N \Gamma_{Lj}$ and $\sum_{j=1}^N \Gamma_{Tj}$ can be proved for an indefinitely large number of coupled modes. Moreover, it can be shown that

limit $(\omega - \omega_{Tj}) \cdot \epsilon(\omega)$ is not necessarily real if $\gamma_{jk} \neq 0$. Although $\omega \rightarrow \omega_{Tj}$ it has not been proved by the author, it is reasonable to

expect that $\omega_{Tj} \leq \omega_{Lj} \leq \omega_{Tj+1}$ for this formulation. Thus, the multimode coupled classical oscillator formula corresponds to the restricted multimode general dielectric response function for which $\sum_{j=1}^N \Gamma_{Lj} = \sum_{j=1}^N \Gamma_{Tj}$ and the amplitude of the pole at $\omega = \omega_{Tj}$ is COMPLEX. The imaginary parts of the complex amplitudes are also subject to a summation restriction by the system of coupled algebraic equations.

All of the classical oscillator approximations of the dielectric response function stated above require that

$$\sum_{j=1}^N \Gamma_{Lj} = \sum_{j=1}^N \Gamma_{Tj}$$

whereas causality conditions require only that

$$\sum_{j=1}^N \Gamma_{Lj} \geq \sum_{j=1}^N \Gamma_{Tj} \quad .$$

Only by allowing loss mechanisms which are implicitly frequency dependent and thereby have different cumulative effects on the TO and LO modes can the full generality of the physically possible dielectric response function be realized. It remains to be seen whether the restricted or unrestricted formulation is more appropriate for real crystals. It may be heuristically justified to use the restricted (equality sign) formulation, at least as a first approximation, until the assumptions implicit in the classical oscillator models are found to be inadequate.

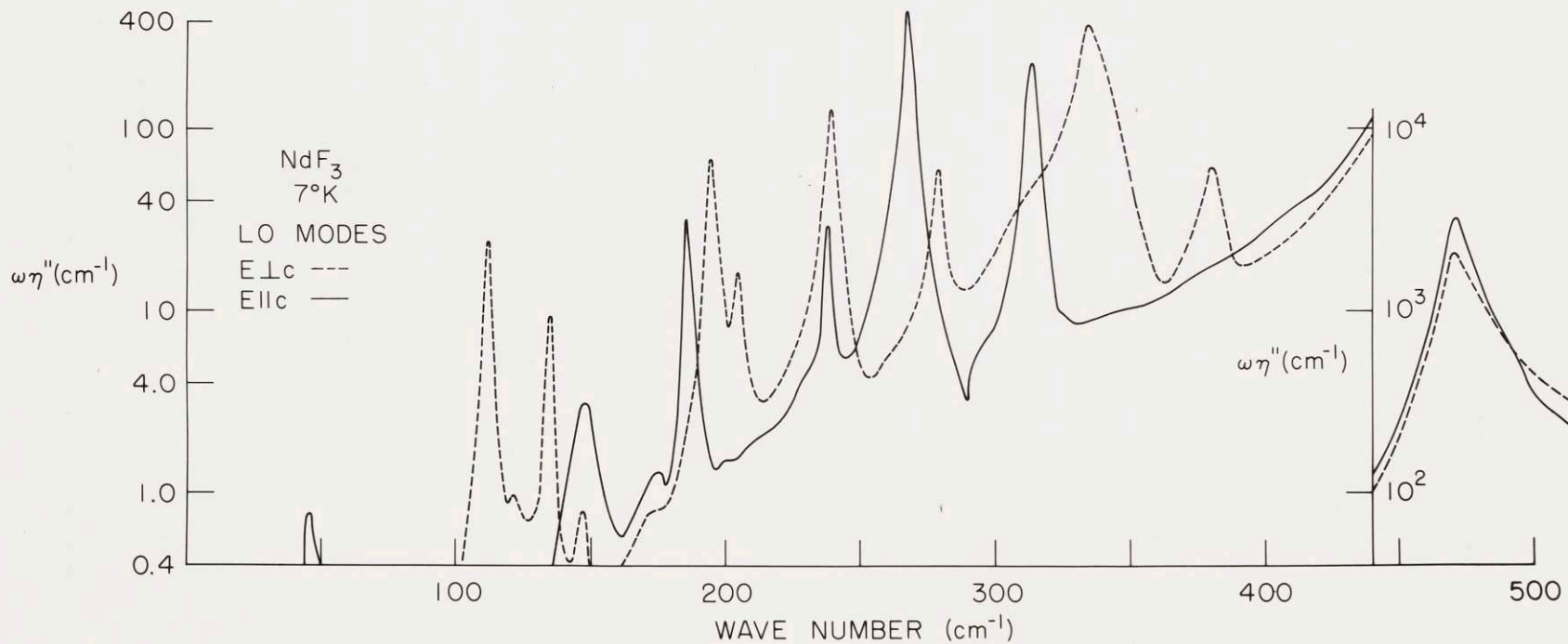
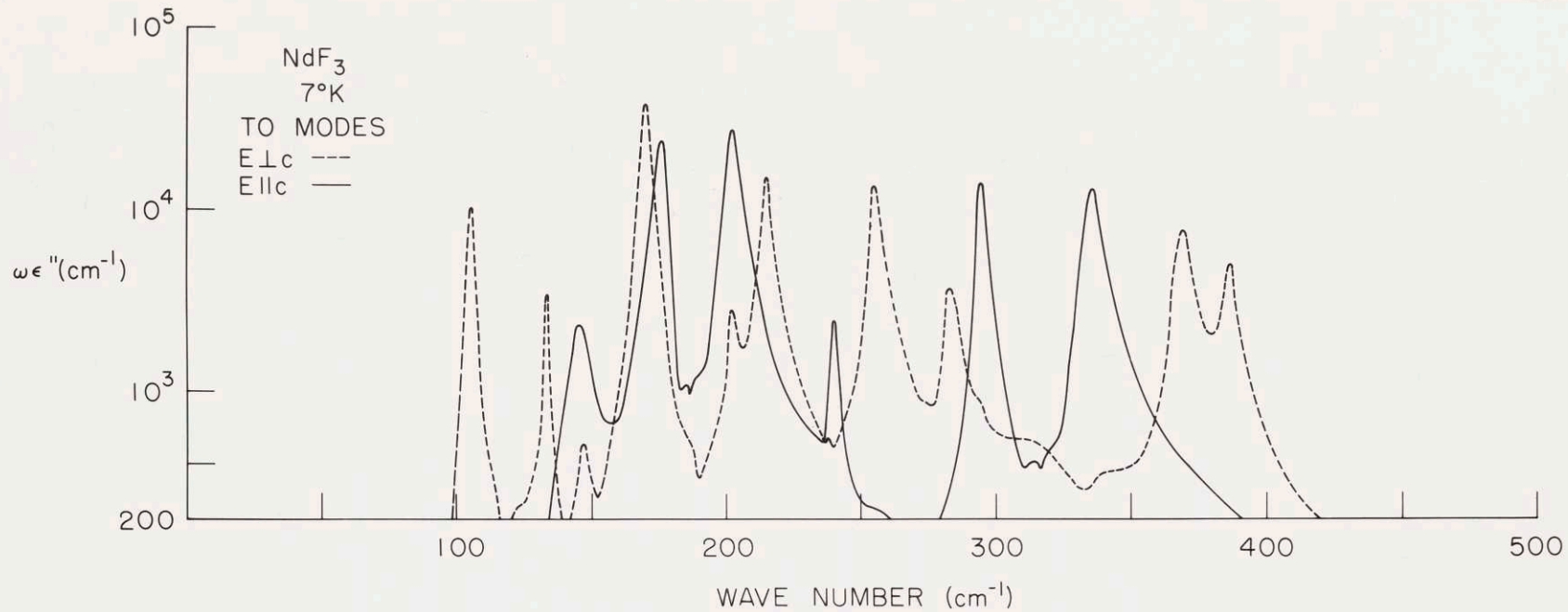
2.6 Measuring Uniaxial Dielectric Response

The effective, experimental dielectric response function for each component of the uniaxial dielectric response tensor of tysonite is calculated from a Kramers-Kronig analysis of the reflectance measurements using the Fresnel formula appropriate for a crystal aligned with the desired axis precisely parallel to the incident electric field and perpendicular to the plane of incidence. The infrared active TO (transverse optical) frequencies are associated with the poles of the dielectric response function ($|D| \neq 0, |E| \rightarrow 0$) and located by peaks in $\omega \cdot \epsilon''$ ($\hat{\epsilon} = \epsilon' + i\epsilon''$) which is proportional to the electric conductivity, $\sigma = \omega \cdot \epsilon''/4\pi$. The infrared active LO (longitudinal optical) frequencies are associated with the zeros of the

dielectric response function ($|D| \rightarrow 0$, $|E| \neq 0$) and are located by peaks in $\omega \cdot \eta''$ ($\hat{\epsilon}^{-1} = \hat{\eta} = \eta' + i\eta''$, $\eta'' = -\epsilon''/|\hat{\epsilon}|$). The half widths (damping constants) of the modes are measured by the half widths of the corresponding peaks in the dielectric response. Typical spectra of $\omega \cdot \epsilon''$ and $\omega \cdot \eta''$ are displayed in Figure 2.4 for the low temperature reflectance of NdF_3 in both the π - ($E \parallel c$) and σ -polarizations ($E \perp c$).

The principle poles and zeros of both components of the dielectric response tensor of tysonite were identified quite satisfactorily using the above procedure. Since the reflectance was measured at low angle of incidence (approximately 7.5°), the location of the TO frequencies and the lower LO frequencies did not change significantly when the Fresnel formula for normal incidence was used to analyze the Kramers-Kronig transform of the reflectance measurements. However, the frequency of the highest LO mode appears to be five to ten wave numbers higher than its true value if the incorrect formula is used. As the angle of incidence is increased, the apparent location of an LO mode can move from its true location ($|\epsilon| = 0 \Rightarrow n = 0$) to as high as the Christiansen frequency⁽²⁴⁻²⁶⁾ in a vacuum ($n=1$). For the lower frequency modes the difference between these frequencies is small, but for the highest frequency mode the difference can be quite large. In addition to this rather obvious effect of using an incorrect Fresnel formula to analyze

Figure 2.4: Infrared active TO and LO frequency locators for NdF_3 reflectance spectra.



the experimental data, there are also measureable effects in both reflectance and transmittance due to a slight misalignment of the crystal axes from the ideal position assumed in the above analysis. In order to understand the nature and the magnitude of the effects of this misalignment, it is instructive to solve a special case of the reflectance and transmittance of a uniaxial single crystal.

In a uniaxial crystal ($\hat{\epsilon}_x = \hat{\epsilon}_y \neq \hat{\epsilon}_z$) electromagnetic radiation splits into an ordinary wave and an extraordinary wave which propagate in the same direction but with different phase velocities. If the direction of propagation of incident radiation is normal to the crystal-vacuum interface, the ordinary and extraordinary waves inside the crystal propagate in the same direction as the incident radiation. Letting φ be the angle between the incident electric field of a linearly polarized beam and the projection of the optic axis (c or z axis) on the crystal face, it can be easily shown that: $R = R_0 \sin^2 \varphi + R_e \cos^2 \varphi$ and $T = T_0 \sin^2 \varphi + T_e \cos^2 \varphi$ where R and T are the effective normal reflectance and transmittance coefficients of the crystal, R_0, T_0, R_e and T_e are the normal reflectance and transmittance coefficients for the ordinary wave and the extraordinary wave respectively.

If $\varphi \approx 0$, then $R = R_e + (R_0 - R_e) \sin^2 \varphi \approx R_e$. Since $|R_0 - R_e| \leq 1$ and in practice $\sin^2 \varphi \leq 0.01$, it is clear that one

can measure the extraordinary reflectance coefficient within an additive error of less than 1% reflectance. Similarly, if $\varphi \approx 90^\circ$, the ordinary reflectance coefficient can be measured within 1% reflectance. Likewise it can be shown that the ordinary and extraordinary transmittance coefficients at normal incidence can be measured within an additive error of 1% transmittance. As a result, the errors introduced in the measurement of the reflectance or transmittance by a slight error (less than five arc degrees) in the orientation of a plane polarizer with respect to the optic axis can either be conveniently ignored or be eliminated by small corrections based upon measurements in the orthogonal plane of polarization.

Moreover, since at normal incidence $R_0 = |(1-\hat{n}_x)/(1+\hat{n}_x)|^2$ and ignoring interference effects $T_0 \approx (1-R_0)^2 \exp(-\alpha_x d)$, where $\hat{n}_x = (\mu \hat{\epsilon}_x)^{1/2}$, d is the thickness of the crystal, and $\alpha_x = 2\pi\omega \text{Im}[\hat{n}_x]$, one of the components of the dielectric response tensor, namely $\hat{\epsilon}_x$, can be calculated directly from R_0 and T_0 .

Unfortunately, $\hat{\epsilon}_z$ can not be calculated directly from R_e and T_e . Indeed, $R_e = |(1-\hat{n}_e)/(1+\hat{n}_e)|^2$ and ignoring interference effects

$$T_e = (1 - R_e)^2 \exp(-\alpha_e) ,$$

where

$$\hat{n}_e = c/v_e = (\mu \hat{\epsilon}_e)^{1/2}$$

and

$$\alpha_e = 2\pi\omega \text{Im}[\hat{n}_e] ,$$

but (27)
$$v_e^2 = v_z^2 \cos^2 \theta + v_x^2 \sin^2 \theta$$

where
$$v_x^2 = c^2 / \mu \hat{\epsilon}_x, \quad v_z^2 = c^2 / \mu \hat{\epsilon}_z,$$

and θ is the angle between the optic axis and the plane of the crystal face. Rewriting the formula for the phase velocity, v_e , in terms of an effective dielectric response function, $\hat{\epsilon}_e$:

$$\hat{\epsilon}_e = (\hat{\epsilon}_z^{-1} \cos^2 \theta + \hat{\epsilon}_x^{-1} \sin^2 \theta)^{-1}.$$

By inspection it can be seen that as long as $\theta \neq 0$ or 90° then $\hat{\epsilon}_e$ must have zeros at all of the zeros of both $\hat{\epsilon}_x$ and $\hat{\epsilon}_z$ independent of the precise value of θ . However, the strengths of the zeros, as measured by $\eta'' = \epsilon'' / |\hat{\epsilon}|$, and the resulting locations of the poles of $\hat{\epsilon}_e$ both depend very strongly on the value of θ . A simpler form of this relation can be expressed in terms of the reciprocal of the dielectric response functions. Letting $\hat{\eta} = \hat{\epsilon}^{-1}$,

$$\hat{\eta}_e = \hat{\eta}_z \cos^2 \theta + \hat{\eta}_x \sin^2 \theta.$$

Again by inspection it is clear that there must be poles of $\hat{\eta}_e$ at all of the poles of both $\hat{\eta}_x$ and $\hat{\eta}_z$. Moreover, the strengths of the poles of $\hat{\eta}_e$ (zeros of $\hat{\epsilon}_e$) in terms of the strengths of the poles of $\hat{\eta}_x$ and $\hat{\eta}_z$ depend upon θ in a very simple way.

The crystals used in this study were cut and polished with the optic axis parallel to the face of the crystal within an estimated five arc degrees, so that $\sin^2 \theta \approx \theta^2 \leq 0.01$. Therefore,

$$\hat{n}_e = \hat{n}_z (1 + (\hat{\epsilon}_z / \hat{\epsilon}_x - 1) \sin^2 \theta)^{-1/2} \approx n_z - \theta^2 \hat{n}_z (\hat{\epsilon}_z - \hat{\epsilon}_x) / 2\hat{\epsilon}_x$$

as long as $|\theta^2 / \hat{\epsilon}_x| \ll 1$. Under these conditions,

$$R_e \approx R_z \pm 2\theta^2 \cdot R_z \cdot |\hat{n}_z / (1 - \hat{\epsilon}_z)| \cdot |(\hat{\epsilon}_z - \hat{\epsilon}_x) / \hat{\epsilon}_x|$$

and

$$T_e \approx (1 - R_e)^2 \exp(-\alpha_e d)$$

where

$$R_z = \left| \frac{1 - \hat{n}_z}{1 + \hat{n}_z} \right|^2,$$

$$\alpha_e = \alpha_z - \pi\omega \operatorname{Im} \left[\left(\theta^2 / \hat{\epsilon}_x \right) \hat{n}_z (\hat{\epsilon}_z - \hat{\epsilon}_x) \right],$$

and

$$\alpha_z = 2\pi\omega \operatorname{Im}[\hat{n}_z].$$

Clearly, even when $\theta^2 \leq 0.01$, there is no assurance that the difference between R_e and R_z or between T_e and T_z must be less than 1% as is the case for a slight misalignment of the polarizer with respect to the optic axis. In fact, whenever one approaches an LO frequency of $\hat{\epsilon}_x$, that is whenever one is near a zero of $\hat{\epsilon}_x$ or a pole of $\hat{\eta}_x$, significant features may be expected in R_e and T_e . In a low dispersion region of $\hat{\epsilon}_z$ in which $\operatorname{Re}(\hat{n}_z) = \text{const.} = n_z$ and $\operatorname{Im}(\hat{n}_z) = 0$, then

$$R_e \approx R_z + K_1 (\theta^2 / |\hat{\epsilon}_x|)$$

and
$$\alpha_e \approx -K_2 \theta^2 \omega \eta_x''$$

where $\eta_x'' = \operatorname{Im}[\eta_z]$ and $K_2 = \pi n_z^3 / \mu$ and where K_1 may be

evaluated from R_e and R_0 . Consequently, even in regions where $\hat{\epsilon}_z$ is approximately constant, there will be a weak peak or dip in the reflectance and a moderately strong minimum in the transmittance proportional to θ^2 whenever the observational frequency approaches an LO frequency of $\hat{\epsilon}_x$. By orienting the crystal so that $\theta \approx 90^\circ$, minima in the extraordinary transmittance due to the LO frequencies of $\hat{\epsilon}_z$ can be observed for radiation propagating almost parallel to the optic axis.

This weak coupling of the nominally transverse material electromagnetic wave (mixed photon-phonon particle wave) to the longitudinal optical (LO) frequencies of the orthogonal components of the dielectric response tensor apparently has not been previously reported although it is a general property of all strongly anisotropic ($|\epsilon_x - \epsilon_z| \gg 0$) transparent crystals. The existence of this effect makes it possible for some longitudinal dielectric resonances (zeros of the dielectric response function) to be studied in transmission as if they were weak transverse resonances as well as identifying intrinsic but otherwise spurious absorption and reflection bands which are due to a slight misalignment of an anisotropic crystal with strong longitudinal resonances. An observation in transmission of the lowest LO frequency of the ϵ_x component of the tysonite lanthanide fluorides is reported in Chapter III.

CHAPTER III

THE TYSONITE LATTICE

3.1 General Physical Properties

Various chemical and physical properties of compounds of the lanthanide and actinide elements have been under continuing investigation for many years. (See for example references 28 to 32.) As shown in Figure 3.1 for the lanthanide fluorides, each substance shows a rather pronounced lanthanide contraction as the atomic number of the cation is increased and the additional electrons enter an inner f-electron shell. The lanthanide fluorides are especially interesting because they have a different crystal structure and are much more rugged than the other lanthanide halides. Whereas the chlorides and bromides of both the lanthanide and actinide elements crystallize with the hexagonal UCl_3 structure, the trigonal-hexagonal tysonite or LaF_3 structure appears to be the most stable form for the fluorides of La, Ce, Pr, Nd, and all of the actinide elements, as well as being a possible room temperature structure for the fluorides of Sm, Eu, Ho, and Th.⁽³³⁾ The actinide hydrides and the heavier lanthanide hydrides also crystallize in the form of tysonite.⁽³³⁾ However, as shown in Figure 3.1, the heavier lanthanide fluorides generally crystallize in the slightly less dense, orthorhombic YF_3 structure at room temperatures.⁽³³⁻³⁵⁾ At higher temperatures (transition temperature between $555^{\circ}C$ for SmF_3 and $1075^{\circ}C$ for

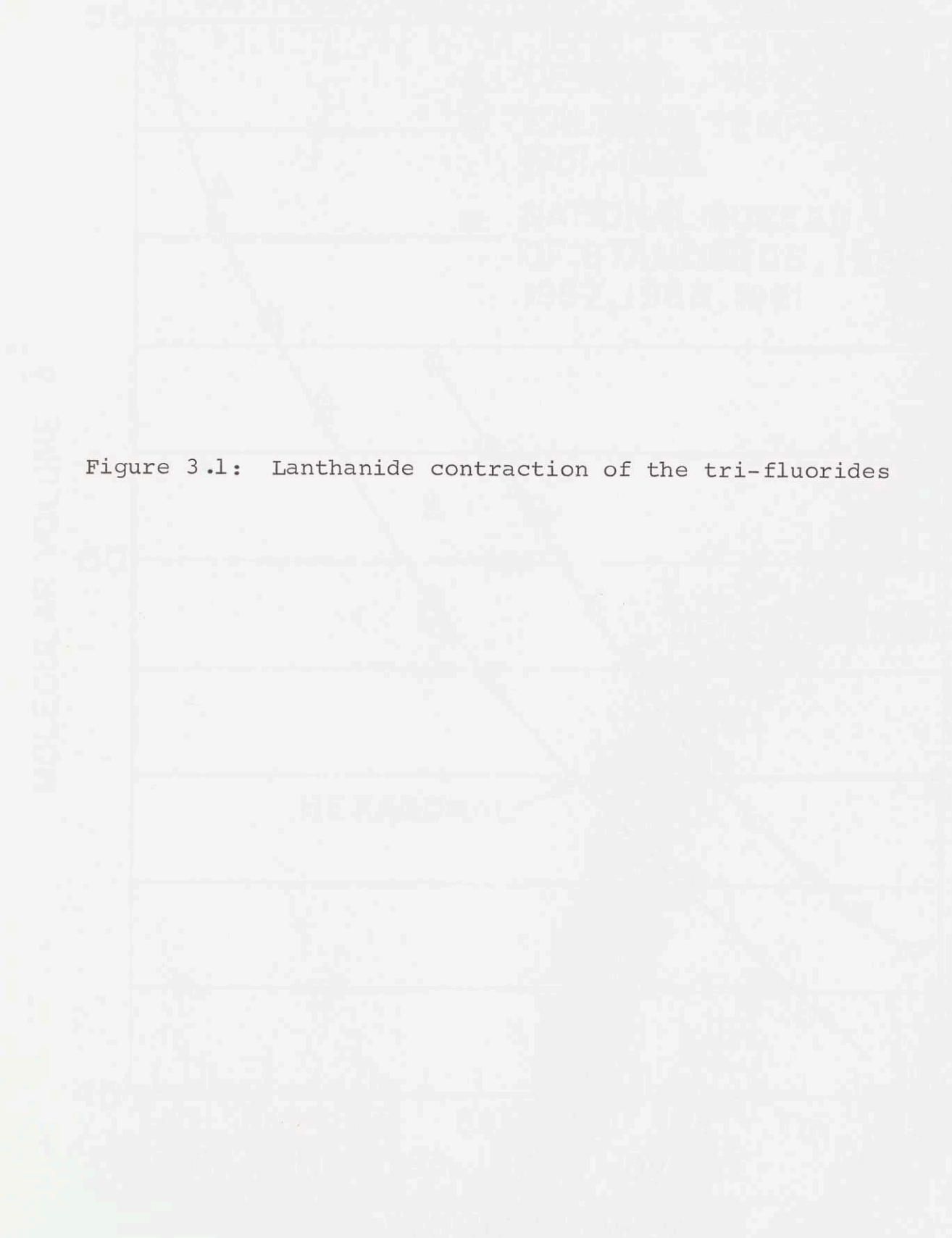
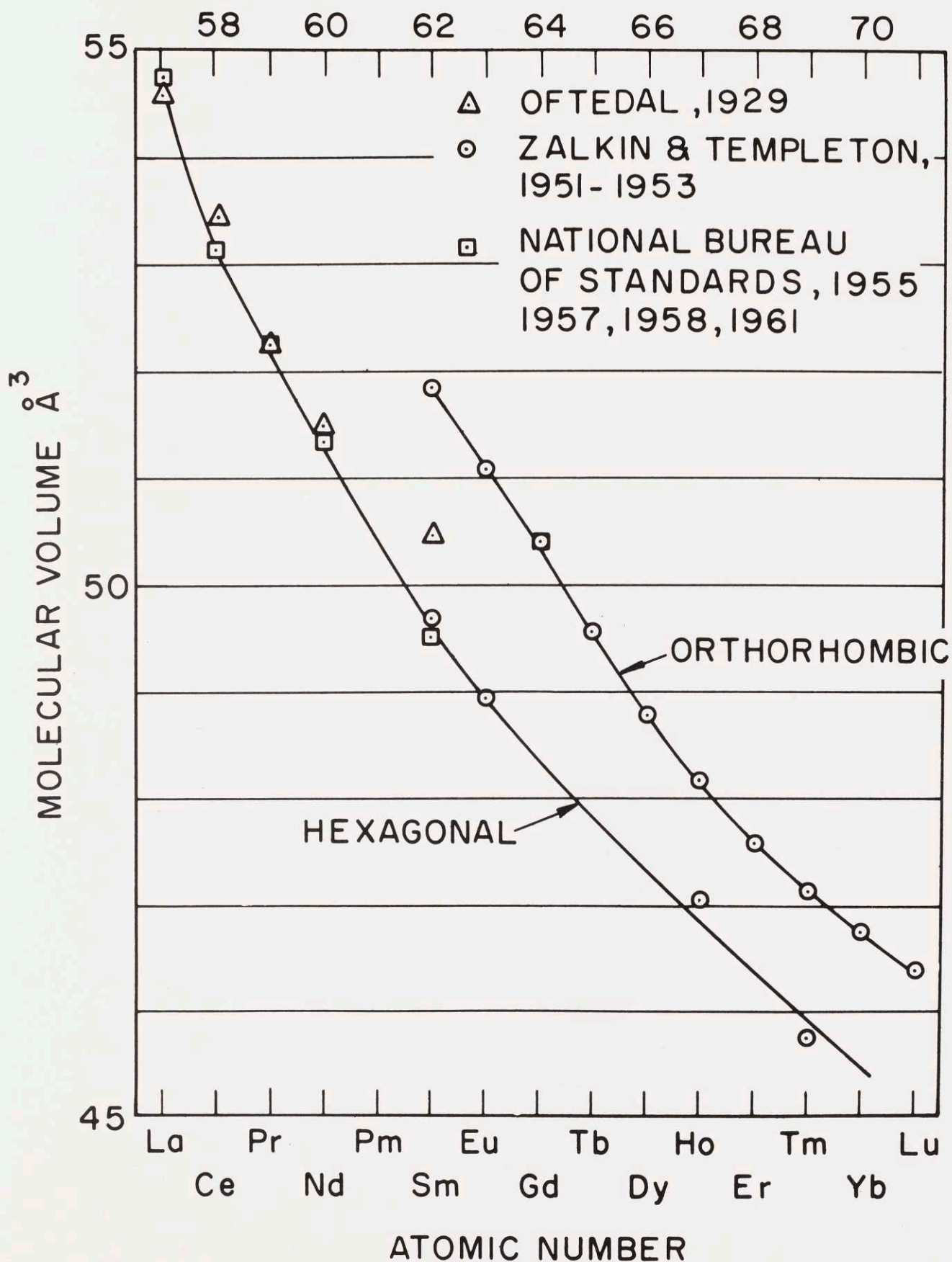


Figure 3.1: Lanthanide contraction of the tri-fluorides



ErF_3) the heavier lanthanide fluorides from SmF_3 through HoF_3 assume a trigonal-hexagonal structure identical with tysonite or LaF_3 at room temperature, and ErF_3 through LuF_3 assume a hexagonal, high temperature YF_3 structure. (36)

The lanthanide fluorides have a relatively high melting point (37) of 1200°K to 1500°K and a low electrical conductivity which appears to be due primarily to the migration of fluorine ions with an activation energy of 0.46 ev. (38) Whereas the chlorides and bromides tend to be rather soft and soluble, the fluorides are quite hard and insoluble in most common reagents. (3,4) Moreover, since soft glass (Corning 7570) wets LaF_3 and since LaF_3 and pure copper have similar coefficients of thermal expansion, it should be quite easy to fabricate heterogeneous structures from these materials. (4) Also, the four lightest lanthanide fluorides are all transparent from 250 nm through the visible region of the spectrum: (3) LaF_3 and CeF_3 are colorless, PrF_3 is green, and NdF_3 is a light purple or violet.

3.2 X-ray and Neutron Diffraction

Based upon powder X-ray diffraction patterns of the mineral tysonite, $(\text{Ce, La, ...})\text{F}_3$, and some artificially created tysonite lanthanide fluorides, the LaF_3 space group was first reported by Ivar Oftedal to be P6_322 (D_6^6) with six formula units per unit cell. (34) He also noted that the proposed locations of the

atoms in the unit cell were very close to those of a smaller, more symmetrical $P6_3/mmc$ (D_{6h}^4) pseudocell containing only two formula units per unit cell, and that the pseudocell was adequate to explain all but the weakest of the observed Bragg reflections. (34) However additional X-ray diffraction studies of single crystals of naturally occurring tysonite revealed more restrictive selection rules which convinced Oftedal that the proper space group must be $P6_3/mcm$ (D_{6h}^3) with six formula units per unit cell, despite the fact that the observed and calculated scattering intensities do not agree as well as they do in his $P6_3$ unit cell. (39)

Several subsequent studies of the X-ray diffraction of tysonite lanthanide fluoride powders refined the reported values of the lattice constants but did not significantly increase the available information on the tysonite lattice. (35,40-45) In fact, the $P6_3/mmc$ bimolecular pseudocell shown in Figure 3.9 was often listed as the LaF_3 structure. (33) Eventually, however, the apparent theoretical difficulties experienced by Oftedal were resolved by M. Mansmann (46,47) and independently by Allan Zalkin, David H. Templeton, and Ted E. Hopkins. (48) They observed that the tysonite lattice exhibits trigonal $\bar{3}m$ Laue-symmetry rather than hexagonal $6/mmm$ Laue-symmetry as previously reported. The space group was identified as $\bar{P}3c1$ (D_{3d}^4) and the atoms were located in almost the same

positions as those proposed by Oftedal for the $P6_322$ space group⁽³⁴⁾ except that the two layers of atoms in the unit cell are related by a glide plane operation rather than by a screw-axis operation. See Figure 3.8 for a plan view of the $\overline{P3}cl$ structure.

M. Mansmann and W. E. Wallace⁽⁴⁹⁾ have studied the lattice structure of tysonite HoD_3 by both X-ray diffraction and neutron diffraction. Again, satisfactory agreement between the observed and calculated scattering intensities is found only for the trigonal $\overline{P3}cl$ space group. However, Colette de Rango, Georges Tsoucaris, and Charles Zelwer conclude that the neutron diffraction of LaF_3 is most consistent with an hexagonal $P6_3cm$ (C_{6v}^3) lattice with six molecules per unit cell.⁽⁵⁰⁾

It should be noted here that, since X-ray and neutron diffraction are both invariant with respect to spatial inversion, it is not possible for them to distinguish space groups differing only by the presence or absence of the spatial inversion operator. Consequently, the noncentrosymmetric $\overline{P3}cl$ (C_{3v}^3) space group containing six formula units per unit cell is also consistent with the data reported above.

3.3 Bragg Diffraction of Light from Acoustic Phonons

Some features of a lattice structure can be determined from the propagation of ultrasonic waves through the crystal. It can be shown that a uniform solid may have up to twenty one

elastic constants relating the stress components to the strain components. However, the number of independent constants is greatly reduced by the presence of symmetry operations like rotations or reflections which move every atom in the crystal to an equivalent position. Solids belonging to the trigonal crystal class have six independent elastic constants governing the propagation of long wavelength acoustic phonons. Those in the hexagonal crystal class have only five independent elastic constants and are unique in that they exhibit acoustic isotropy in the basal plane. (51)

Since the wavelength of visible light (~500 nm) is much longer than the interatomic (~0.1 nm) or unit cell (~1nm) dimensions, it is possible to form a macroscopic three dimensional optical diffraction grating within a crystal by using ultrasonic waves of comparable wavelengths. By observing the Bragg diffraction of a single-mode He-Ne 632.8 nm laser beam by acoustic wave pulses in the 200-800 MHz frequency region, Charles Krischer has measured the velocity of propagation of transverse acoustic phonons in the basal plane of LaF_3 . (52)

With the propagation vector, k , parallel to the x-axis of the crystal and the displacement vector, u , approximately parallel to the y-axis: $v_x^y = 2.788 \pm 0.002 \text{ Km/s}$. However, with $k \parallel y$ and $u \parallel x$: $v_y^x = 2.785 \pm 0.002 \text{ Km/s}$. The reported acoustic anisotropy, $v_x^y - v_y^x = 0.0034 \pm 0.001 \text{ Km/s}$, is much larger

than the experimental error. Moreover, similar measurements on crystal quartz show the expected acoustic isotropy.

Thus, due to the observed acoustic anisotropy, the tysonite lattice of LaF_3 can not belong to any of the proper hexagonal space groups. However, the results are consistent with any of the trigonal space groups even if they possess an hexagonal Bravais lattice like the $\overline{\text{P3c1}}$ structure proposed from the most recent X-ray diffraction studies.

3.4 Infrared and Raman Activity due to Optical Phonons: Previous Studies

Because the wavelength of visible and infrared radiation is much longer than the dimensions of the tysonite unit cell, macroscopic electromagnetic interactions with the lattice take place via long wavelength phonons near the center of the Brillouin zone ($k \approx 0$) or via multiphonon combinations for which $\sum_i k_i \approx 0$. Infrared active phonon transitions couple directly to the electromagnetic field and must therefore have the same transformation properties under the symmetry operations of the crystal class as does an electric dipole. Raman active phonon transitions, on the other hand, couple to both an incoming and outgoing, scattered photon and must therefore transform the same as a symmetric second order tensor (electric quadrupole). If the symmetry operations of a crystal class include the spatial

inversion operator, infrared active phonons and Raman active phonons must be distinct because an electric dipole has negative parity and a symmetric second order tensor has positive parity. However, in the absence of the spatial inversion operator, a phonon transition may be simultaneously infrared and Raman active depending upon what other symmetry operators are contained in the crystal class. A conventional group theoretical analysis of the space group and the symmetry sites occupied by the atoms in the unit cell can determine the total number of optically active fundamental phonon transitions and can predict which multiphonon transitions may or may not be optically active. Therefore, in addition to locating the critical frequencies of the electromagnetic interactions with the lattice, a very important result in itself, the infrared and Raman spectra complement one another and can be used to support or discredit the lattice structures proposed from X-ray and neutron diffraction measurements.

The frequencies of the infrared and Raman active lattice vibrations of powdered samples of LaF_3 were first measured at room temperature. Only a very few of the fundamental lattice modes were identified by H. H. Caspers, R. A. Buchanan, and H. R. Marlin,⁽⁵⁹⁾ and these unpolarized results were interpreted as supporting the bimolecular pseudocell lattice, at least as an approximate structure at room temperature.

More recent measurements of the Raman scattering of single crystals of the four lightest tysonite lanthanide fluorides, LaF_3 , CeF_3 , PrF_3 , and NdF_3 , by R. P. Bauman and S.P.S. Porto⁽⁵⁴⁾ show that only the strongest Raman bands can be considered characteristic of the bimolecular lattice. Four to five A-modes are consistently observed and at least eight E-modes are always observed in all four substances. By correlating all of the observations a total of five A-modes and twelve E-modes can be identified. Two very weak bands at 177 cm^{-1} and 192 cm^{-1} are attributed to multiphonon processes. Two sharp peaks at 395 cm^{-1} and 412 cm^{-1} are reported to be instrumental in origin.⁽⁵⁴⁾ Moreover, in addition to the lattice Raman scattering, three electronic Raman lines at 66, 94, and 537 cm^{-1} are observed at very low temperatures (20°K) due to the Pr^{3+} ion in PrF_3 . They conclude that the major features of the room temperature lattice Raman spectrum are explainable quite satisfactorily by assuming that the LaF_3 lattice is approximated by the hexagonal $\text{P6}_3/\text{mcm}$ with six formula units per unit cell, but that the precise selection rules and the number of Raman active frequencies are consistent with the proposed trigonal $\text{P}\bar{3}\text{c1}$ lattice and not with either of the hexagonal $6/\text{mmm}$ ($\text{D}_{6\text{h}}$) lattices.

Just after the polarized far infrared reflectance measurements reported in the next section were completed, H. E. Rast, H. H. Caspers, S. A. Miller, and R. A. Buchanan⁽⁵⁵⁾ published

the unpolarized, far infrared emittance of a single crystal of LaF_3 . They report the $k \approx 0$ transverse optical phonon frequencies for $k \parallel c$ (equivalent to the σ -polarization) to be at 92, 100, 115, 128, 166, 192, 208, 246, 272, 353, and 368 cm^{-1} and the additional frequencies for $k \perp c$ (mixture of σ -polarization and π -polarization) to be at 170, 203, 235, 264, and 304 cm^{-1} . In the σ -polarization, the emittance frequencies are, for the most part, quite close to those determined from the reflectance data. The exceptions are that neither the 92 cm^{-1} nor the 115 cm^{-1} transitions observed in the emittance spectrum can be seen in either reflectance or transmittance. Conversely, the emittance results show no sign of the phonon modes observed in reflectance just above and below the moderately strong band near 130 cm^{-1} .

In the π -polarization, however, the reported emission frequencies are not in good agreement with those observed in reflection, except for the strong lattice mode near 170 cm^{-1} . This is due to the fact that the emittance frequencies in the π -polarization were recorded with $k \perp c$ rather than with $E \parallel c$ as done in reflection. As a result, since the lanthanide fluorides are uniaxial and the dielectric response tensor contains two principal nondegenerate components, the emittance experiment simultaneously excited the infrared active modes in both orthogonal polarizations, yielding a strongly mixed

spectrum difficult to relate to the dielectric response function in either polarization. Consequently, due to the strongly anisotropic dielectric response of the tysonite lanthanide fluorides, the unpolarized emittance measurements did not identify all of the infrared active fundamental phonon modes of LaF_3 . For the most part, the frequencies and polarizations of the fundamental infrared active phonon modes of the four lightest lanthanide fluorides were not known prior to the publication of the results contained in the next two sections.

3.5 Infrared Activity due to Optical Phonons: Current Study

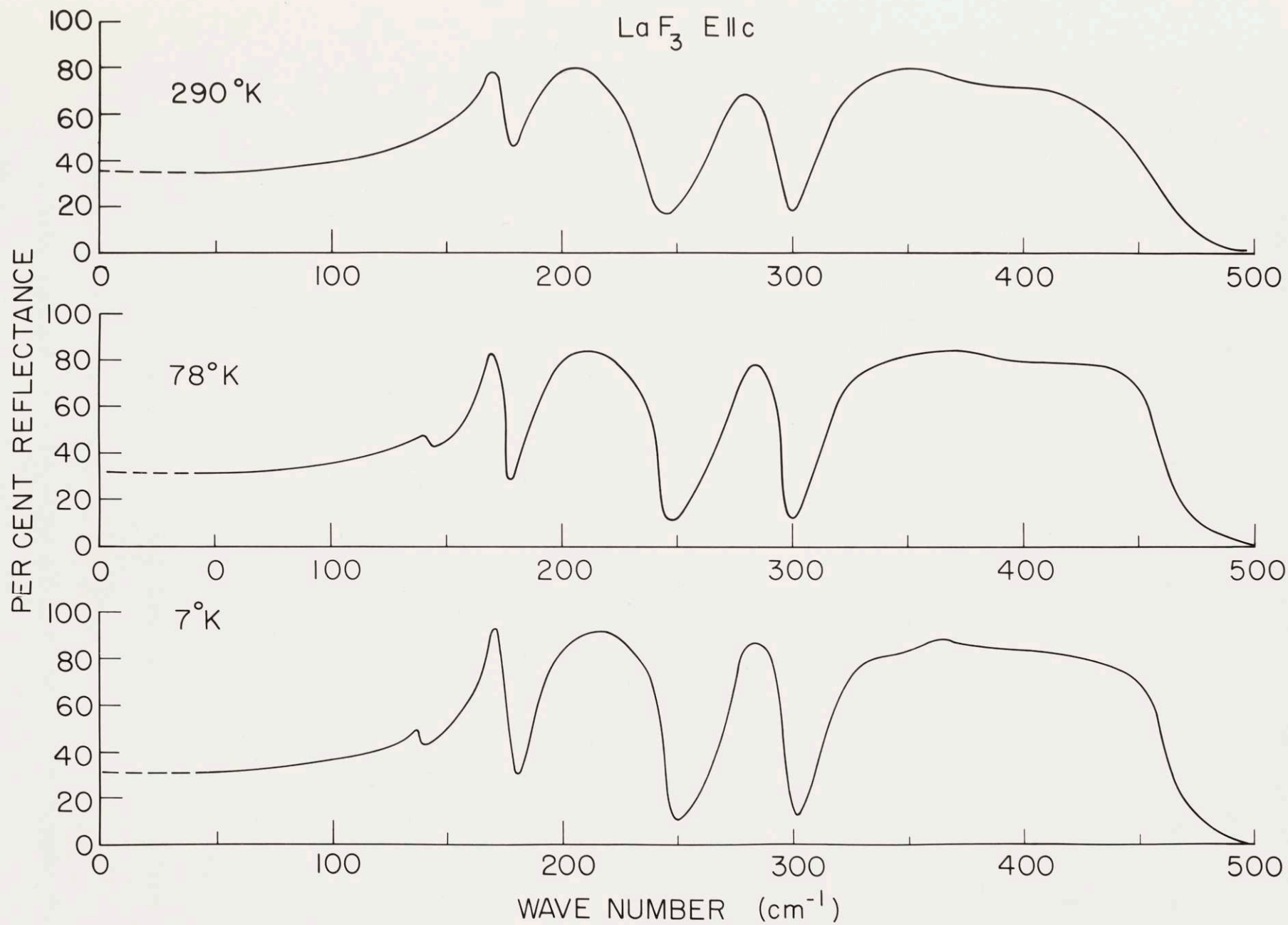
All of the far infrared spectra reported in this section were measured by means of Michelson interferometry using a modified R.I.I.C. FS-520 Fourier Spectrophotometer in the Spectroscopy Laboratory at M.I.T. The reflectance in both the π -polarization, $E||c$, and the σ -polarization, $E\perp c$, of the four lightest tysonite lanthanide fluorides was measured at 295°K , 78°K , and 7°K . Each of the composite spectra of LaF_3 and CeF_3 consist of two sets of measurements and cover the frequency region from 50 cm^{-1} to 500 cm^{-1} . Using the appropriate filters and background spectra, the first set of measurements cover the 50 cm^{-1} to 200 cm^{-1} region with the 0.5 mil (1 mil = 10^{-3} inch) beamsplitter and the second set covers the 150 cm^{-1} to 500 cm^{-1} region with the 0.15 mil beamsplitter. The PrF_3 spectra have

been extended to lower frequencies by a third set of measurements covering the 30 cm^{-1} to 90 cm^{-1} frequency region with the 1.0 mil beamsplitter. The NdF_3 spectra have been extended to both higher and lower frequencies by adding a fourth set of measurements covering the 250 cm^{-1} to 650 cm^{-1} region with the 0.15 mil beamsplitter, the Perkin Elmer interference filter, and the Perkin Elmer wire grid polarizer on a silver chloride substrate. The full set of reflectance measurements for these four substances in both polarizations and at all three fixed temperatures required many weeks of almost continuous observations by both the author and Professor R. P. Lowndes, who is now at Northeastern University. However, without the interferometer the measurements would have been even more difficult and tedious. Whereas the wide bandwidth interferometer provides at least a 50 cm^{-1} overlap between each beamsplitter and filter change, a comparable vacuum grating spectrometer would require at least four and up to six or more grating and filter changes in order to cover the same frequency region with minimal 10 cm^{-1} overlaps.

The spectra of LaF_3 shown in Figure 3.2 are typical of the reflectance of the tysonite lanthanide fluorides in the π -polarization as a function of temperature. At room temperature there are only four well defined peaks in the reflectance. The TO (transverse optical) frequencies of the peaks are near $170, 195, 275, \text{ and } 325 \text{ cm}^{-1}$. As the temperature is lowered to

Figure 3.2: Reflectance spectra of LaF_3 at 290°K , 78°K , and 7°K in the π -polarization

LaF₃ Ellc



that of liquid nitrogen all four peaks gradually sharpen and a fifth peak appears near 140 cm^{-1} . At the temperature of liquid helium the five bands sharpen slightly more. All of the changes appear to be gradual functions of temperature and there is no evidence for a phase change between 7°K and 300°K .

The low temperature, π -polarized reflectance spectra of the four lightest tysonite lanthanide fluorides are shown in Figure 3.3. The CeF_3 spectrum shows the same five reflectance peaks as observed for LaF_3 . The PrF_3 and NdF_3 spectra show not only the five reflectance peaks observed in LaF_3 and CeF_3 , but an additional feature near 235 cm^{-1} . The two features below 100 cm^{-1} , the 66 cm^{-1} peak in PrF_3 and the 45 cm^{-1} ripple in NdF_3 , have been associated with far infrared electronic transitions rather than lattice vibrations and are discussed in Chapter IV. Whereas the four lightest tysonite lanthanide fluorides exhibit only four strong reflectance bands in the π -polarization at room temperature, although there is the hint of a dip near 235 cm^{-1} in the room temperature reflectance of NdF_3 , the low temperature spectra show at least five and possibly six reflectance bands which can be associated with lattice vibrations. The TO and LO (longitudinal optical) frequencies and half-widths of five of these features have been extracted from the π -polarized reflectance spectra by means of Kramers-Kronig analysis and are listed in Table 3.1.

In a like manner, the spectra of LaF_3 shown in Figure 3.4

Figure 3.3: Low temperature π -polarized reflectance spectra of LaF_3 , CeF_3 , PrF_3 , and NdF_3

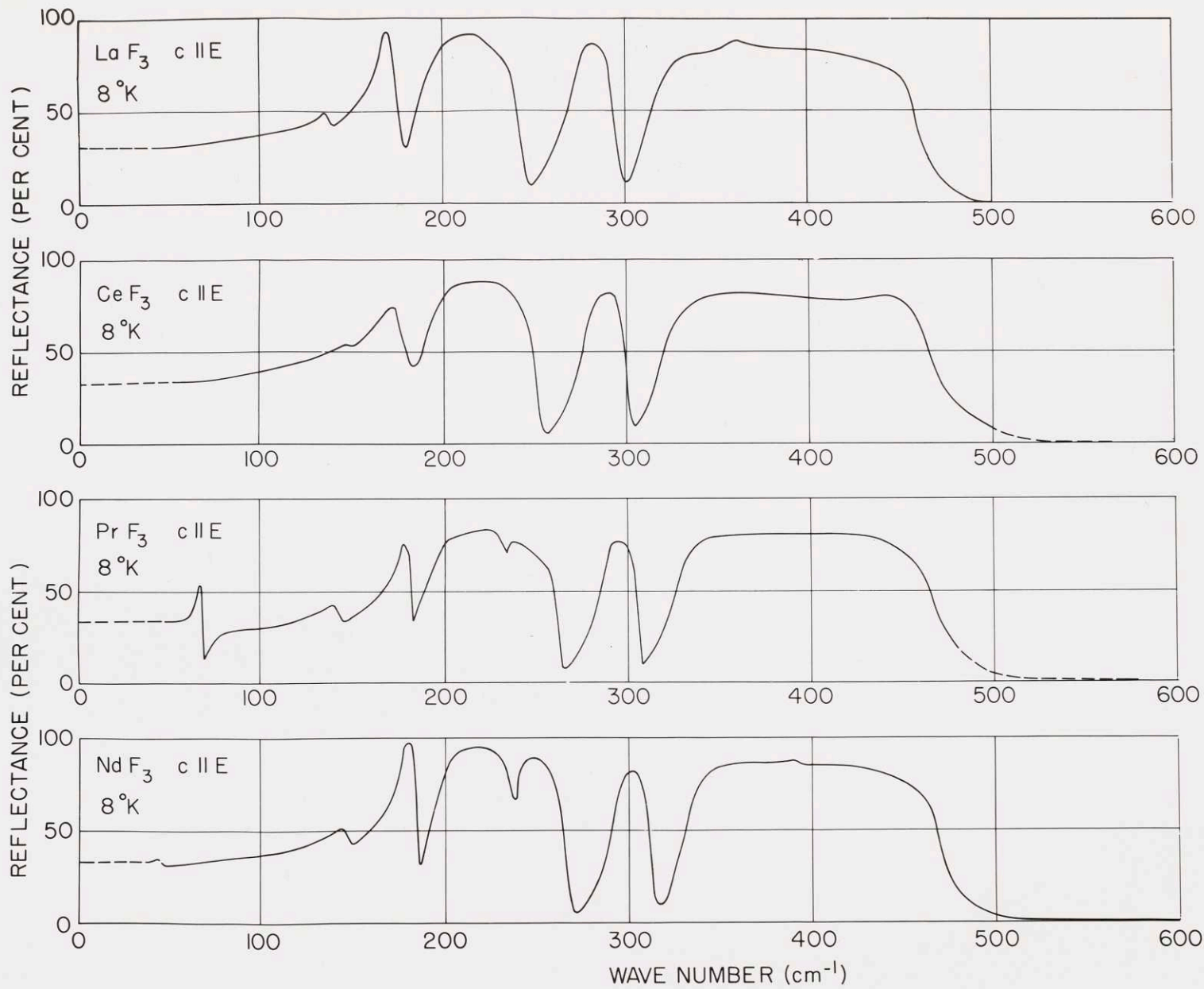
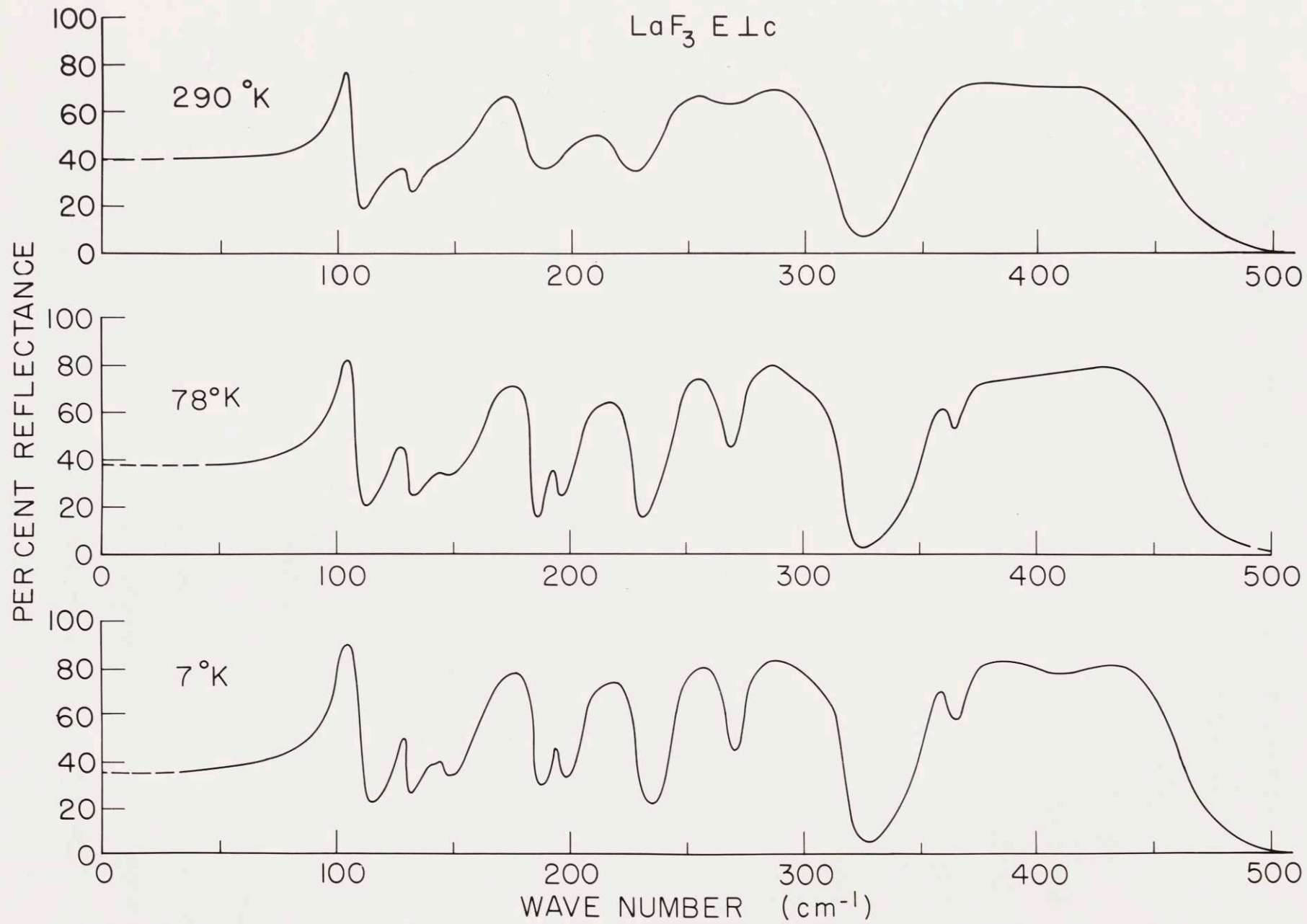


TABLE 3.1

Poles and zeros of the π -polarized dielectric response function-- A_{2u} lattice vibrations of the four lightest tysonite lanthanide fluorides

Mode	LaF ₃			CeF ₃			PrF ₃			NdF ₃		
	5	78	295 ^Q K	5	78	295 ^Q K	5	78	295 ^Q K	5	78	295 ^Q K
ω_T	138	142		140	141		141	141		144	147	
Γ_T	3	5		9	9		5	16		10		
ω_L	138	143		140	141		143	142		147	147	
Γ_L	4	5		8	8		5	17		10		
ω_T	166	168	168	170	170	167	178	175	170	176	177	172
Γ_T	4	4	6	5	6	10	3	9	16	5	4	8
ω_L	178	178	176	180	181	180	183	182	182	185	185	184
Γ_L	3	4	7	6	10	20	2	6	15	3	3	12
ω_T	194	195	194	199	203	193	201	203	195	202	202	198
Γ_T	8	9	14	8	11	24	10	17	20	6	7	15
ω_L	246	243	239	252	252	249	263	261	257	268	267	264
Γ_L	5	7	16	8	8	16	6	7	20	4	6	14
ω_T	273	274	275	280	285	273	289	288	283	294	294	290
Γ_T	8	10	12	3	6	20	6	8	20	4	6	17
ω_L	298	297	296	302	301	303	308	307	308	314	314	312
Γ_L	6	6	10	4	7	13	5	4	20	5	6	14
ω_T	318	319	323	329	329	321	331	332	329	335	337	337
Γ_T	14	14	16	6	14	18	8	15	20	8	8	12
ω_L	462	461	468	478	475	466	471	474	467	470	472	472
Γ_L	14	18	22	23	28	17	15	20	20	13	18	24

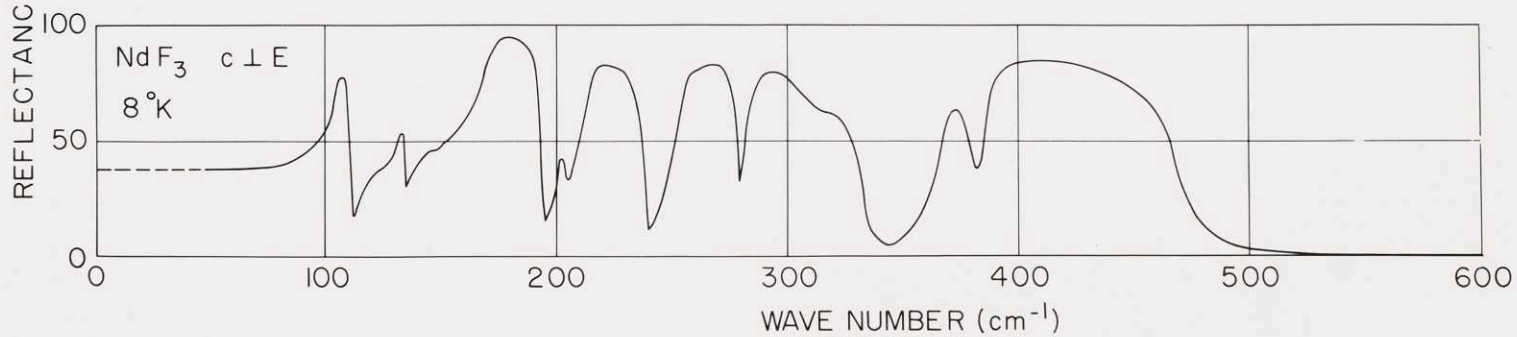
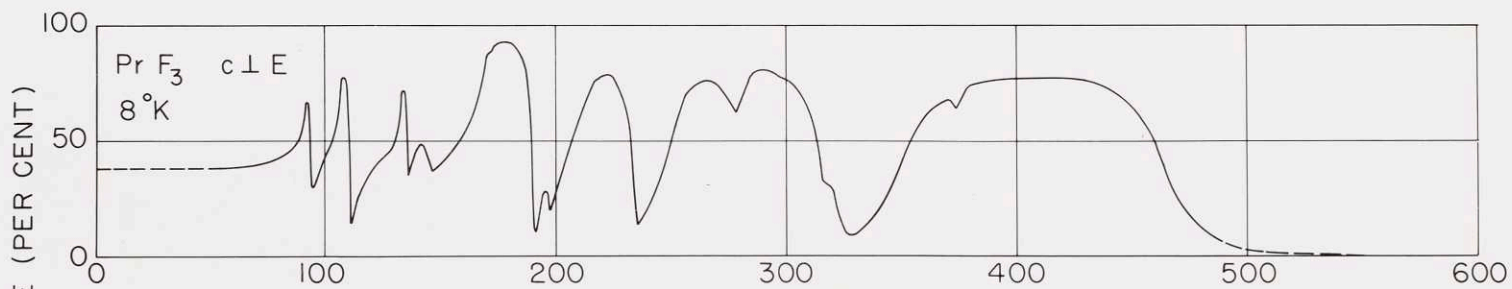
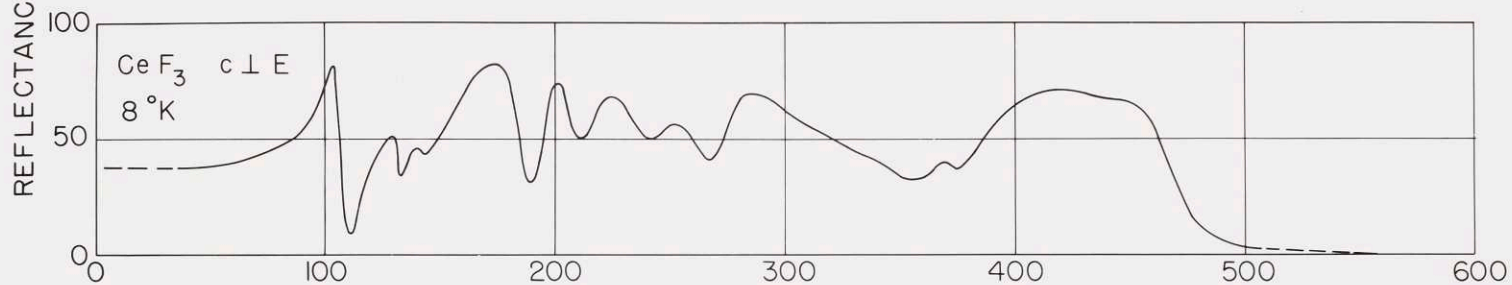
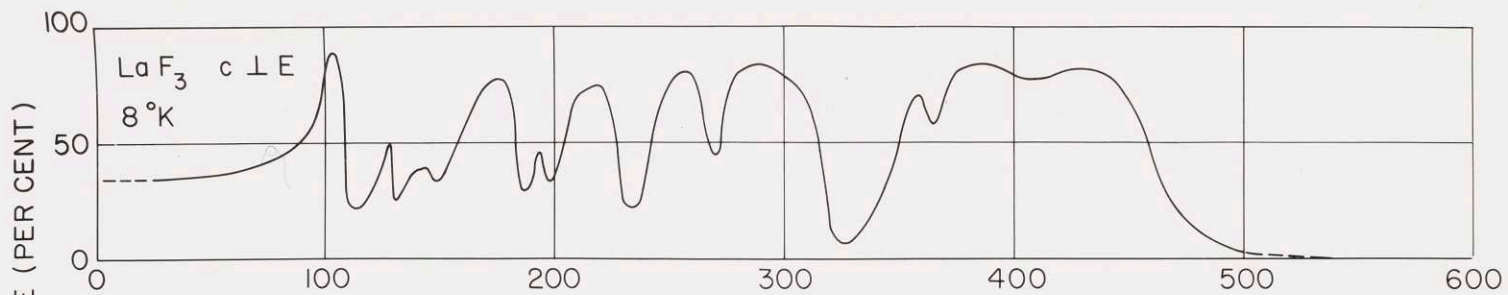
Figure 3.4: Reflectance spectra of LaF_3 at 290°K , 78°K , and 7°K in the σ -polarization



are typical of the reflectance of the tysonite lanthanide fluorides in the σ -polarization as a function of temperature. At room temperature there are six well defined peaks in the reflectance. The TO frequencies are near 100, 130, 170, 210, 245, and 355 cm^{-1} . In addition, however, two very weak and broad features near 145 cm^{-1} and 270 cm^{-1} are also discernable at room temperature. As the temperature is lowered to that of liquid nitrogen all of the previously mentioned features gradually sharpen and additional peaks appear near 195 cm^{-1} and 365 cm^{-1} . At the temperature of liquid helium a total of ten reflectance peaks can be easily seen.

As shown in Figure 3.5, the σ -polarized reflectance spectra of the four lightest tysonite lanthanide fluorides are quite similar. At least ten reflectance peaks due to lattice vibrations can be easily seen in each spectrum. The eleventh peak in the reflectance of PrF_3 at 92 cm^{-1} is due to an electronic transition as explained in Chapter IV. In addition to the above, the PrF_3 and NdF_3 spectra exhibit weak shoulders near 320 cm^{-1} , on the high frequency side of the 280 cm^{-1} reflectance peak, and near 125 cm^{-1} , on the low frequency side of the 134 cm^{-1} reflectance peak. The 125 cm^{-1} feature is also visible to some extent in the CeF_3 spectrum. Whereas the four lightest tysonite lanthanide fluorides exhibit only six strong reflectance bands in the σ -polarization at room temperature, at least ten and

Figure 3.5: Low temperature σ -polarized reflectance spectra of LaF_3 , CeF_3 , PrF_3 and NdF_3



possibly eleven or twelve lattice reflectance bands can be seen at low temperatures. The TO and LO frequencies and half-widths of ten of these features have been extracted from the σ -polarized reflectance spectra by means of Kramers-Kronig analysis and are listed in Table 3.2.

Since the lanthanide atomic weight increases by only 4% and the lattice volume decreases by only 5% in proceeding from LaF_3 through NdF_3 , the lattice reflectance spectra are quite similar. Consequently, only ten out of the total of twenty-four composite spectra have been explicitly displayed in the form of spectra. Nevertheless, all of the TO and LO frequencies extracted from the reflectance spectra at all three fixed temperatures are listed in Tables 3.1, 3.2, or 3.3.

Table 3.3 lists those reflectance features shown in Figures 3.3 and 3.5 which could not be associated conclusively with direct, first order coupling to the infrared active phonons of the tysonite lattice. The first three features listed are the electronic transitions of the Pr^{3+} ions in PrF_3 and the Nd^{3+} ions in NdF_3 which are discussed in more detail in Chapter IV.

It is conceivable that the dip in the π -polarized reflectance of PrF_3 and NdF_3 near 235 cm^{-1} may be due to the lifting of an accidental degeneracy of the reflection band at 220 cm^{-1} . However, this feature may also be associated with a σ -polarized

TABLE 3.2

Poles and zeros of the σ -polarized dielectric response function-- E_u
lattice vibrations of the four lightest tysonite lanthanide fluorides

Mode	LaF ₃			CeF ₃			PrF ₃			NdF ₃		
Mode	5	78	295 ^Q K	5	78	295 ^Q K	5	78	295 ^Q K	5	78	295 ^Q K
ω_T	101	100	100	98	98	100	107	104	102	104	105	101
Γ_T	2	7	5	6	6	7	3	4	6	3	6	8
ω_L	110	110	108	108	107	108	111	110	109	112	111	110
Γ_L	4	7	4	5	4	4	3	4	6	3	4	5
ω_T	128	127	128	130	130	130	134	132	131	133	133	131
Γ_T	3	8	8	4	4	7	2	5	13	3	4	
ω_L	130	131	130	132	132	132	136	135	133	135	135	136
Γ_L	3	7	7	3	4	7	2	6	10	3	4	20
ω_T	144	144		142			142	143		147		
Γ_T	11			5			8			6		
ω_L	146	145		142			145	143		147		
Γ_L	11			2			8			6		
ω_T	168	167	168	164	166	164	169	170	166	170	170	165
Γ_T	8	10	11	9	10	10	2	5	14	5	6	17
ω_L	184	184	183	186	186	186	189	189	190	194	194	193
Γ_L	5	5	18	8	7		2	3	14	3	4	14
ω_T	193	193		198	201		196			204	202	
Γ_T	10	7		6			4			4		
ω_L	196	195		210	208		197			204	202	
Γ_L	10						3			5		
ω_T	210	208	208	218	222	203	213	211	205	215	214	208
Γ_T	8	10	34				8	11		8	10	
ω_L	230	229	222	240	235	224	235	235	228	239	238	233
Γ_L	8	10	26				4	12		6	8	

TABLE 3.2
continued

Mode	LaF ₃			CeF ₃			PrF ₃			NdF ₃		
	5	78	295 ^Q K	5	78	295 ^Q K	5	78	295 ^Q K	5	78	295 ^Q K
ω_T	246	248	245	247	247	244	255	252	248	255	255	251
Γ_T	6	7	19				7	13	25	5	8	25
ω_L	268	268	272	264	266	272	278	276	278	279	279	278
Γ_L	9	12					20			5	12	
ω_T	274	272	268	276	278	269	280	278	278	283	284	278
Γ_T	8	13		20			10			5	11	
ω_L	318	317	316	350	350	318	323	322	324	334	334	332
Γ_L	10	10	16			34	15	16	25	12	16	23
ω_T	356	354	356	364		360	354	355	358	369	368	366
Γ_T	9	13	15			44	20	23	33	8	10	30
ω_L	364	364		374			373	373		381	381	380
Γ_L	15									10	12	33
ω_T	368	367		382	385		374	375		386	385	
Γ_T							16	20		9		
ω_L	466	462	457	472	474	478	468	464	467	471	471	463
Γ_L	31	29	35	26	33	72	16	23	33	18	20	30

TABLE 3.3

Miscellaneous features of the
dielectric response functions of the
four lightest tysonite lanthanide fluorides

Substance	Measurement	Description cm^{-1}	Identification
PrF_3	π -reflectance 5°K	$\omega_T = 66$ $\omega_L = 69$	Electronic transition of Pr^{3+} ion
PrF_3	σ -reflectance 5°K	$\omega_T = 92$ $\omega_L = 94$	Electronic transition of Pr^{3+} ion
NdF_3	π -reflectance 5°K	$\omega_T = 45$ $\omega_L = 46$	Electronic transition of Nd^{3+} ion
PrF_3	σ -reflectance 5°K	$\omega_T \approx \omega_L \approx 127$ $\omega_T \approx \omega_L \approx 317$	Uncertain, possibly fundamental or multi-
NdF_3	σ -reflectance 5°K	$\omega_T \approx \omega_L \approx 121$ $\omega_T \approx \omega_L \approx 315$	phonon lattice modes of tysonite
PrF_3	π -reflectance 5°K 78°K	$\omega_T \approx \omega_L \approx 234$ $\omega_T \approx \omega_L \approx 232$	Spurious π -reflectance feature associated with ω_L (zero) of ϵ_x . See
NdF_3	π -reflectance 5°K 78°K 295°K	$\omega_T \approx \omega_L \approx 239$ $\omega_T \approx \omega_L \approx 237$ $\omega_T \approx \omega_L \approx 235$	Table 3.2 for direct observation in the σ -reflectance spectrum
LaF_3	π -transmittance	opaque 28-32	π -polarized, fundamental,
CeF_3	5°K	opaque 30-34	infrared active lattice
PrF_3		opaque 37-41	mode of tysonite
NdF_3		opaque 32-36	

longitudinal frequency listed in Table 3.2. As discussed in the preceding chapter, a slight misalignment of the crystal axes of the uniaxial crystal causes the effective dielectric response function associated with the extraordinary ray (anything other than perfect $E_{\parallel c}$ or σ -polarized rays) to have zeros at all of the zeros of both $\epsilon_z(\omega)$ and $\epsilon_x(\omega)$. For small angles, the strength of the additional zeros is proportional to the square of the angle of misalignment, and since the effective dielectric response function must have the same number of poles as zeros, each of the weak zeros has a weak pole very close to it. This weak but direct, infrared active coupling to the longitudinal frequencies of $\epsilon_x(\omega)$ can cause spurious features in the experimentally measured π -polarized reflectance or transmittance, which are functions only of $\epsilon_z(\omega)$ for perfectly aligned crystals. In addition to this probably spurious dip in the reflectance near 235 cm^{-1} , a small ripple in the π -polarized reflectance is detectible near 108 cm^{-1} . As discussed below, this latter feature has also been observed in transmission and has been associated conclusively with the lowest frequency σ -polarized longitudinal frequency listed in Table 3.2.

The 125 cm^{-1} feature in the low temperature σ -polarized reflectance is possibly an infrared active fundamental phonon mode. Unfortunately, whereas the ten modes listed in Table 3.2

can be identified as fundamental phonon modes merely on the basis of their strong infrared activity, this latter band is rather weak and is not easily visible in all four substances. On the other hand, the feature near 315 cm^{-1} in the σ -polarized reflectance of NdF_3 , which is only slightly weaker than the tentatively identified eleventh fundamental phonon mode at 125 cm^{-1} , is suspiciously close to and slightly above a longitudinal frequency of $\epsilon_z(\omega)$ listed in Table 3.1. Higher order terms in the experimentally measured σ -polarized reflectance involving both the angle of incidence and the angle of misalignment may lead to measurable effects near the zeros of ϵ_z or $(\epsilon_z - 1)$ and could explain this feature. However, it is also quite possible that the 315 cm^{-1} feature may be due to a strong second order multiphonon mode of the lattice. The identification of both of these features is rather uncertain and speculative and neither of them can be conclusively identified as first order infrared active fundamental phonon modes, higher order infrared active phonon modes, or spurious effects due to impurities or due to the geometry of observation.

Figures 3.6 and 3.7 show the low temperature absorption coefficient spectra of LaF_3 and CeF_3 in both polarizations between 25 cm^{-1} and 150 cm^{-1} . A very strong, totally polarized absorption band between 95 cm^{-1} and 112 cm^{-1} dominates the σ -polarized spectra. Clearly it is associated with the lowest

Figure 3.6: Low temperature absorption coefficient spectra
of LaF_3

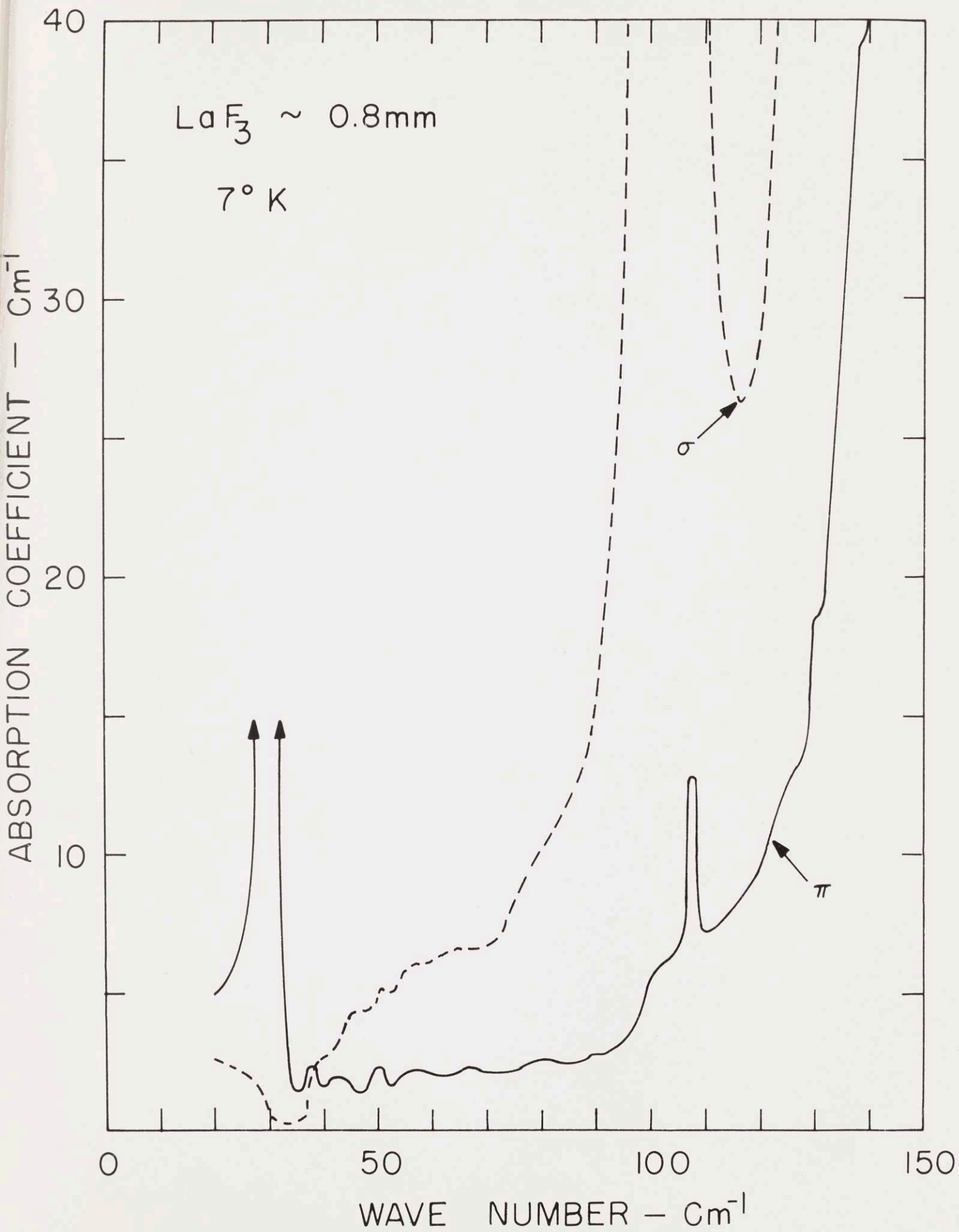
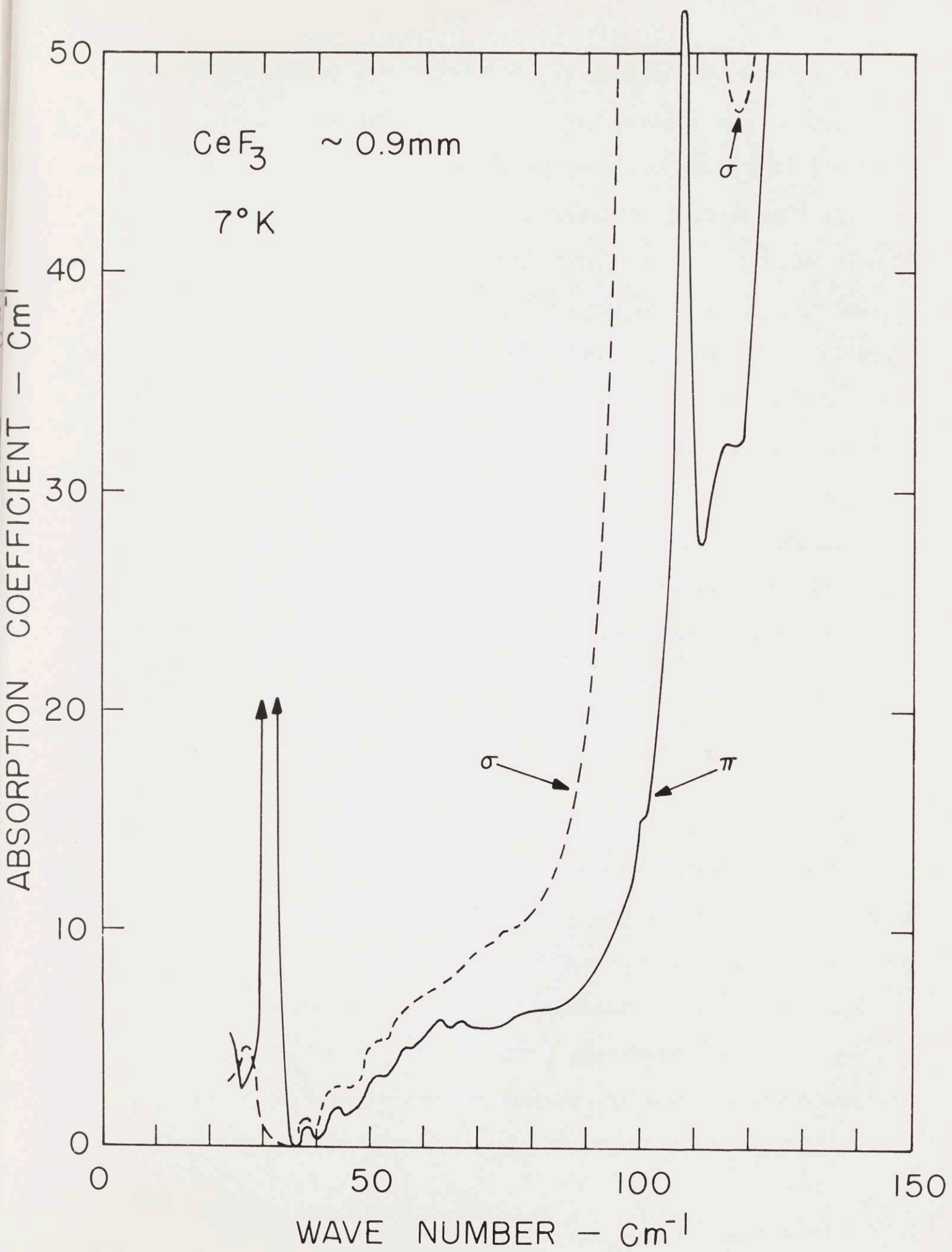


Figure 3.7: Low temperature absorption coefficient spectra of CeF_3



frequency infrared active fundamental phonon mode visible in the σ -polarized reflectance. A similar feature near 30 cm^{-1} is visible in the π -polarized absorption spectra. This latter absorption band is consistently observed between 28 cm^{-1} and 32 cm^{-1} in LaF_3 , 30 cm^{-1} and 34 cm^{-1} in CeF_3 , 37 cm^{-1} and 41 cm^{-1} in PrF_3 , and 32 cm^{-1} and 36.5 cm^{-1} in NdF_3 independent of any lanthanide dopants in the crystal. Based upon the proportionality between the experimentally measured width of a totally absorbing line and the square root of the optical strength of the absorbing transition,⁽⁵⁶⁾ this 30 cm^{-1} band in the π -polarization is approximately one tenth as strong as the fundamental phonon mode identified at 100 cm^{-1} in the σ -polarization. Therefore, it is quite possibly due to a very low frequency π -polarized fundamental phonon mode of the tysonite lattice although it is slightly weaker than expected and other explanations are conceivable.

The rather sharp, π -polarized absorption bands at 107.7 cm^{-1} in LaF_3 and 107.5 cm^{-1} in CeF_3 with half-widths of approximately 2 cm^{-1} and 4 cm^{-1} respectively, are due to the σ -polarized longitudinal optical phonon frequencies listed in Table 3.2, which are observed in reflectance measurements to lie between 108 and 110 cm^{-1} with half-widths of approximately 3 to 5 cm^{-1} . As explained in the preceding chapter, this weak absorption due to the longitudinal mode varies in strength from sample to sample

and is seen only because the crystal c-axis is slightly misaligned from the exact $E \parallel c$ and $k \perp c$ requirements for the π -polarization. The ratio of the reduced strength measured in transmission to the full strength measured in reflection suggests that the angle of misalignment is approximately 2.6 arc-degrees in the LaF_3 sample and 5.4 arc-degrees in the CeF_3 sample. An equivalent feature can be seen in the π -polarized transmittance of PrF_3 at 111.5 cm^{-1} and NdF_3 at 111.0 cm^{-1} .

No other first order absorption bands are observed below 120 cm^{-1} in the undoped spectra of LaF_3 and CeF_3 , but several higher order absorptions could be detected. The PrF_3 and NdF_3 spectra show their respective first order electronic transitions in addition to the features visible in the LaF_3 and CeF_3 spectra. The most consistent weak absorptions (peak absorption coefficient less than 5 cm^{-1} were generally unpolarized and were observed near 26, 38, 45, 50, 56, 65, 72, 79, 82, and 100 cm^{-1} in LaF_3 . The 72 cm^{-1} feature is most likely due to uncompensated polyethylene absorption. The one at 100 cm^{-1} shows only in the π -polarization and may be associated with the lowest frequency TO frequency in the σ -polarization. Otherwise, not all of these weak absorptions were always observed in all four substances or in different samples of the same substance.

3.6 The Lattice Space Group

Tables 3.1 and 3.2 reveal that the frequency of any particular lattice mode in LaF_3 generally moves to higher frequencies in the heavier lattices. This may reflect the stronger interionic forces present in the heavier lattice due to the lanthanide contraction of the cell volume as the atomic number of the cation is increased.

A comparison of the phonon frequencies identified from the current infrared measurements with the Raman active phonon frequencies reported by Bauman and Porto⁽⁵⁴⁾ show that all of the A_{1g} Raman active frequencies are distinct from all of the infrared active TO and LO frequencies. However, some of the Raman active E_g modes seem to be almost degenerate with infrared active modes. There is a rather strong clustering of weakly active infrared and Raman frequencies near 145 cm^{-1} in which an A_{1u} and an E_u infrared active mode are within 5 cm^{-1} of two E_g Raman active modes. Also, the two high frequency modes described as E_{2g} of D_{6h} by Bauman and Porto lie very close to the LO frequencies of two E_u modes listed in Table 3.2.2. Otherwise, the Raman active frequencies appear quite distinct from the infrared active ones, and none of the infrared active frequencies appear to remain consistently within 1 cm^{-1} of a given Raman active mode in all four substances.

Since there are 34 infrared active frequencies (counting both TO and LO frequencies) and 17 Raman active frequencies observed below 500 cm^{-1} , it would not be surprising if one or more distinct modes accidentally lay within a 5 cm^{-1} interval. Consequently, the most recent infrared and Raman measurements have been interpreted as strongly supporting a structure which includes inversion symmetry, although the accuracy of the measurements is not better than 1 cm^{-1} and a noncentrosymmetric structure can not be conclusively eliminated as a remote possibility.

Table 3.4 summarizes some results of a group theoretical vibrational analysis of several structures proposed for the tysonite lattice from X-ray diffraction studies. The low temperature infrared reflectance measurements reveal the existence of at least five and possibly six infrared active modes in the π -polarization and at least ten and possibly eleven or twelve infrared active modes in the σ -polarization. Therefore, the $P6_3/mmc$ (D_{6h}^4) lattice which predicts two π -polarized and two σ -polarized infrared active modes and the $P6_3/mcm$ (D_{6h}^3) lattice which predicts four π -polarized and seven σ -polarized infrared active modes can both be eliminated as possible tysonite lattices. The $P\bar{3}c1$ (D_{3d}^4), $P6_322$ (D_6^6), and $P6_3cm$ (C_{6v}^3) lattices, on the other hand, are all compatible with the infrared measurements. Nevertheless, the $P6_322$ and $P6_3cm$ lattices can be eliminated because group theory predicts almost twice as many

doubly degenerate Raman active modes as observed. (54) Moreover, all eleven of the g-polarized infrared active modes of the P6₃22 structure and all infrared active modes of the

TABLE 3.4
Number of optically active phonons
in the proposed tysonite lattices

Lattice space group	Formula units	Lanthanide site symmetry	Optical activity*			
			IR- π	Raman-A	IR- σ	Raman-E
P6 ₃ /mmc (D _{6h} ⁴)	2	$\bar{6}m2$ (D _{3h})	2A _{2u}	1A _{1g}	2E _{1u}	1E _{1g} 3E _{2g}
P6 ₃ /mcm (D _{6h} ³)	6	mm (C _{2v})	4A _{2u}	3A _{1g}	7E _{1u}	4E _{1g} 8E _{2g}
P $\bar{3}c1$ (D _{3d} ⁴)	6	2 (C ₂)	6A _{2u}	5A _{1g}	11E _u	12E _g
P6 ₃ 22 (D ₆ ³⁶)	6	2 (C ₂)	6A ₂	5A ₁	11E ₁	11E ₁ 12E ₂
P6 ₃ cm (C _{6v} ³)	6	m (C _s)	7A ₁		11E ₁	11E ₁ 12E ₂
P3c1 (C _{3v} ³)	6	1 (C ₁)	11A ₁			23E

* IR = infrared active; Raman = Raman active; A = nondegenerate
E = doubly degenerate; $\pi = \vec{E} \parallel \vec{c}$; $\sigma = \vec{E} \perp \vec{c}$.

As mentioned earlier, the difference between the P6₃/mcm and the P $\bar{3}c1$ lattice is determined only by small displacements and the physical properties of tysonite may be dominated by features characteristic of the approximate P6₃/mcm lattice.

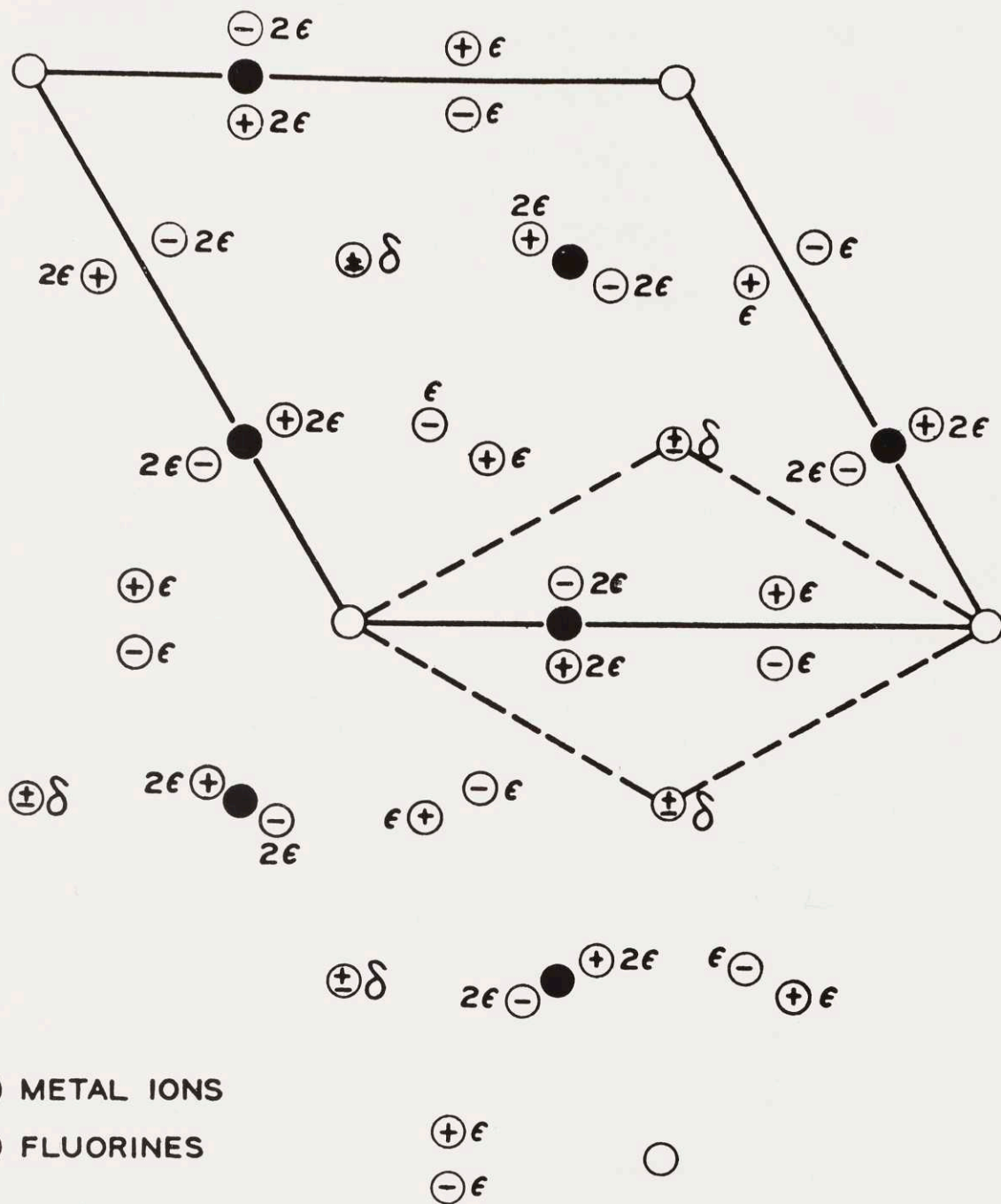
doubly degenerate Raman active modes as observed.⁽⁵⁴⁾ Moreover, all eleven of the σ -polarized infrared active modes of the $P6_3 22$ structure and all of the infrared active modes of the $P6_3$ cm structure should be both infrared and Raman active. Likewise, although it is consistent with the most recent X-ray studies,⁽⁴⁶⁻⁴⁸⁾ the noncentrosymmetric $P3cl$ (C_{3v}^1) lattice can be eliminated by either infrared or Raman studies. Only the $\bar{P}3cl$ lattice seems to be consistent with both infrared and Raman measurements.

In addition to adequately explaining the optically active phonon spectrum, the $\bar{P}3cl$ lattice has a lanthanide ion site symmetry low enough to be compatible with all of the reported optical absorption measurements discussed in the next chapter and has fluorine ion sites compatible with the spectra of H^- and D^- impurities in the lattice.⁽⁵⁷⁾ Those experiments in which polarized or partially polarized electronic spectra have been observed do not necessarily contradict the low site symmetry found in the $\bar{P}3cl$ lattice, since the lower site symmetry merely allows unpolarized transitions and the depolarization of a given transition may not easily be measurable.

As mentioned earlier, the difference between the $P6_3/mcm$ and the $\bar{P}3cl$ lattice is determined only by small displacements and the physical properties of tysonite may be dominated by features characteristic of the approximate $P6_3/mcm$ lattice.

A plan view of the $\overline{P3}cl$ unit cell is shown in Figure 3.8.⁽⁵⁴⁾ Using the Wyckoff labels⁽⁵⁸⁾ for the equivalent lattice sites, the $P6_3/mcm$ lattice can be generated from the $\overline{P3}cl$ lattice by displacing the four "d" fluorines by 0.46 \AA ⁽⁴⁸⁾ so that they lie in horizontal mirror planes perpendicular to the c-axis at $z = \pm \frac{1}{4}$ lattice units and by displacing the twelve "g" fluorines by 0.04 \AA ⁽⁴⁸⁾ so that they are contained within vertical mirror planes passing through the origin and the lanthanide ions. The net result of these displacements from the more symmetric $P6_3/mcm$ structure is that two B_{2u} infrared inactive modes and the four A_{2u} infrared active modes of the D_{6h} group combine to form the six A_{2u} infrared active modes of the D_{3d} group. Four inactive E_{2u} modes and the seven active E_{1u} modes of D_{6h} combine to form the eleven E_u modes of D_{3d} . Therefore, the infrared spectrum associated with the $\overline{P3}cl$ lattice may be expected to consist of four π -polarized and seven σ -polarized strong reflection bands, characteristic of the $P6_3/mcm$ lattice, together with two more π -polarized and four more σ -polarized weaker reflection bands allowed only in the $\overline{P3}cl$ lattice. The experimental results confirm this and at $295^\circ K$ the weaker bands observed at lower temperatures are almost completely damped out leaving just the four π -polarized and seven σ -polarized strong infrared active modes. This result might also be expected because the small distances that differentiate between these two lattices are

Figure 3.8: Plan view of the $\overline{P3c1}$ structure proposed for tysonite. (54)

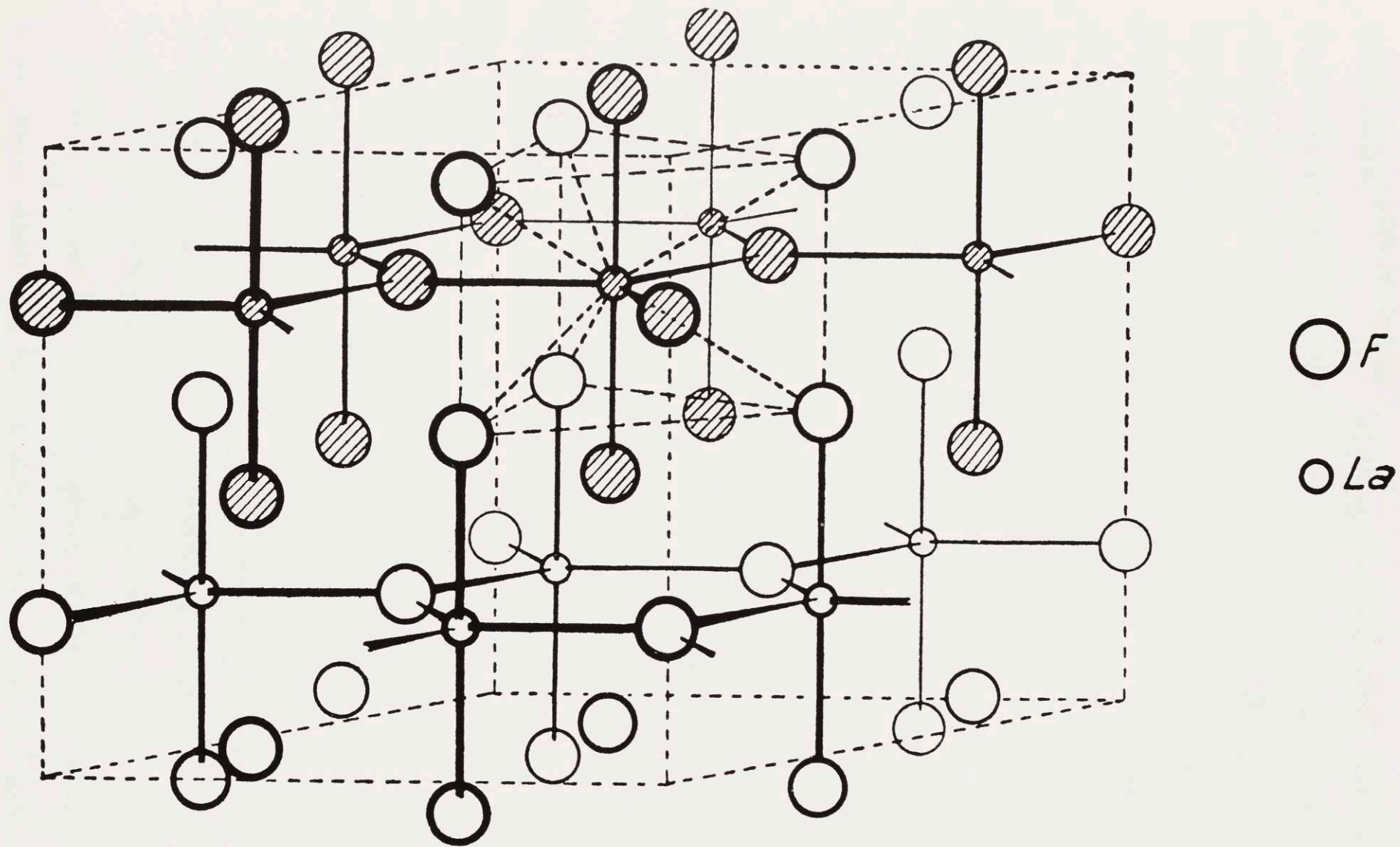


Unit cell of LaF_3 . The solid line outlines the hexamolecular unit cell, the dashed line the bimolecular cell (or "pseudocell"). The plane shown is $\frac{1}{4}$ lattice unit above the origins of Ref. 20 (pp. 271, 304), for simplicity of representation of position of ions, and the distances of fluorine atoms above or below this plane are indicated. ($\epsilon \approx \frac{1}{6}c$, $\delta \approx \frac{1}{16}c$)

comparable with typical vibrational amplitudes of ions in solids, and the increased amplitude of these vibrations as the temperature is raised would more strongly affect the weaker bands allowed only in the $\overline{P3}cl$ lattice.

Whereas the trigonal $\overline{P3}cl$ hexamolecular structure shown in Figure 3.8 offers a rather precise description of the tysonite lattice, due to the relatively small displacements distinguishing them, the hexagonal $P6_3/mcm$ hexamolecular structure is an exceptionally good approximation, especially at room temperature. This suggests a further approximation. The hexamolecular $P6_3/mcm$ structure shown in Figure 3.9⁽³³⁾ only by horizontal displacements of the six lanthanide ions by $0.05 \overset{\circ}{\text{A}}$ and of the twelve k-fluorines (g-fluorines in $\overline{P3}cl$) by $0.14 \overset{\circ}{\text{A}}$.⁽⁴⁸⁾ These displacements are comparable to those distinguishing the two hexamolecular structures. The principle difference is that the hexamolecular unit cells have three times as many phonon modes at the center of the Brillouin zone as the bimolecular unit cell. Assuming arbitrarily small displacements for which the infrared and Raman activities are negligibly small, the extra modes in the smaller hexamolecular Brillouin zone can be considered to be generated from interior regions of the bimolecular Brillouin zone being folded back to the center of the zone while other interior regions closer to the center of the zone are being projected out to the surface of the Brillouin zone. As the displacements approach those observed in X-ray

Figure 3.9: Bimolecular pseudocell of tysonite. ⁽³³⁾



The crystal structure of LaF_3

(34, 39, 46-48)
 diffraction, the nearly degenerate zone center phonon modes generated from the interior regions of the phonon branches of the bimolecular Brillouin zone will separate in frequency and the strengths of the infrared and Raman activities will increase. Quite possibly a detailed force constant calculation of the vibrational modes of the bimolecular $P6_3/mmc$ pseudocell and their relation to those of the hexamolecular $P6_3/mcm$ and $P\bar{3}c1$ structures could explain the diffuse clustering of zone center phonon modes above 300 cm^{-1} as well as the rather strong clustering of both infrared and Raman active modes near 145 cm^{-1} . Unfortunately, the required mathematical tools and computer programs necessary to handle up to 24 atoms and 72 normal modes in the unit cell are not available and the time required to generate them would have seriously detracted from the other results presented in this report.

Twelve nondegenerate optical phonon modes which are neither infrared nor Raman active are predicted for the $P\bar{3}c1$ structure. Five of them are A_{1u} modes of $\bar{3}m$ which are associated with two A_{1u} modes and three B_{1u} modes of the $6/mmm$ structure. They may become infrared active in the σ -polarization upon the application of an anisotropic stress or Raman active upon the application of an electric field perpendicular to the c-axis. The other seven silent modes are A_{2g} modes of $\bar{3}m$ which are associated with two A_{2g} modes and five B_{2g} modes of the $6/mmm$ structure. These latter modes may become Raman active upon the application

of an anisotropic stress or infrared active in the σ -polarization upon the application of an electric field perpendicular to the c-axis. Since the $\overline{P3c1}$ structure is so well approximated by the $P6_3/mcm$ structure it is likely that only the two modes described by A_{2g} of $6/mmm$ would become measurably infrared active upon the application of an electric field.

It is possible that some of the weak absorption bands observed in transmission below 120 cm^{-1} may be due to the nominally silent fundamental phonon modes of the tysonite lattice. The weak, extrinsic infrared activity of these intrinsically silent vibrational modes would be due to the higher order electric multipole moments of the electronic wavefunctions in the crystal which express the fact that the ions are not point charges in a perfect lattice: in other words, the extrinsic infrared activity is due to electron-phonon interactions. Such absorption bands would be the vibrational counterparts to the vibronic sidebands observed near pure electronic transitions. Because its strength seems to depend upon nearby electric dipole transitions, the absorption band near 50 cm^{-1} in LaF_3 has some of the group theoretical properties expected of one of the two vibrational modes described by A_{2g} of $6/mmm$, but it and the other weak absorptions reported in an earlier section are more probably due to the geometry of observation, multiphonon modes, or impurity and defect modes. Studies of the electric field

induced and strain induced infrared and Raman activities could confirm or deny any tentative assignment of the 50.5 cm^{-1} absorption band as well as locating some of the other optically inactive fundamental optical phonon modes.

At least five π -polarized and ten σ -polarized lattice reflectance bands have been observed in the spectra of the four highest tysonite lanthanide fluorides. The TO and LO frequencies are listed in Tables 3.1 and 3.2. These results together with the Raman scattering results⁽⁵⁴⁾ imply that the tysonite lattice is described most accurately by the trigonal-hexagonal $\bar{P}3c1$ hexamolecular structure proposed from the most recent X-ray diffraction studies.⁽⁴⁶⁻⁴⁸⁾ However the physical and optical properties are also very well approximated, at least at room temperature, by the hexagonal $P6_3/mcm$ hexamolecular structure proposed from earlier X-ray diffraction studies.⁽³⁹⁾ It also appears that the hexagonal $P6_3/mmc$ bimolecular structure⁽³⁴⁾ may be useful in understanding properties of the hexamolecular structures although it is not a very accurate approximation by itself. Tentatively, a sixth π -polarized A_{2u} mode near 30 cm^{-1} and an eleventh σ -polarized E_u mode near 125 cm^{-1} have also been identified, leaving unidentified only twelve nondegenerate fundamental phonon modes which are neither infrared nor Raman active to the first order.

CHAPTER IV

LANTHANIDE IONS IN TYSONITE

4.1 The Rare Earths

The lanthanide elements are characterized by the progressive filling of the 4f electron shell. In the normal configuration of the neutral lanthanides the spherically symmetric inner electronic core with the normal xenon configuration ($1s^2 2s^2 2p^6 3s^2 3p^6 3d^{10} 4s^2 4p^6 4d^{10} 5s^2 5p^6$) and any 4f electrons are surrounded by two or three outer electrons in a $6s^2$ or $5d6s^2$ configuration. M.G. Mayer,⁽⁵⁹⁾ R. Latter,⁽⁶⁰⁾ C.A. Coulson,⁽⁶¹⁾ and C.S. Sharma⁽⁶¹⁾ have shown that both the energy and the spatial extension of the 4f electronic eigenfunction drop suddenly at the commencement of the lanthanides. Whereas the 4f orbital wavefunction of lanthanum ($_{57}\text{La}$) has a theoretical energy of -0.95 eV and a maximum radial density outside the xenon core wavefunctions, the 4f orbital wavefunction of neodymium ($_{60}\text{Nd}$) has a theoretical energy of -5 eV and a maximum radial density well inside the $5s^2 2p^6$ electronic shells of the xenon core.⁽⁵⁹⁾ Thus the 4f electrons of the lanthanides behave as if they were entering an inner electron shell and tend to interact rather strongly with the nucleus while being well shielded from the external environment by the valence electrons and the outer electrons of the xenon core. In fact, other than their chemical similarity, one of the more striking properties of the lanthanides is the resulting

lanthanide contraction of the ions predicted theoretically⁽⁵⁹⁻⁶¹⁾ and illustrated in the preceding chapter (Figure 3.1). Lanthanum ($_{57}\text{La}$) is often included in the lanthanide series because it is chemically similar to the succeeding fourteen elements. However, the spectroscopically interesting series begins with cerium ($_{58}\text{Ce}$), which has a single 4f electron in both the neutral and triply ionized states, and ends with lutecium ($_{71}\text{Lu}$), which has a closed shell of fourteen 4f electrons.

The actinide elements are characterized by the progressive filling of the 5f electron shell. They have many properties analogous to the lanthanides and both groups of elements can be referred to as the rare earths. In the normal configuration of the neutral actinides the spherically symmetric inner electronic core with the normal radon configuration ($1s^2 2s^2 p^6 3s^2 p^6 d^{10} 4s^2 p^6 d^{10} f^{14} 5s^2 p^6 d^{10} 6s^2 p^6$) and any 5f electrons are surrounded by two or three outer electrons in a $7s^2$ or $6d7s^2$ configuration, except thorium ($_{90}\text{Th}$) which has four outer electrons in a $6d^2 7s^2$ configuration. At the beginning of the actinides the energy and spatial extension of the 5f electronic eigenfunction drop, but not quite as fast as they do for the 4f electronic eigenfunction of the lanthanides.⁽⁵⁹⁻⁶¹⁾ Due to the larger spatial extension of the 5f orbitals, the electron spin resonance of the actinide ion U^{3+} in CaF_2 shows hyperfine structure attributable to a significant overlap of the 5f

electronic eigenfunction with the nearby fluorine nuclei, whereas such an effect is not observed for the corresponding lanthanide ion, Nd^{3+} , in CaF_2 .⁽⁵²⁾ Due to the lower binding energy, neither neutral actinium ($_{89}\text{Ac}$) nor neutral thorium ($_{90}\text{Th}$) have any 5f electrons in their normal configurations. Nevertheless, the triply ionized state of thorium is spectroscopically interesting because it does have a single 5f electron and the actinide series ends with lawrencium ($_{103}\text{Lw}$), which has a closed shell of fourteen 5f electrons.

Because they are so well shielded from the external environment and have such a small effective radius (approximately 0.1 nm), the 4f electrons of the lanthanides and the 5f electrons of the actinides do not interact strongly with the other atoms in a crystalline or liquid environment. First order perturbation theory predicts that the mean energy of the LSJ levels of the $4f^n$ and $5f^n$ configurations should be independent of the host material: only the fine structure and widths of the transitions between these levels should depend strongly on the host material. As a result, the mean location of many of the absorption and emission bands observed in the spectra of rare earth compounds are at almost the same frequency as those observed in gaseous spectra of the same rare earth ions. These characteristic absorption and emission bands have been associated with $4f \rightarrow 4f$ and $5f \rightarrow 5f$ electronic transitions and the resulting mean energy levels of many different rare earth compounds have been

used to calculate the theoretical coupling coefficients for the electrostatic and spin-orbit interactions of the $4f^n$ and $5f^n$ configurations.

The energy levels of the d^n configurations of the transition metal ions are predicted very well by the L·S or Russell-Sanders coupling scheme, in which the spin-orbit splitting is small compared with the electrostatic interaction. In the f^n configurations, however, the spin-orbit splitting is much larger than for the d^n configurations and, although most of the energy levels of the $4f^n$ configurations can be predicted fairly well by L·S coupling, some of the energy levels of the $5f^n$ configuration can be predicted as well or better within the J·J coupling scheme, in which the electrostatic splitting is small compared with the spin-orbit interaction. The best energy level predictions have been based upon the intermediate coupling scheme, in which the entire set of electrostatic and spin-orbit matrices are diagonalized simultaneously. This arithmetically complicated approach, which uses all of the possible f^n energy levels, has yielded extremely good agreement between the theoretical and experimental energy levels of cerium ($Ce^{3+}, 4f^1$), ytterbium ($Yb^{3+}, 4f^{13}$), praseodymium ($Pr^{3+}, 4f^2$), thulium ($Tm^{3+}, 4f^{12}$), neodymium ($Nd^{3+}, 4f^3$), and erbium ($Er^{3+}, 4f^{11}$). (See for example, references 63 and 64.) Unfortunately, as shown in Table 4.1, the number of energy levels increases rapidly for the other f^n

configurations. Nevertheless, such calculations seem to be in progress for the rest of the f^n configurations and are expected to yield very good results. (See for example reference 65 on

TABLE 4.1

Group properties of the f^n configurations
(See for example reference 65 on 3d, 4f, etc.)

Configuration	Number of terms	Number of levels	Number of states
f^1 or f^{13}	1	2	14
f^2 or f^{12}	7	13	91
f^3 or f^{11}	17	41	364
f^4 or f^{10}	47	107	1001
f^5 or f^9	73	198	2002
f^6 or f^8	119	295	3003
f^7	119	327	3432

transitions between electronic states to differ by several hundred wavenumbers from the mean frequency predicted, but the mean frequencies are very useful for qualitative identification of lanthanide ions and for determining interesting regions of investigation. Transitions between the low lying LSJ levels of most of the lanthanides have been directly observed in the mid and near infrared in one or more host lattices, but until recently (see for example references 66-73) there has been almost no attempts to observed Raman active transitions between these levels.

Due to the vast amount of data available, weak first order, second order, and higher order effects have also been observed in addition to the moderately strong crystal field splitting.

configurations. Nevertheless, such calculations seem to be in progress for the rest of the f^n configurations and are expected to yield very good results. (See for example reference 65 on Gd^{3+} , $4f^7$.)

The approximate mean energy and the Russel-Saunders labels for the energy levels of the trivalent lanthanide ions can be found in the extensive literature covering the infrared, visible, and ultraviolet absorbance and fluorescence spectra of rare earth compounds: the references listed⁽²⁸⁻³¹⁾ are merely representative and can not be considered exhaustive. Crystal field interactions and other fine structure may cause individual transitions between electronic states to differ by several hundred wavenumbers from the mean frequency predicted, but the mean frequencies are very useful for qualitative identification of lanthanide ions and for determining interesting regions of investigation. Transitions between the low lying LSJ levels of most of the lanthanides have been directly observed in the mid and near infrared in one or more host lattices, but until recently (see for example references 66-73) there has been almost no attempts to observed Raman active transitions between these levels.

Due to the vast amount of data available, weak first order, second order, and higher order effects have also been observed in addition to the moderately strong crystal field splitting.

The most widely acknowledged is the nephelauxetic (expansion) effect of the partially covalent bonds in nominally ionic crystals. E. Y. Wong, O. M. Stafsudd, and D. R. Johnston⁽⁷⁴⁾ have reported this effect in detail for the Pr^{3+} ion in LaF_3 , $\text{La}(\text{C}_2\text{H}_5\text{SO}_4)_3 \cdot 9\text{H}_2\text{O}$, LaCl_3 , LaBr_3 , and $\text{YAl}_3(\text{AlO}_4)_3$. As the nearest lanthanide neighbor changes from F to H_2O , Cl, Br, and O, the f orbitals expand and begin to participate more in covalent bonding. The Slater integrals change by approximately 2% between the Pr-F and Pr-Cl bonds and between the Pr-Cl and Pr-O bonds and the spin-orbit splitting decreases with the increasing covalency. The 3P_0 level of Pr^{3+} , for example, which is near 20900 cm^{-1} in LaF_3 moves approximately 500 cm^{-1} closer to the 3H_4 ground levels in LaCl_3 . If the Pr-F bond is assumed to be purely ionic (0% covalent), then the covalency, δ , of the Pr-Cl and Pr-Br bonds as defined by Wong et. al.⁽⁷⁴⁾ is approximately 1%. Similar results can also be shown for the other lanthanide ions.

However, the primary concern of this thesis is not the direct observation of transitions between the LSJ levels of the lanthanide ions by either infrared or Raman techniques. The rest of this thesis is concerned with the direct observation of far infrared active transitions between the Stark (crystal field) levels of a given LSJ multiplet in the tysonite lanthanide fluorides. The next section discusses the elements of the

theory of crystal field splitting for tysonite. This is followed by a report of the results of a preliminary survey of the far infrared properties of the tysonite lanthanide fluorides doped with various lanthanide ions.

4.2 Crystal Field Splitting

Three conventional models are used to calculate the splitting of the electronic degeneracies of an ion in a non-spherical electrical environment. The simplest is the crystal field model in which all other ions are considered to be described by point charges (or dipoles, etc.) located totally outside the central ion. These exterior electric charges create electric field gradients which remove the spherical degeneracies of electrons contained totally inside the central ion. In the ligand field model the degeneracies are removed by effective crystal field terms which are calculated from both internal and external charge distributions rather than exclusively from external point charges as in the pure crystal field model. The arithmetic of the ligand field model is similar to that in the crystal field model, except that first order corrections from both overlap and exchange integrals can be calculated with respect to the other ions. The molecular orbital model, basically a many body problem, is used primarily for the valence electrons of small molecules like CO_2 or the light hydrocarbons. The arithmetic can vary greatly from problem to problem and the methods

are not amenable to a simple discussion because, even in the first order, the electron no longer belongs to a given ion but is shared by many ions.

The experimentally observed splittings of the $4f^n$ energy levels of the lanthanide ions appear to be described rather well by the formalism of the crystal field or ligand field models. If the charges creating the local crystal field can be considered to be totally outside a region of radius R , as assumed in the crystal field model, it can be shown (see for example reference 75) that the local electric potential function, $U(r, \theta, \varphi)$, can be written in terms of the spherical harmonics, $Y_\ell^m(\theta, \varphi)$:

$$U(r, \theta, \varphi) = \sum_{\ell, m} a_{\ell m} \cdot r^{\ell+1} \cdot Y_\ell^m(\theta, \varphi) .$$

Given the $a_{\ell m}$'s and a naive approach to the energy perturbation problem, one can calculate the change in energy of the $4f$ electronic wavefunctions by calculating the integral $\int_V U \cdot \rho \cdot dV$ where ρ is the electronic density function or the square of the magnitude of the electronic wavefunction. However, since the ρ function of an f^n configuration is calculated from a wavefunction with orbital angular momentum up to $\ell = 12$ (1Q of f^6 and 2Q of f^7), it would seem that $U(r, \theta, \varphi)$ must contain spherical harmonics up to $\ell = 24$ for a complete description of the perturbation of the energy levels of some of the rare-earth ions.

Fortunately, the problem can be greatly simplified. If one is considering only first order effects based upon the central field approximation of the energy levels, the f electrons can be considered to be individuals--each one described by its own position and momentum. (56) The crystal field terms in the central field Hamiltonian can be written as a summation over the individual electrons labeled by the index k.

$$H_{\text{xtal}} = \sum_k e \cdot U(r_k, \theta_k, \varphi_k)$$

Matrix elements of the form $\langle LSJ | U | LSJ \rangle$ breakdown into sums of $\langle a | \langle f | U | f \rangle$ in which the wavefunction f contains orbital angular momenta no higher than $l=3$, so that the effective $U(r, \theta, \varphi)$ needs to contain spherical harmonic only up to $l=6$. Moreover, since all terms in a given configuration have the same parity, (28) only the positive parity terms of U (i.e. $l=0, 2, 4, 6$) can contribute to first order integrals. Local crystal site symmetry operations can limit the number of effective terms even further.

In fact, the site symmetry of the lanthanide ions in some crystals (like the lanthanide chlorides) is sufficiently high that the experimentally observed crystal field splitting of the f^n energy levels can be used to calculate a unique set of experimental amplitudes for the spherical harmonics in the electric potential function $U(r, \theta, \varphi)$. One can also calculate theoretical crystal field parameters from the mean positions of

the ions in the crystal as revealed by modern X-ray crystallographic techniques. Unfortunately, when these two independent calculations of the crystal field parameters are performed and the values are compared, it is found that the theoretical values of the $l=2$ terms are overestimated by a factor of ten, the $l=4$ terms are in approximate agreement, and the theoretical values of the $l=6$ terms are underestimated by a factor of ten. (76)

Most of the discrepancy between the experimental and theoretical values of the $l=2$ terms has been accounted for by linear electronic shielding. (76-80) Perturbation of the outer $5s^2 5p^6$ electrons of the xenon core make the largest contribution to the shielding of the low multipole electric field gradients, but additional contributions from the valence electrons and the inner core electrons can result in a theoretical shielding parameter of over 90%. Nevertheless, first order linear shielding does not account for all of the discrepancy in the $l=2$ terms and is completely inadequate to account for the apparent tenfold antishielding of the $l=6$ terms. Theoretical shielding parameters for the $l=4$ and $l=6$ terms are less than 20% and another mechanism must account for the discrepancies these higher order multipole terms.

Some improvement in the theoretical estimates of the $l=4$ and $l=6$ terms result from a reevaluation of $\langle r^4 \rangle$ and $\langle r^6 \rangle$ based upon the (nephelauxetic effect) expanded 4f wavefunctions in

the crystal lattice. (79-81) Other significant contributions come from the induced multipoles in the nearest neighbor ions. (76,82) However, Gerald Burns (82) has shown that the multipole approximation is not adequate or applicable because the ions are so close to one another that the extended nature of the induced charges must be taken into account. He also shows that the qualitative variation of the crystal field parameters as a function of nuclear charge and lattice parameters can be explained by assuming that all of the effective charge of a nearest neighbor ion lies on the surface of the ion.

The most effective technique for calculating theoretical values for the $\ell=6$ terms (and incidently for the $\ell=4$ and $\ell=2$ terms) within 10% of the experimental values has been developed by M. M. Ellis, D. J. Newman, S. S. Bishton, J. Smith, M. M. Curtis, and G. E. Stedman in a series of four papers. (83-86) They call it a contact approximation: Only interactions with the nearest neighbor ions are considered, all contributions from purely electrostatic charges on more distant ions are neglected. An effective ligand field at the expanded 4f wavefunction is calculated from a MO-LCAO (molecular orbital--linear combination of atomic orbitals) approximation of the coordinated valence electrons of a local ion complex $((\text{PrCl}_9)^{-6}$ for PrCl_3). The approximation represents a major breakthrough in understanding the physics of rare-earth crystal field splitting, but the

required MO-LCAO solution for the ligands is rather difficult and must be solved for the ion complex, if any, appropriate for the crystal lattice being studied. C. K. Jørgensen, R. Pappalardo, and H. H. Schmidtke⁽⁸⁷⁾ and later C. E. Schäffer and C. K. Jørgensen⁽⁸⁸⁾ have developed a special form of the contact approximation which represents the ligand electronic distributions by delta functions of position. The qualitative concepts inherent in the contact approximation are very helpful in understanding the PrF_3 spectra reported in this thesis, but no attempts have been made to calculate quantitative variations in the crystal field parameters based upon these chemical models because of the computational difficulties involved.

4.3 Far Infrared Stark Levels: Experimental Survey

In the fall of 1967, Professor R. P. Lowndes and the author surveyed the low temperature (5-8°K) transmittance between 20 cm^{-1} and 100 cm^{-1} of over 25 samples of the tysonite lanthanide fluorides approximately 5 mm thick and doped with approximately 1% of various trivalent lanthanide ions. The only trivalent lanthanide ions omitted from the survey were lutecium ($_{71}\text{Lu}$), holmium ($_{67}\text{Ho}$), and promethium ($_{61}\text{Pm}$). Lutecium has a closed shell of fourteen 4f electrons and consequently is like lanthanum in not permitting any 4f \rightarrow 4f electronic transitions. Holmium was temporarily unavailable. Promethium was unavailable because

it is radioactive and does not occur in nature. Not only is it very expensive but the decaying atoms tend to disrupt the host lattice thereby confusing the interpretation of its spectra. Only the omission of holmium could be considered detrimental to a full survey, but since the purpose of the survey was to identify profitable paths of thesis research and not to examine in detail all of the possible combinations of fourteen ions in four different tysonite lattices, the omission of two possibly interesting lanthanide ions out of fourteen did not diminish the value of the survey.

Strong lattice absorption extends from approximately 100 cm^{-1} to 500 cm^{-1} in the tysonite lanthanide fluorides (see preceding chapter for details). Consequently, electronic absorption lines in this region can not be studied unless they are very strong. Also, due to instrumental limitations, the spectra are very difficult to extend below 20 cm^{-1} without excessive noise which obscures possible weak absorption bands. Therefore, the survey was limited to the transparent region between 20 cm^{-1} and 100 cm^{-1} , excluding the strong (π -polarized) lattice absorption band near 30 cm^{-1} .

Unoriented samples of LaF_3 doped with approximately 1% of praseodymium (${}_{59}\text{Pr}^{3+}$, $4f^2$, ${}^3\text{H}_4$), neodymium (${}_{60}\text{Nd}^{3+}$, $4f^3$, ${}^4\text{I}_{9/2}$), and erbium (${}_{68}\text{Er}^{3+}$, $4f^{11}$, ${}^4\text{I}_{15/2}$) show rather strong and moderately sharp absorption bands below 100 cm^{-1} which are not evident

in the spectra of pure LaF_3 . The three lines are located at 56 cm^{-1} for Pr^{3+} , 45 cm^{-1} for Nd^{3+} , and 52 cm^{-1} for Er^{3+} .

Polarized far infrared spectra of these three ions in four different tysonite lattices are reported in a later section of this chapter. An electronic Stark level has been predicted⁽⁸⁹⁾ to lie 48 cm^{-1} above the ground state of the samarium ion (${}_{62}\text{Sm}^{3+}$, $4f^5$, ${}^6\text{H}_{5/2}$) but it could not be detected in the survey. Nevertheless, polarized spectra of Sm^{3+} in tysonite have been measured in hopes of detecting such a 48 cm^{-1} transition. Similarly, although no significant absorption bands could be detected in the survey, polarized spectra of the cerium ion (${}_{58}\text{Ce}^{3+}$, $4f^1$, ${}^2\text{F}_{5/2}$) have also been measured because Ce^{3+} completes the lightest series of lanthanide elements (from ${}_{57}\text{La}$ to ${}_{62}\text{Sm}$, omitting ${}_{61}\text{Pm}$ as noted above) and because a possible electronic level 71 cm^{-1} above the ground state has been predicted.⁽⁹⁰⁾

The rest of the lanthanide ions did not show conclusive evidence either for or against the existence of weak absorption lines below 100 cm^{-1} . Because it has no degeneracy, the lowest lying LSJ level of europium (${}_{63}\text{Eu}^{3+}$, $4f^6$, ${}^7\text{F}_0$) can not be split but only shifted by crystal field interactions. However, the first excited LSJ level (${}^7\text{F}_1$), only 350 cm^{-1} above the ground level, can be split into three Stark levels. The lowest LSJ level of gadolinium (${}_{64}\text{Gd}^{3+}$, $4f^7$, ${}^8\text{S}_{7/2}$) can not be split by first order interactions involving only the crystalline electric fields because it has zero orbital angular momentum. Actual

measurements in the microwave region ⁽⁹¹⁾ show that the $^8S_{7/2}$ level of gadolinium is split by typically 0.3 cm^{-1} by fourth order perturbation terms involving the electric fields to the first or second order and spin orbit interactions to the second or third order. ⁽³⁰⁾ Neither of these ions are expected to have any electronic levels 20 cm^{-1} to 100 cm^{-1} above the ground state and it is comforting that none were observed in this survey. On the other hand, terbium ($_{65}\text{Tb}^{3+}, 4f^8, ^7F_6$) and thulium ($_{69}\text{Tm}^{3+}, 4f^{12}, ^3H_6$) might have electronic levels between 60 cm^{-1} and 100 cm^{-1} because the samples doped with these two ions were opaque above 60 cm^{-1} . However, neither of them show any definite absorption lines, only a broad high frequency cut off which may be due to impurities or strains in an imperfect crystal rather than electronic lines. The other two lanthanide ions, dysprosium ($_{66}\text{Dy}^{3+}, 4f^9, ^6H_{15/2}$) and ytterbium ($_{70}\text{Yb}^{3+}, 4f^{13}, ^2F_{7/2}$), did not show any significant absorption not suggested by the pure LaF_3 samples. Moreover, the absence of transitions below 100 cm^{-1} is predicted for Yb^{3+} in LaF_3 . ⁽⁹²⁾ Possibly a further study of the trivalent ions of Tb, Dy, Ho, Tm, and Yb in tysonite may lead to the discovery of other far infrared electronic transitions, but the remainder of this report will deal primarily with those actually observed for trivalent ions of Ce, Pr, Nd, Sm, and Er in tysonite.

4.4 Paramagnetic Rotation

Reports of the paramagnetic susceptibilities and the Verdet constants as a function of temperature were among the earliest to reveal detailed information about the ground multiplet and site symmetry of the lanthanide ions in a tysonite lattice. The application of an external magnetic field causes degenerate electronic levels to split and the associated electronic transitions to become elliptically polarized: circularly polarized if the magnetic field is applied parallel to an optic axis. The resulting elliptically polarized optical dispersion causes a rotation of the electric field vector of linearly polarized light propagating parallel to the magnetic field. To the first order, the rotation of the plane of polarization is proportional to both the applied magnetic field and the propagation distance. The effect is called paramagnetic or Faraday rotation and the constant of proportionality is called the Verdet constant.

In many substances the Verdet constant as a function of temperature is proportional to the magnetic susceptibility with an additive constant.⁽⁹³⁾ The temperature dependence is interesting because the crystalline electric fields split the ground multiplet into several energy levels which may be populated or depopulated at experimentally accessible temperatures. For instance, the optical dispersion of CeF_3 at low temperatures is dominated by transitions of the single 4f electron of Ce^{3+} to excited 5d levels approximately $40,000 \text{ cm}^{-1}$ above the ${}^2F_{5/2}$ ground

multiplet. Consequently, the magnetic properties of the optical dispersion as expressed by the Verdet constants and the magnetic susceptibility of CeF_3 are both dominated by the magnetic characteristics of the lowest lying energy levels of the Ce^{3+} ion. As the temperature is changed the relative populations of the lowest lying levels change thereby similarly affecting the optical dispersion, the Verdet constants, and the magnetic susceptibilities at the same time. Because it consists largely of CeF_3 diluted with diamagnetic LaF_3 with only very small concentrations of other magnetic ions (principally Nd^{3+} and Pr^{3+}), the Verdet constants of naturally occurring tysonite are also proportional to the magnetic susceptibilities.

H. A. Kramers⁽⁹⁴⁾ based his calculation of the mean magnetic susceptibility of tysonite on the assumption that the electric fields at the Ce^{3+} ion have trigonal symmetry with the principal C_3 axis parallel to the optic axis. He showed that the mean or powder susceptibility of CeF_3 from 293°K down to 14°K could be fitted quite well with three Kramers doublet levels at 0, 163, and 652 cm^{-1} above the ground state.

Using the proportionality between the magnetic susceptibility and the Verdet constant, the magnetic susceptibility measurements can be extended down to 1.5°K . J. H. Van Vleck and M. H. Hebb⁽⁹³⁾ show that the mean susceptibility down to 1.5°K can be approximated fairly well by three doublet levels at 0, 139, and 765 cm^{-1} above the ground state, but that there are no

wavefunctions with trigonal symmetry which can correctly represent the magnetic susceptibility along the individual crystal axes. They extend their analysis to include sites with C_{2v} rhombic symmetry which have one axis parallel to the optic axis as proposed by Oftedal⁽³⁹⁾ for his $P6_3/mcm$ hexamolecular structure. Very good agreement is then found between the theoretical and experimental values of the magnetic susceptibilities both parallel and perpendicular to the optic axis for doublet levels at 0, 130, and 754 cm^{-1} above the ground state. They show that there is a rather strong deviation from the symmetry assumed by Kramers and suggest that even better agreement might be achieved by twisting each of the orthorhombic sites slightly as proposed for the $P6_3 22$ ⁽³⁴⁾ and $P\bar{3}c1$ ⁽⁴⁶⁻⁴⁹⁾ structures.

Even though their results are adequate to explain the temperature dependence of the principle values of the magnetic susceptibility, some discrepancies remain. Due to saturation effects, the theoretical magnetic susceptibility in the basal plane (perpendicular to the optic axis) of their proposed structure is not independent of the angle between the magnetic field and the crystal axes. However, it can be shown that the first term to depend upon the angle is proportional to the fourth power of the magnetic field. Therefore, the magnetic susceptibility in the basal plane should be independent of the angle between the magnetic field and the crystal axes for small

values of H . In fact, it is not. It is periodic with period $\pi/3$ even for very low field strengths⁽⁹³⁾ implying that a hexagonal structure is not adequate to explain the experimental results.

Nevertheless, the information derived from these early measurements are of value in several ways. First, they predict the approximate site symmetry and crystal field splitting of Ce^{3+} in tysonite. Second, they show that a hexagonal structure may not be adequate and indirectly support the recently proposed trigonal structure.⁽⁴⁶⁻⁴⁹⁾ Finally, the measurements of Jean Becquerel, W. J. de Haas, and J. van den Handel predict that the paramagnetic tysonite lattices may become antiferromagnetic at low temperatures.⁽⁹⁵⁾

4.5 EPR and NMR

More detailed information about the local crystal fields and the site symmetry of the lanthanide ions in tysonite can be derived from the EPR (electron paramagnetic resonance, also called ESR or electron spin resonance) tensor. Similar information about the fluorine ions can be derived from the NMR (nuclear magnetic resonance) tensor. Both of these effects are described by a second order symmetric tensor, called the g -tensor, defined at an atomic site. The equivalent tensors at other crystallographically equivalent atomic sites are related by the symmetry operations of the crystal's space group. Because

an external field is used, experimental measurements can yield up to five independent constants (the five components of the irreducible representation $Y_2^m(\theta, \varphi)$ of the full rotation group) for each atomic site. In information content, this compares quite favorably with the measurement of macroscopic vector properties such as electric and magnetic dipole transition moments which must be averaged over a complete unit cell and can yield no more than three independent constants (the three components of $Y_1^m(\theta, \varphi)$) for the entire crystal.

D. A. Jones, J. M. Baker, and D. F. D. Pope⁽⁹¹⁾ report that one of the principal components of the g-tensor of the $8S_{7/2}$ ground state of Gd^{3+} in LaF_3 is parallel to the optic axis. The other two components at a given site are mutually orthogonal to each other and to the optic axis. There are three magnetically distinguishable lanthanide sites, whose g-tensors are related by a rotation of 120° about the optic axis. They conclude that the results are consistent with the $P6_3/mcm$ (D_{6h}^3) structure proposed by Oftedal⁽³⁹⁾ and used by Van Vleck and Hebb⁽⁹³⁾ to explain the paramagnetic rotation of CeF_3 and naturally occurring tysonite. The six lanthanide sites in this structure are magnetically equivalent in pairs because of the glide plane operations perpendicular to the C_2 axes passing through each C_{2v} lanthanide site.

Later measurements by J. M. Baker and R. S. Rubins⁽⁹⁶⁾ show that none of the principal components of the EPR g-tensor

of $\text{Ce}^{3+}(4f^1, {}^2F_{5/2})$, $\text{Nd}^{3+}(4f^3, {}^4I_{9/2})$, $\text{Dy}^{3+}(4f^9, {}^6H_{15/2})$, $\text{Er}^{3+}(4f^{11}, {}^4I_{15/2})$, or $\text{Yb}^{3+}(4f^{13}, {}^2F_{7/2})$ in LaF_3 are parallel to the optic axis. However, one of the principal components, g_y , is always perpendicular to the optic axis and parallel to another crystal axis. The other two components are mutually perpendicular to each other and to g_y . The angle between the optic axis and g_z , the larger of these two components, varies from 10° for Yb^{3+} to 45° for Nd^{3+} and Er^{3+} . Six magnetically distinguishable lanthanide sites are observed. Their g-tensors are related by rotations of 120° about the optic axis and by either a reflection in a plane perpendicular to the optic axis or a rotation of 180° about the optic axis.

M. B. Schulz and C. D. Jeffries⁽⁹⁷⁾ report the EPR and spin-lattice relaxation in tysonite of all seven of the trivalent lanthanide ions which have an odd number of 4f electrons (all Stark levels are Kramers doublets) including $\text{Sm}^{3+}(4f^5, {}^6H_{5/2})$ and $\text{Gd}^{3+}(4f^7, {}^8S_{7/2})$. Due to the low lanthanide site symmetry in tysonite, no magnetic resonance is either expected or observed for those lanthanide ions, like $\text{Pr}^{3+}(4f^2, {}^3H_4)$, which have an even number of 4f electrons. In agreement with Baker and Rubins,⁽⁹⁶⁾ they observe six magnetically distinguishable lanthanide sites for everything except Gd^{3+} . The anomalous Gd^{3+} results may be associated with the very small (approximately 0.3 cm^{-1}) crystal field splitting of the ${}^8S_{7/2}$ ground state via second and third order spin-orbit coupling terms involving the

${}^6P_{7/2}$ and ${}^6D_{7/2}$ excited LSJ levels of the $4f^7$ configuration. (30)

Schulz and Jeffries also comment on the fact that the reported g-tensors are not consistent with either the hexagonal $P6_3/mcm$ or the trigonal $\bar{P}3cl$ structures because both of them allow only three magnetically distinguishable lanthanide sites. They further suggest that the inconsistency may be resolved by a low temperature phase transition or by twinning of the trigonal $\bar{P}3cl$ structure. (97)

Studies of the motional narrowing of the nuclear magnetic resonance of fluorine nuclei (${}^{19}_9F$) in tysonite reveal that there is considerable ionic diffusion even at room temperatures. (98-101) From slightly below room temperatures up to about $500^\circ K$ the ratio of fast moving to slow moving fluorines is reported by most authors (100-103) to be approximately 2:1, although Russian experimenters (104-105) consistently report the inverse. Above $500^\circ K$ all of the fluorine ions appear to be in rapid motion. (100-105) Recent low temperature ($88^\circ K$) NMR measurements by Kenneth Lee (103,106) show that there are four fluorine sites in tysonite which are magnetically distinguishable along the c-axis of the crystal. The concentration ratios for these four fluorine sites, 3:3:2:1, were initially interpreted (106) as supporting the $P6_3cm$ (C_{6v}^3) structure proposed from neutron diffraction measurements. (50) However, additional NMR measurements at higher magnetic field strengths (103) reveal a field independent splitting of the two magnetically distinguishable fluorines with the

highest concentrations. This field independent splitting implies that the fluorine ions must be crystallographically equivalent and that there are only three crystallographically inequivalent fluorine sites in tysonite with the concentration ratios of 6:2:1. These ratios are in agreement with the predictions of the hexagonal $P6_3/mcm$ (D_{6h}^3) or trigonal $P\bar{3}c1$ (D_{3d}^4) structures but not with the hexagonal $P6_3cm$ (C_{6v}^3) structure. (103) Moreover, above room temperature, the nuclear magnetic resonance lines coalesce and the g-fluorines of the $P\bar{3}c1$ structure have been identified as moving faster than those at the a or d fluorine sites. (103)

The nuclear quadrupole resonance (NQR) of the lanthanum ($^{139}_{57}\text{La}$) nucleus has also been studied by K. Lee and A. Sher (107) and by L. O. Andersson and W. G. Proctor. (107-108) They report six magnetically distinguishable lanthanide sites which is consistent with the $P6_3cm$ structure but not with either the $P6_3/mcm$ or the $P\bar{3}c1$ structures. However, K. Lee (103) has suggested that all of the results of Andersson and Proctor are consistent with a twinned $P\bar{3}c1$ structure.

4.6 Infrared Spectra: A Literature Survey

Absorbance and fluorescence spectra of all of the lanthanide ions have been studied in one or more solid state hosts. (See for example references 28, 30, or 31) However, such spectra have not yet been reported for all of the lanthanide ions in the

four lightest tysonite lanthanide fluorides, even though the materials are now commercially available.⁽⁵⁾ This brief survey of the published spectra of $Ce^{3+}(4f^1)$, $Pr^{3+}(4f^2)$, $Nd^{3+}(4f^3)$, $Sm^{3+}(4f^5)$, $Er^{3+}(4f^{11})$, and $Yb^{3+}(4f^{13})$ ions in one or more tysonite lanthanide fluoride host lattices is presented as an introduction to the new polarized far infrared spectra reported in the next section.

The $4f \rightarrow 4f$ electronic spectra of Ce^{3+} and Yb^{3+} are the simplest of the lanthanide series because there is only one term (2F) and two LSJ levels ($^2F_{5/2}$ and $^2F_{7/2}$). The crystalline electric fields of the tysonite lattice split the $^2F_{5/2}$ level into three Stark levels and the $^2F_{7/2}$ level into four Stark levels, each Stark level being a Kramers doublet. The infrared absorption spectra of Ce^{3+} in both LaF_3 and CeF_3 have been reported by R. A. Buchanan, H. E. Rast, and H. H. Caspers.⁽⁹⁰⁾ The infrared fluorescence spectra of Yb^{3+} in LaF_3 have been reported by H. E. Rast, H. H. Caspers, and S. A. Miller.⁽⁹²⁾ In addition, H. E. Rast and H. H. Caspers have also observed the fluorescence and absorbance spectra of Sm^{3+} in LaF_3 and published them in an internal report of the Naval Ordnance Laboratory Corona.⁽⁸⁹⁾

Many spectra have been reported for the Pr^{3+} ion in both LaF_3 and PrF_3 . Since the $4f$ electronic wavefunctions have integral spin, all of the electronic degeneracies are lifted in tysonite and each LSJ level splits into $2J + 1$ Stark levels.

Edward V. Sayre and Simon Freed⁽¹⁰⁹⁾ report that the selection rules governing the absorption spectra of pure PrF_3 films are consistent with the C_{2v} lanthanide site symmetry of the $P6_3/mcm$ structure at liquid nitrogen temperatures but weak transitions forbidden by the C_{2v} site symmetry appear at liquid helium temperatures. They suggest that the Pr^{3+} ions do not lie on the vertical mirror planes of the $P6_3/mcm$ structure. On the other hand, the spectra of Pr^{3+} in LaF_3 published by Eugene Y. Wong, Oscar M. Stafsudd, and David R. Johnston,⁽⁷⁴⁾ W. M. Yen, W. C. Scott, and A. L. Schawlow,⁽¹¹⁰⁾ and H. H. Caspers, H. E. Rast, and R. A. Buchanan⁽¹¹¹⁾ are completely consistent with the C_{2v} lanthanide site symmetry. Unpolarized far infrared absorption spectra of the electronic transition from the ground state to the first excited state of the 3H_4 multiplet of Pr^{3+} in LaF_3 and PrF_3 powders have been reported by R. A. Buchanan and M. A. Butler.⁽¹¹²⁾ The polarized far infrared spectra of PrF_3 published by Armand Hadni and Pierre Strimer⁽¹¹³⁾ are in essential agreement with those observed by the author and show absorption transitions from the ground state to both the first and second excited states of the 3H_4 multiplet of Pr^{3+} in PrF_3 . Unfortunately, several lattice phonon transitions and possibly a polyethylene absorption band are also visible in their spectra and Hadni and Strimer grossly misinterpret the PrF_3 spectra below 120 cm^{-1} as representing the entire 3H_4 multiplet of Pr^{3+} in PrF_3 which actually extends beyond 500 cm^{-1} . A more accurate interpretation of the spectra is presented in the next section.

The unpolarized absorption spectrum of NdF_3 including some Zeeman effects has been reported by Y. K. Chow.⁽¹¹⁴⁾ Subsequent publications by Eugene Y. Wong, Oscar M. Stafsudd, and David R. Johnston,⁽¹¹⁵⁾ H. H. Caspers, H. E. Rast, and R. A. Buchanan,⁽¹¹⁶⁾ C. K. Asawa and M. Robinson,⁽¹¹⁷⁾ and S. A. Johnson, H. G. Freie, A. L. Schawlow, and W. M. Yen⁽¹¹⁸⁾ have reported various temperature dependent properties of the absorbance and fluorescence spectra of Nd^{3+} in LaF_3 . Erbium does not form a tysonite trifluoride lattice at room temperature, consequently only the absorbance and fluorescence spectra of Er^{3+} in LaF_3 have been reported by William F. Krupke and John B. Gruber.^(2,119)

The published Stark levels of the two or three lowest energy LSJ multiplets of cerium, praseodymium, neodymium, samarium, erbium, and ytterbium are summarized in Table 4.2. Note that one level each of Nd, Sm, and Er and two levels of Pr should be observable in the far infrared spectra recorded below 100 cm^{-1} . Only the 48 cm^{-1} transition of Sm^{3+} was missed in the survey spectra and the polarized spectra reported in the next section. Either this level does not actually exist or the transition is too weak to be observed in the concentration studied. Details of the polarized far infrared spectra of Pr^{3+} , Nd^{3+} , and Er^{3+} in LaF_3 , CeF_3 , PrF_3 , and NdF_3 are reported in the next section. All of the energy levels of the higher LSJ multiplets should be observable since they lie well above the lattice bands of tysonite.

TABLE 4.2

Predicted low energy Stark levels in tysonite

Substance	References	$(2S+1)_{L_J}$	Energy Levels (cm^{-1})
$\text{LaF}_3:\text{Ce}^{3+}$	90	$2F_{5/2}$	0,150,???
		$2F_{7/2}$	2160,2240,2635,2845
$\text{CeF}_3:\text{Ce}^{3+}$	90	$2F_{5/2}$	0,148,???
		$2F_{7/2}$	2158,2238,2638,2848
$\text{LaF}_3:\text{Nd}^{3+}$	116,	$4I_{9/2}$	0,45,136,296,500
	117,	$4I_{11/2}$	1978,2037,2068,2091,2187,2223
	118	$4I_{13/2}$	3919,3979,4039,4078,4120,4213,4278
$\text{NdF}_3:\text{Nd}^{3+}$	114	$4I_{9/2}$	0,46,148,...?
$\text{LaF}_3:\text{Sm}^{3+}$	89	$6H_{5/2}$	0,48,115
		$6H_{7/2}$	1000,1044,1185,1280
		$6H_{9/2}$	2210,2245,2342,2409,2473
$\text{LaF}_3:\text{Er}^{3+}$	2, 119	$4I_{15/2}$	0,52,122,200,220,314,401,444
		$4I_{13/2}$	6603,6631,6672,6702,6735,6744,6827
		$4I_{11/2}$	10264,10304,10315,10335,10349,10401
$\text{LaF}_3:\text{Yb}^{3+}$	92	$2F_{7/2}$	0,185,401,(870)?
		$2F_{5/2}$	10260,10430,10660
$\text{LaF}_3:\text{Pr}^{3+}$	110,	$3H_4$	0,58,76,137,196,203,296,330,508
	111,	$3H_5$	2179,2234,2272,2299,2304,2354,2412, 2431,2457,2469,2567
	112	$3H_6$	4219,4223,4266,4300,4385,4440,4508, 4527,4552,4579,4591,4671,4776
$\text{PrF}_3:\text{Pr}^{3+}$	109, 112	$3H_5$	0,66,88,...?

4.7 Polarized Far Infrared Spectra

All of the measurements reported in this section were made on the modified PS-520 Fourier Spectrophotometer described in the second chapter using the TI detector and the 0.5 mil beam splitter. The samples of LaF_3 , CeF_3 , PrF_3 , and NdF_3 were purchased from Optovac, Inc. ⁽⁵⁾ They were 10 millimeters in diameter and were cut and hand polished to be 0.7 mm to 1.7 mm thick with the optic axis within five arc degrees of being parallel to the face of the crystal. The samples were held in a high purity copper block sample holder attached to the tail of a liquid helium reservoir. The temperature of the sample holder farthest from the liquid helium reservoir was measured to lie between 5°K and 8°K and was stable throughout a given experimental run to better than 0.1°K .

The low temperature absorption coefficient of pure LaF_3 and pure CeF_3 in both polarizations is reported in the preceding chapter and displayed in Figures 2.6 and 2.7. At first, the sharp absorption peak near 108 cm^{-1} in the π -polarization was thought to be an impurity vibrational or electronic line. However, as discussed in Chapters II and III, it is a spurious absorption not intrinsically present in the π -polarization. It is associated with the lowest frequency, σ -polarized LO (longitudinal optic) mode of the tysonite lattice.

The ripple between 115 and 120 cm^{-1} in the π -polarized absorption coefficient of CeF_3 is also thought to be spurious.

Because the absolute value of the transmittance is so small ($\leq 5\%$), only a very slight misalignment ($\leq 5^\circ$) of the sample with respect to the polarizer can lead to significant cross talk (approximately a 1% change in the transmittance) between the experimentally measured ordinary (σ) and extraordinary (π) transmittance. There is a minimum in the σ -polarized absorption coefficient at 118 cm^{-1} associated with a peak in the σ -polarized transmittance where $k \approx 0$ as $n \approx 1$. Rather than being a peak in the π -polarized absorption coefficient due to an actual π -polarized absorption band at 115 cm^{-1} , it is more likely a dip at 118 cm^{-1} in the experimentally calculated absorption coefficient due to cross talk from the σ -polarized transmission peak at the Christiansen⁽²⁴⁻²⁶⁾ frequency.

No characteristic absorption peaks, not already accounted for in Chapter III, are observed in either polarization of CeF_3 below 115 cm^{-1} . Thus, the existence of an electronic energy level only 71 cm^{-1} above the ground state of Ce^{3+} in CeF_3 is very unlikely,⁽⁹⁰⁾ unless the electric dipole transition moment between these two energy levels is extremely small. Based upon current data, the first excited Stark level of Ce^{3+} in CeF_3 is almost certainly at or near 150 cm^{-1} above the ground level as predicted by most of the early research.^(90,93,95-97)

Unfortunately, a one millimeter thick sample of CeF_3 at 7°K is opaque above 120 cm^{-1} , which precludes the direct observation in transmission of a 150 cm^{-1} , infrared active transition

between the two lowest lying Stark levels of Ce^{3+} . Moreover, this probable transition is not strong enough to be clearly evident in the reflectance spectra of CeF_3 reported in Chapter III. More accurate (and tedious) measurement of the reflectance or transmittance of CeF_3 may reveal a 150 cm^{-1} electronic transition in pure CeF_3 , but such a search for it seems hopeless in samples of tysonite doped with only 1% Ce^{3+} . Nevertheless, a search for this transition in low temperature Raman spectra may be quite fruitful.

The Nd^{3+} spectra, on the other hand, show a very clear electronic transition near 45 cm^{-1} in all four host lattices. There is no doubt that the transition is unpolarized in 1% concentrations as shown in Figure 4.1. In pure NdF_3 , however, the TO (transverse optic) and LO (longitudinal optic) frequencies of the electronic transition are split by the electric dipole moment of the transition. Due to macroscopic polarization effects, the TO and LO frequencies can differ between the two polarizations although they are due to the same intrinsic "free resonance" in the anisotropic, microscopic, ionic polarizability.

The frequency, peak absorption coefficient, and half width of the 45 cm^{-1} Nd^{3+} transition in the four lightest tysonite lanthanide fluorides are summarized in Table 4.3. In LaF_3 and CeF_3 the electronic transition has almost the same peak absorption coefficient in either the π - or σ -polarizations. In PrF_3

Figure 4-1: Nd^{3+} electronic transition in LaF_3 , CeF_3 , PrF_3 ,
and NdF_3

1% Nd³⁺ IN TYSONITE LANTHANIDE FLUORIDES

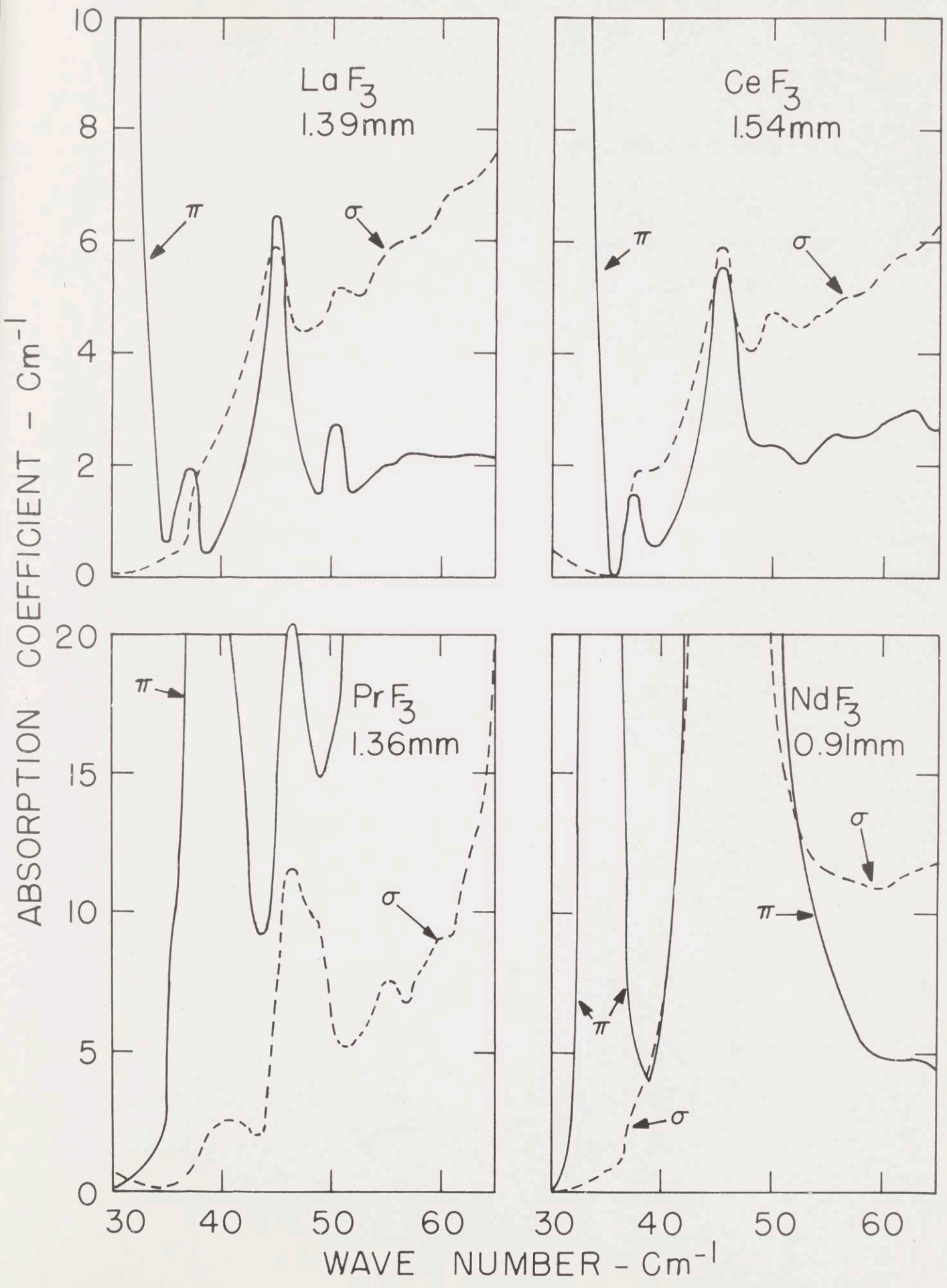


TABLE 4.3

Nd³⁺ electronic transition in LaF₃, CeF₃, PrF₃, and NdF₃

Host lattice	LaF ₃	CeF ₃	PrF ₃	NdF ₃	
Thickness mm	1.39	1.54	1.36	0.91	
Wave number cm ⁻¹	45.0 ± 0.5	45.5 ± 0.5	46.5 ± 0.5	46 ± 2	
Half width cm ⁻¹	π	3.5	4.0	4→7	<8
	σ	5.0	4→5	3→6	<8
Peak absorption cm ⁻¹	π	6.4	5.6	20.4	10 ² →10 ³
	σ	5.9	5.9	11.6	10 ² →10 ³

and NdF_3 , however, the transition is approximately 75% stronger in the π -polarization. Moreover, although the Nd^{3+} concentration is reportedly the same in both the LaF_3 and PrF_3 samples, the transition seems to be enhanced in the PrF_3 lattice. The enhancement may be due to an increase in the magnitude of the odd spherical harmonics in the crystalline electric field or it may be due to coupling with the highly polarizable Pr^{3+} ions occupying most of the lanthanide sites.

In NdF_3 , the Nd^{3+} transition is strong enough to be detectable in the reflectance spectra reported in Chapter III. Using the proportionality between the square of the experimentally measured width of a transition at a given absorption coefficient and the strength of the transition, ⁽⁵⁶⁾ the Nd^{3+} transition in NdF_3 is only about half as strong in the π -polarization as the σ -polarized lattice mode at 100 cm^{-1} in LaF_3 . Nevertheless, it is as strong as or slightly stronger than the π -polarized lattice mode at 30 cm^{-1} in LaF_3 . Unfortunately, the intensity of the far infrared source drops off very rapidly at lower frequencies and the lower signal to noise ratio makes the 45 cm^{-1} Nd^{3+} transition barely detectable and the 30 cm^{-1} lattice mode undetectable with the instrumentation used. Further reflectance measurements with an improved low temperature and long wavelength detector should reveal more information about the 45 cm^{-1} electronic transition in NdF_3 and could reveal more clearly the lowest frequency π -polarized lattice mode of the tysonite lanthanide fluorides.

No characteristic absorption peaks, not already accounted for in Chapter III, are observed in any of the spectra of the two different samples of LaF_3 doped with 1% Sm^{3+} used in this study. Both of the samples are a very pale green and appear to have no optical defects. The first one is the unoriented sample approximately 5 mm thick used in the preliminary survey. The second one is oriented with the optic axis parallel to the face of the crystal and has been cut and hand polished into two disks approximately 1 mm and 3 mm thick. None of the samarium doped samples are quite as transparent below 100 cm^{-1} as pure LaF_3 . Possibly this broad general absorption is associated with the mass defect between the lanthanum and the samarium ions (approximately 8%). However, other than a slightly higher average absorption coefficient, no sharp or even distinct absorption bands are observed, not even in the neighborhood of the predicted 48 cm^{-1} transition.⁽⁸⁹⁾ The sensitivity of the measurements and the thickness of the samples suggests that if the transition exists the peak absorption coefficient must be less than 0.5 cm^{-1} . Thus, the intrinsic electric dipole moment of the Sm^{3+} transition must be less than one-tenth that of either Nd^{3+} or Er^{3+} , or electron-phonon coupling with the phonon mode detected at 50 cm^{-1} in LaF_3 has broadened the electronic transition so much that it is not clearly visible. In either case, it may yet be possible to observe this transition, if it does indeed

exist, in higher concentrations of Sm^{3+} in LaF_3 or in one of the other tysonite host lattices.

The far infrared spectra of Er^{3+} in the tysonite lanthanide fluorides are quite similar to those of Nd^{3+} . However, as shown in Figure 4.2, the Er^{3+} transition is approximately 50% stronger in the σ -polarization than in the π -polarization. Thus, although it is clearly unpolarized, the Er^{3+} transition possesses a characteristic anisotropy. With respect to $\text{LaF}_3:\text{Er}^{3+}$, there is a slight enhancement of the strength of the Er^{3+} transition in both CeF_3 and NdF_3 , but there is not a significant enhancement of the σ -polarized component in PrF_3 . The $56.7 \text{ cm}^{-1} \text{ Er}^{3+}$ transition could not be observed in the π -polarization of PrF_3 because it was obscured by the strong, π -polarized, 66 cm^{-1} electronic transition of the Pr^{3+} ions in PrF_3 . The frequency, peak absorption coefficient, and half width of the $52 \text{ cm}^{-1} \text{ Er}^{3+}$ transition in the four lightest tysonite lanthanide fluorides are summarized in Table 4.4. Note that the frequency of the erbium electronic transition changes much more rapidly as a function of the host lattice than does that of the neodymium electronic transition.

The far infrared spectra of the $\text{Pr}^{3+} ({}^3\text{H}_4)$ ion in the tysonite lanthanide fluorides are unique in several ways. It is the only lanthanide ion studied in detail in this report which has an integral spin ($J=4$) wavefunction: therefore all of the electronic degeneracies are lifted (no Kramers degeneracy) and

Figure 4-2: Er^{3+} electronic transition in LaF_3 , CeF_3 , PrF_3 ,
and NdF_3

1% Er³⁺ IN TYSONITE LANTHANIDE FLUORIDES

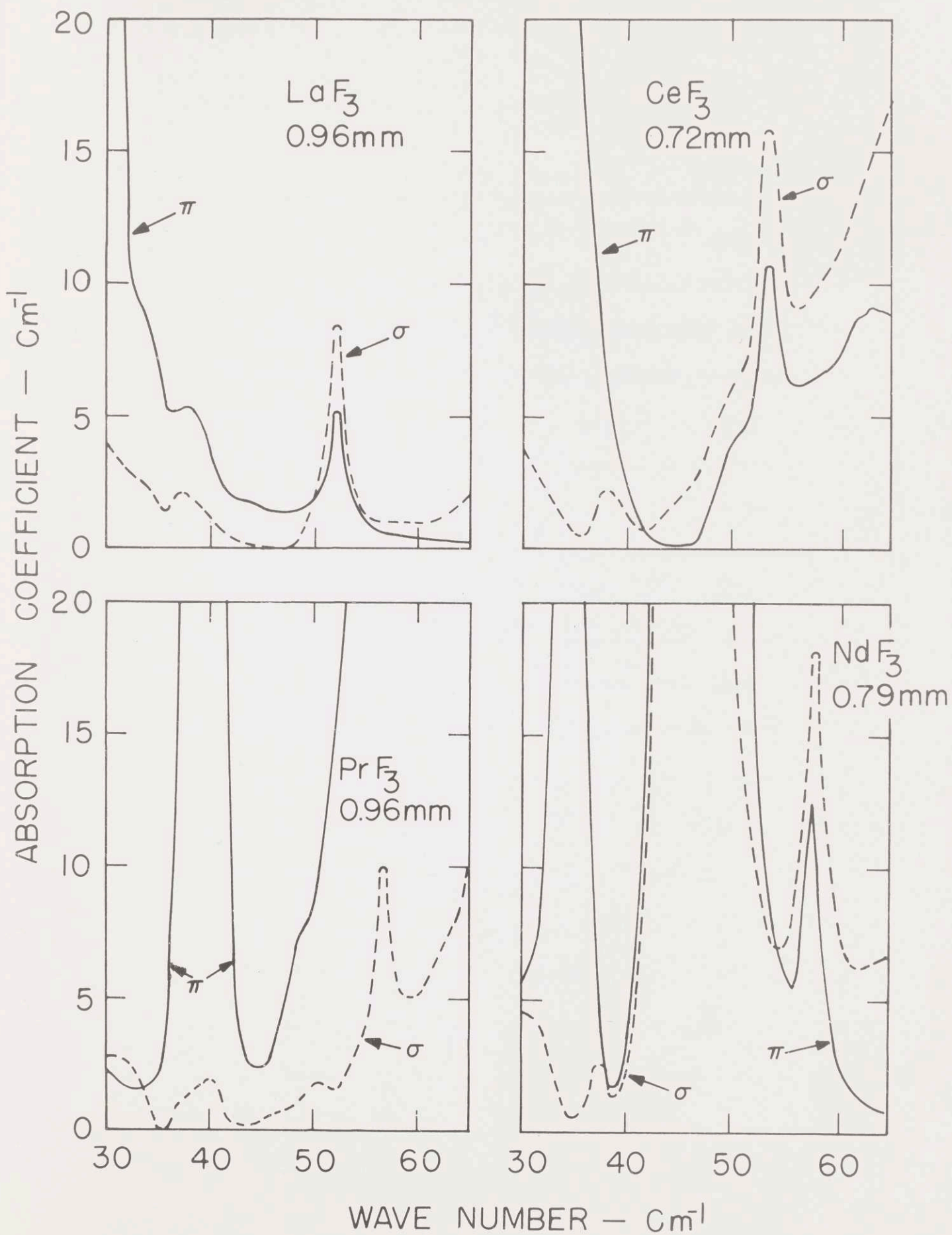


TABLE 4.4

Er³⁺ electronic transition in LaF₃, CeF₃, PrF₃, and NdF₃

Host lattice	LaF ₃	CeF ₃	PrF ₃	NdF ₃	
Thickness mm	0.96	0.72	0.96	0.79	
Wave number cm ⁻¹	52.0 ± 0.5	53.5 ± 0.5	56.7 ± 0.5	57.7 ± 0.5	
Half width cm ⁻¹	π	<1.5	~2.5	<1.5	<2.0
	σ	<1.5	~3.0	<1.5	<2.0
Peak absorption cm ⁻¹	π	5.2	10.8	~40	12.4
	σ	8.4	15.9	10.0	18.2

the ion is not paramagnetic in small magnetic fields. Two different electronic transitions are observed below 100 cm^{-1} . Both electronic transitions appear to be very strongly polarized either parallel or perpendicular to the optic axis. Both electronic transitions are strong enough to be clearly visible and easily measurable in the reflectance spectra of pure PrF_3 .

The low temperature spectra from 50 cm^{-1} to 85 cm^{-1} of Pr^{3+} in the four lightest tysonite lanthanide fluorides are shown in Figure 4.3. Note that both electronic absorption bands are visible in the LaF_3 host spectra. The higher frequency transition is obscured by the lowest frequency σ -polarized lattice band in both CeF_3 and NdF_3 . Nevertheless, the upper bound on the strength of the higher frequency Pr^{3+} transition in these two host lattices is consistent with the strength measured in LaF_3 , and one would expect the transition to be easily visible in 0.25 mm thick samples of CeF_3 and NdF_3 doped with 2-5% Pr^{3+} . Two additional oriented samples of CeF_3 and NdF_3 with higher concentrations of Pr^{3+} were not purchased for this study because of the time required to grow the crystals. The frequency, peak absorption coefficient, and half width of the Pr^{3+} electronic transitions in the four lightest tysonite lanthanide fluorides are summarized in Table 4.5. Note that the frequencies of the praseodymium transitions change rather dramatically as a function of the host lattice.

Figure 4.3: Pr^{3+} electronic transitions in LaF_3 , CeF_3 , PrF_3 , and NdF_3 .

1% Pr³⁺ IN TYSONITE LANTHANIDE FLUORIDES

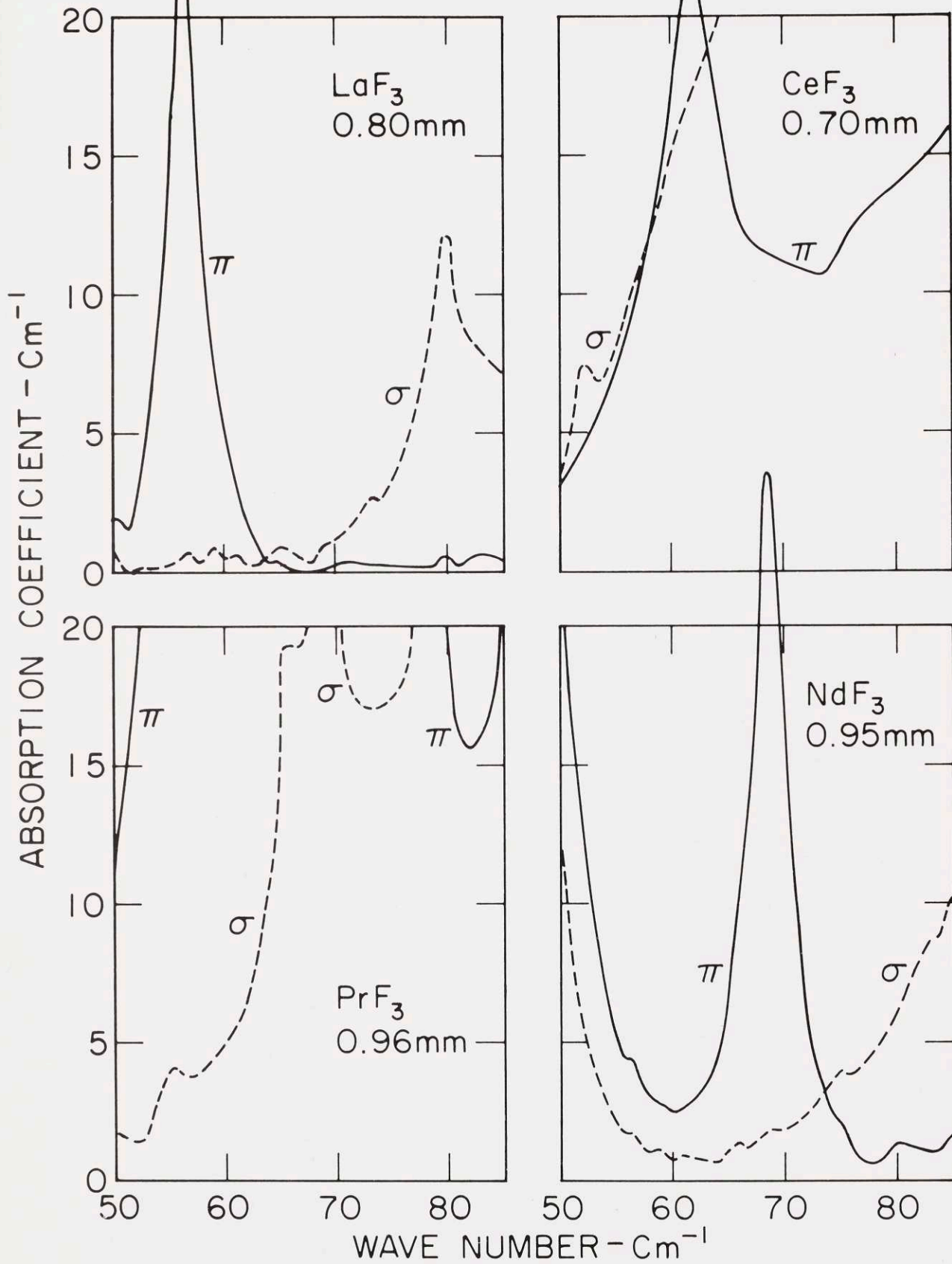


TABLE 4.5

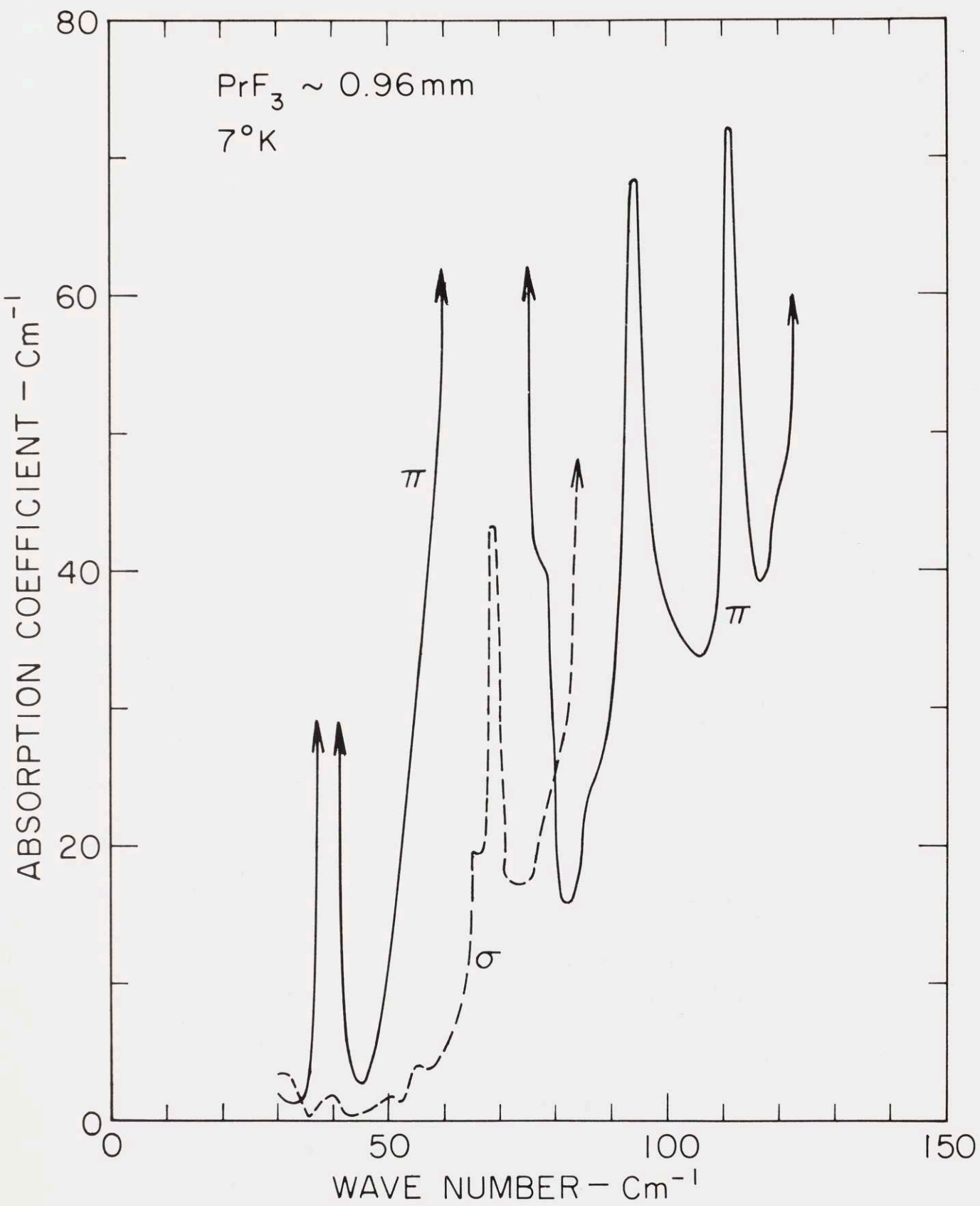
Pr³⁺ electronic transitions in LaF₃, CeF₃, PrF₃, and NdF₃

Host lattice	LaF ₃	CeF ₃		PrF ₃	NdF ₃
Thickness mm	0.80	0.70		0.96	0.95
Wave number cm ⁻¹	56.5 ± 0.5	62.0 ± 0.5	π σ	66 → 69 69.0 ± 0.5	68.5 ± 0.5
Half width cm ⁻¹	3.0	9.0	π σ	~3.0 3.5	4.0
Peak absorption cm ⁻¹	23.0	21.4	π σ	~10 ⁴ 43.2	25.5
Wave number cm ⁻¹	80.0 ± 0.5	?	π σ	94.0 ± 0.5 92 → 94	?
Half width cm ⁻¹	4.5	?	π σ	5.0 ~2.0	?
Peak absorption cm ⁻¹	12.2	?	π σ	68.2 ~10 ⁴	?

A wider range display of the low temperature absorption coefficients of PrF_3 is shown in Figure 4.4. Note that the 66 cm^{-1} transition in the π -polarization and the 92 cm^{-1} transition in the σ -polarization are so strong that the spectra are opaque over a rather wide frequency band. These are the same two bands observed in the low temperature reststrahlen spectra of PrF_3 . Moreover, note that in the orthogonal polarizations the crystal is almost but not quite transparent at these same frequencies. The weak, flat shoulders near 66 and 92 cm^{-1} were also observed by Armand Hadni⁽¹¹³⁾ but are most likely due to a slight cross talk from the orthogonal polarization due to a misalignment of the polarizer with respect to the crystal. However, the rather sharp peaks near 69 cm^{-1} and 94 cm^{-1} can not be explained in terms of cross talk from the broad flat bands in the orthogonal polarizations.

The 94 cm^{-1} peak is similar to the 111 cm^{-1} peak in the π -polarization. Just as the 111 cm^{-1} peak has been definitely associated with the lowest frequency LO mode of the tysonite lattice in the σ -polarization as discussed in detail earlier, the 94 cm^{-1} peak can be associated with the LO frequency of the Pr^{3+} electronic transition whose TO frequency is at 92 cm^{-1} in the σ -polarization. Both of these spurious absorptions occur because the extraordinary dielectric response function is being observed experimentally and the optic axis makes a slight angle ($\sim 5^\circ$) with respect to the polished face of the crystal. More

Figure 4.4: Low temperature absorption coefficient spectra of PrF_3



careful orientation of the tysonite lanthanide fluoride samples may be advisable in the future in order to reveal additional detail in the π -polarization above 90 cm^{-1} .

The peak near 69 cm^{-1} in the σ -polarization, on the other hand, can not be attributed to spurious absorption associated with the LO frequency of the Pr^{3+} electronic transition whose TO frequency is at 66 cm^{-1} in the π -polarization. Whereas the experimentally measured value of the extraordinary (π -polarized) dielectric response function depends upon both $\epsilon_x(\omega)$ and $\epsilon_z(\omega)$ via the angle, φ , between the optic axis and the face of the crystal, the experimentally measured value of the ordinary (σ -polarized) dielectric response function depends only upon $\epsilon_x(\omega)$ and is independent of φ . The only way features of $\epsilon_z(\omega)$ can occur in the experimentally measured σ -polarized spectra is through the additive term involving the orientation of the polarizer with respect to the optic axis. However, as proved earlier, such effects change the transmittance by less than 1% (for misalignments of less than five degrees) and must have the same shape a features observed in the π -polarized spectra. Thus, whereas a broad flat topped band in the σ -polarized spectra extending from approximately $65\text{-}70 \text{ cm}^{-1}$ (note the shoulders actually observed) can be explained away by experimental misalignments, the sharp peak near 69 cm^{-1} must be due to an intrinsic, σ -polarized absorption process.

Moreover, since this absorption appears only in the PrF_3 spectra, it can be taken as evidence for the depolarization of the lower frequency Pr^{3+} electronic transition. The fact that the transition is over a hundred times as strong in the π -polarization causes the observed TO and LO frequencies to split measurably from each other and from the apparent "free" resonance in the anisotropic, microscopic, ionic polarizability of the Pr^{3+} ions near 69 cm^{-1} in the σ -polarization. Nevertheless, the absorption in both polarizations is due to the same single-ion transition which is unpolarized in the group theoretical sense.

4.8 Far Infrared Zeeman Splitting

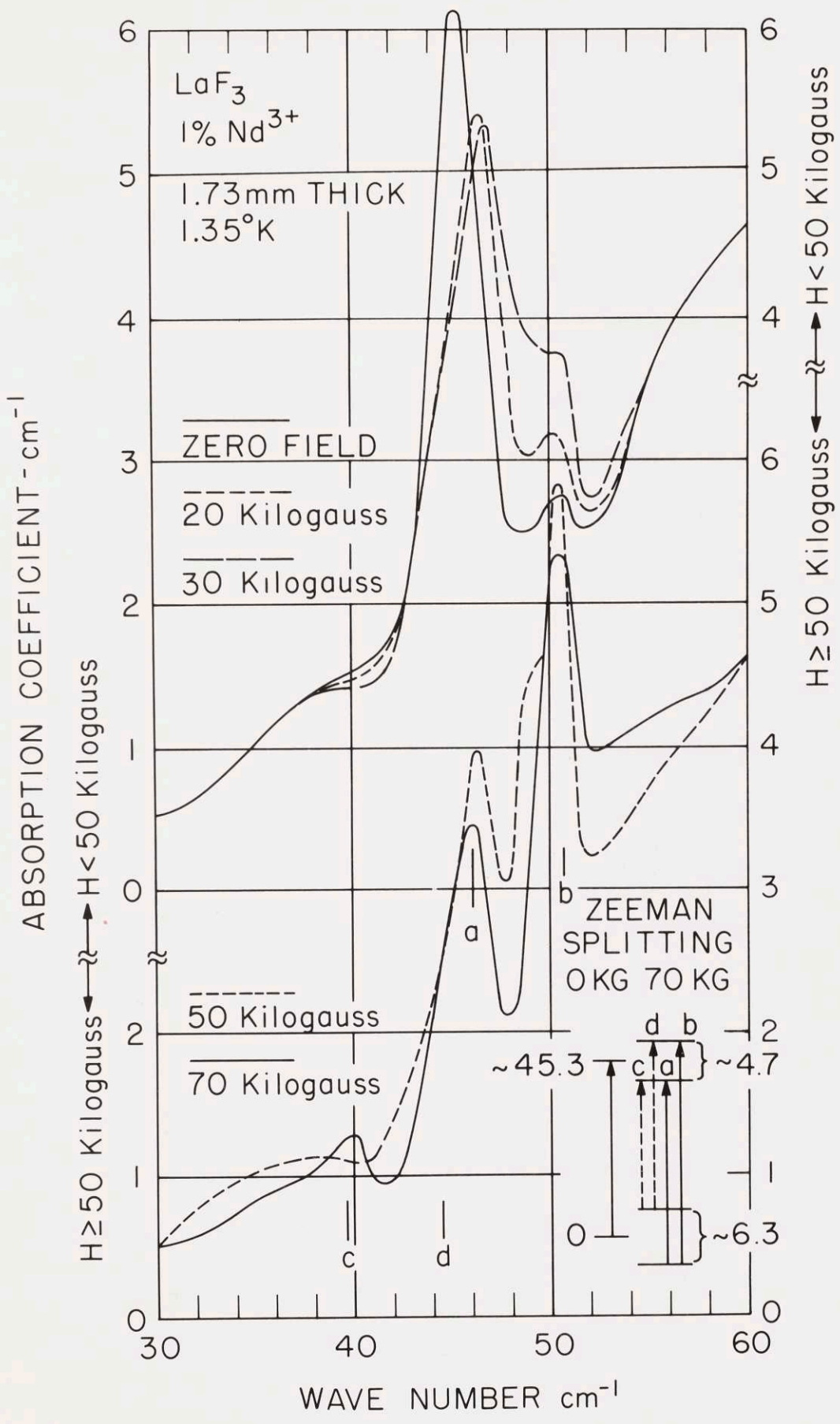
All of the spectra reported in this section were taken at the Francis Bitter National Magnet Laboratory using a Grubb-Parsons far infrared Michelson interferometer. The transmission samples were 0.25" in diameter and 0.04" thick. The reflection samples were 0.375" in diameter and 0.1" thick with a one degree wedge angle between the two faces. The samples and the detector were immersed in pumped liquid helium at temperatures between 1.0 and 1.7°K. Magnetic fields up to 70 kilogauss could be achieved conveniently with a single DC generator. Two of the four generators at the National Magnet Laboratory were used for fields up to 150 kilogauss.

An unoriented single crystal of LaF_3 doped with one mole percent of Nd^{3+} was used to generate the spectra shown in

Figure 4.5. The direction of propagation of the infrared radiation is parallel to the applied magnetic field and approximately perpendicular to the crystal's optic axis ($80^\circ < \theta < 85^\circ$). The operating temperature is $1.35 \pm 0.05^\circ\text{K}$.

Each of the five Stark levels of the $^4I_{9/2}$ ground multiplet of Nd^{3+} in the tysonite fluorides is a Kramers doublet which may be split into two Zeeman levels by an external magnetic field. In zero magnetic field, the unpolarized absorption coefficient in Figure 4.5 shows both a 45 cm^{-1} electronic transition of Nd^{3+} and a 51 cm^{-1} vibrational transition of the LaF_3 lattice. As the magnetic field is increased to 20 and 30 kilogauss, the Nd^{3+} transition appears to broaden from 3.5 cm^{-1} to 4.5 and 5.5 cm^{-1} and to increase in frequency by 1.1 and 1.5 cm^{-1} thereby confirming its electronic nature. On the other hand, although there is an increase in the peak absorption coefficient of the 51 cm^{-1} transition, its frequency does not change thereby confirming its vibrational nature. Below approximately thirty kilogauss, no Zeeman splitting can be resolved due to the instrumental slit width of approximately 2 cm^{-1} and a transition line width of approximately 3.5 cm^{-1} . At 50 kilogauss, however, the Nd^{3+} transition is clearly Zeeman split with a lower frequency component, a, at 46 cm^{-1} and a higher frequency one, b, at 49.5 cm^{-1} . The 51 cm^{-1} transition appears as a very strong resonance at 50.5 cm^{-1} at 50 kilogauss. At 70 kilogauss, the

Figure 4.5: Zeeman spectra of Nd^{3+} electronic transition in LaF_3



Nd^{3+} transitions split further and the higher frequency b-component moves to approximately 51 cm^{-1} , slightly above the weakening lattice resonance at 50.5 cm^{-1} . The behavior of the strength of the b-transition suggests vibronic coupling with the 50.5 cm^{-1} lattice vibration.

Electronic transitions c and d between the upper Zeeman level of the ground doublet and the Zeeman levels of the excited Kramers doublet are not observed because of thermal depopulation. Moreover, although the g-tensor is anisotropic and each of the six lanthanide sites can have a slightly different Zeeman splitting, only two levels could be clearly resolved because the instrumental slit width and the transition line width are too wide. Consequently, only an average spectroscopic g value for these six lanthanide sites could be determined in this experiment. The mean g value for the excited Stark level is 1.4 ± 0.1 . For the ground Stark level it is 2.1 ± 0.2 which is well within the limits of the reported g-tensor of the ground level based upon the electron spin resonance of Nd^{3+} in LaF_3 .⁽⁹⁶⁾

The LaF_3 sample doped with one mole percent of Er^{3+} is also an unoriented single crystal. The angle between the applied magnetic field and the optic axis is approximately 45 degrees. The operating temperature is $1.33 \pm 0.03^\circ \text{K}$ and the instrumental slit width is slightly less than 2 cm^{-1} .

Each of the eight Stark levels of the $^4\text{I}_{15/2}$ ground multiplet

of Er^{3+} in the tysonite fluorides is a Kramers doublet. In zero magnetic field, the spectrum of Er^{3+} in LaF_3 is quite similar to that of Nd^{3+} in LaF_3 except that the electronic transition is at 52.2 cm^{-1} rather than 45 cm^{-1} and the spectrum is much more cluttered with interference or channel spectra lines. At only 20 kilogauss, however, the Er^{3+} absorption spectrum is strikingly different. The single absorption line at 52 cm^{-1} less than 2 cm^{-1} wide has been replaced by a broad band extending from 52.5 to 58.5 cm^{-1} whose peak absorption is between 0.3 and 0.5 that of the zero field line. As the magnetic field increases, the broad band separates into distinct lines 0.1 to 0.2 as strong as the zero field line. Unfortunately, the channel spectra and lattice absorptions in the same frequency range overlap the Zeeman split electronic absorption lines and make the absorption spectra difficult to read. Nevertheless, absorption peaks can be located within $\pm 0.5 \text{ cm}^{-1}$ and have been plotted as a function of magnetic field in Figure 4.6. Four of the absorption peaks visible in the zero field spectra, those at 46.5, 57.6, 61.0, and 65.4 cm^{-1} , do not shift in the magnetic field and have been identified as either channel spectra or lattice absorptions. The 50.5 cm^{-1} lattice absorption, clearly visible in all of the Nd^{3+} spectra, is not visible at zero magnetic field in either the polarized or the unpolarized spectra of Er^{3+} in LaF_3 , but appears clearly above 20 kilogauss. These five constant frequency lines are denoted by horizontal dashed lines in

Figure 4.6: Zeeman splitting of Er^{3+} electronic transition in LaF_3

ZEEMAN SPLITTING OF Er^{3+} IN LaF_3

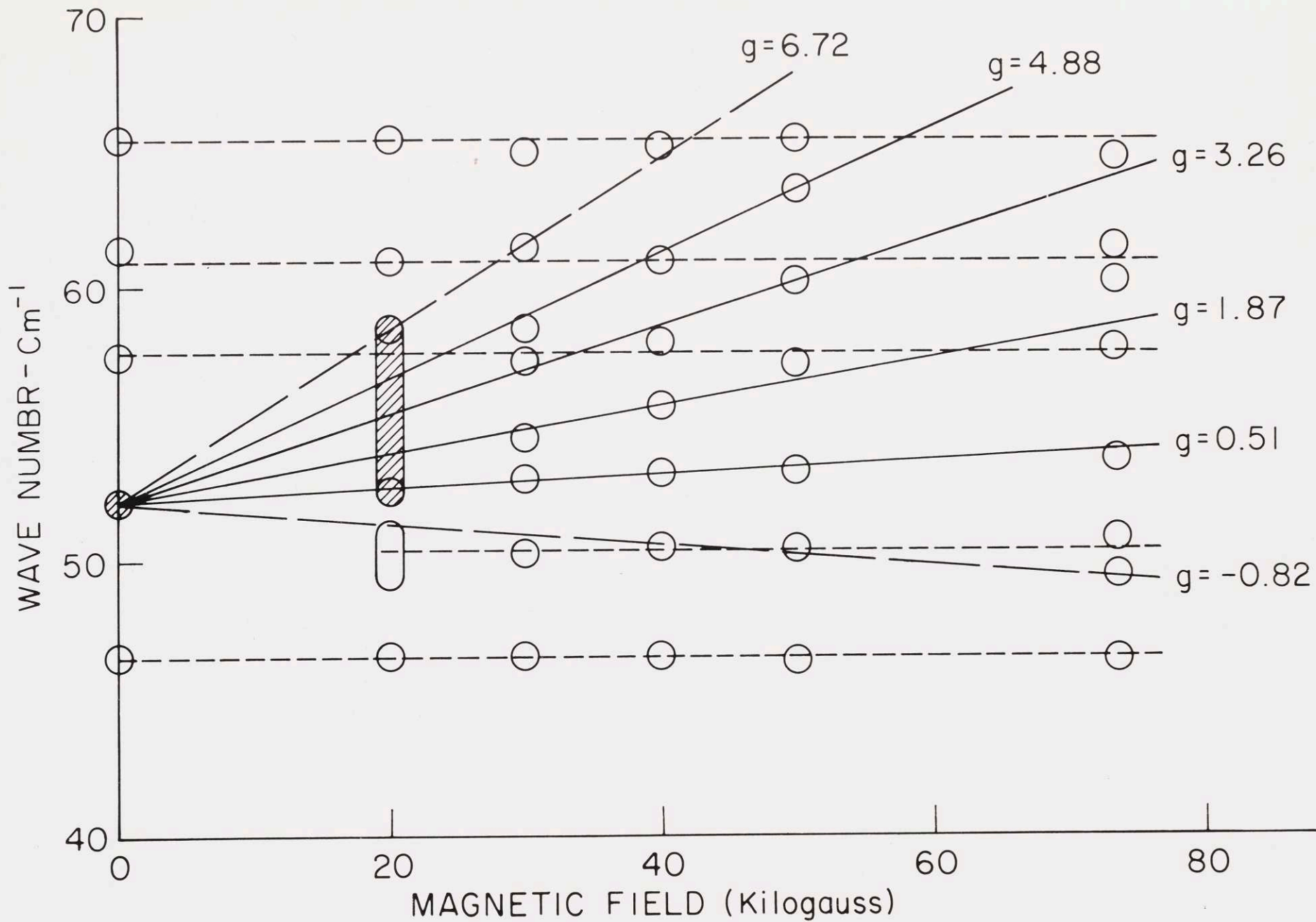


Figure 4.6. The other absorption peaks can be associated with the Zeeman transitions of Er^{3+} which all lie at 50.2 cm^{-1} in zero magnetic field. The four solid lines connect the absorption peaks of the unambiguously identified Zeeman transitions. The two broken lines indicate probable fifth and sixth Zeeman transitions.

The experimentally observed differences between the spectroscopic g -values of the ground state and the first excited state are calculated from the slopes of the six lines in Figure 4.6. Assuming that no significant Zeeman transitions have been missed, these differences range from -0.8 to $+6.7$. So many lines are resolved because the g -tensor of the ground state of Er^{3+} in LaF_3 (96) is strongly anisotropic. Unfortunately, a unique assignment of the g -tensor of the two lowest energy Stark levels is not possible based upon this one experiment because the sample is not well oriented and at least three different orientations would be necessary. Nevertheless, significant upper and lower bounds can still be stated. First, there are at least two and probably at least three magnetically distinguishable erbium sites. The maximum value of g for the excited Stark level in this orientation lies between 1.8 ± 0.2 and 7.5 ± 0.2 . The minimum value of g for the excited Stark level in this orientation lies between 3.5 ± 0.2 and 1.3 ± 0.2 . Finally, the g value of the excited state exceeds that of the ground state by

0.8 in at least one direction and is less than that of the ground state by 6.7 in the same direction for another erbium site.

The LaF_3 sample doped with one mole percent of Pr^{3+} is an unoriented single crystal used only in transmission. The PrF_3 sample is used only in reflection and is oriented with the magnetic field perpendicular to the optic axis and parallel to the face of the crystal. The infrared radiation is polarized with the electric field parallel to the optic axis. The operating temperature is between 1.0 and 1.7^oK and the instrumental slit width is approximately 2 cm^{-1} for all Pr^{3+} spectra.

Since the 4f wavefunction has integral spin, the $^3\text{H}_4$ ground multiplet of Pr^{3+} in tysonite is split into $2J + 1$ or nine non-degenerate Stark levels. Consequently, no first order Zeeman splitting is expected and the reflectance spectra do not change perceptibly in magnetic fields up to 150 kilogauss. Nevertheless, second order Zeeman effects are possible and the transmission spectra show a possible, very slight shift to higher frequencies (less than 1 cm^{-1} at 150 kilogauss) at very high field strengths. However, since the 66 cm^{-1} Pr^{3+} line is rather wide (approximately 3 cm^{-1}) and the transmittance spectra are quite noisy, the latter results are inconclusive.

Further studies of the possible second order magnetic properties of non degenerate Stark levels is not recommended until the far infrared instrumentation is greatly improved.

Studies of the first order Zeeman splitting of the Kramers doublet Stark levels, on the other hand, promise to be quite fruitful. Assuming that all of the Zeeman transitions could be resolved from one another, four oriented samples of each desired material will enable the complete g-tensor of both the ground Stark level and the excited Stark level to be completely specified. Because of the rather large values of g ($g_{\max} = 11$ for the ground state) and the strong anisotropy ($g_{\max}/g_{\min} = 11/3$ for the ground state), the g-tensor of the first excited state of Er^{3+} in tysonite may be rather easy to specify experimentally. Likewise, a Zeeman study of Dy^{3+} in tysonite might prove quite fruitful if it has an excited Stark level which is conveniently accessible.

4.9 Lanthanide Site in the Tysonite Space Group

It is unfortunate that ab initio calculations can not yet be made of the electronic eigenfunctions of the lanthanide ions in tysonite. Such calculations would undoubtedly resolve many of the apparent contradictions and difficulties found in the current literature on the tysonite lanthanide fluorides. Fortunately many of the selection rules governing electronic transitions can be calculated from group theoretical properties and a full MO-LCAO solution of the ligand fields is not always necessary.

Table 4.6 lists the permitted polarizations of electronic transitions and the number of magnetically distinguishable

TABLE 4.6

Permitted polarizations of electronic transitions
at the lanthanide sites
in the proposed tysonite lattices

Lattice space group	Formula units	Lanthanide site symmetry	Magnetically Distinguishable sites	Polarizations*	
				Integral J	Half-integral J
$P6_3/mmc$ (D_{6h}^4)	2	$\bar{6}m2$ (D_{3h})	1	π or σ or Forbidden	π or σ or $\pi\sigma$ or Forbidden
$P6_3/mcm$ (D_{6h}^3)	6	mm (C_{2v})	3	π or σ or Forbidden	all $\pi\sigma$
$P\bar{3}c1$ (D_{3d}^4)	6	2 (C_2)	3	σ or $\pi\sigma$	all $\pi\sigma$
$P6_3/22$ (D_6^6)	6	2 (C_2)	6	σ or $\pi\sigma$	all $\pi\sigma$
$P6_3/cm$ (C_{6v}^3)	6	m (C_s)	6	σ or $\pi\sigma$	all $\pi\sigma$
$P3c1$ (C_{3v}^3)	6	1 (C_1)	6	all $\pi\sigma$	all $\pi\sigma$

* $\pi = E||c$; $\sigma = E\perp c$; $\pi\sigma =$ unpolarized; Forbidden = some transitions have no electric dipole moment.

lanthanide sites for the space groups listed in Table 3.4.

Since the Nd^{3+} and Er^{3+} electronic transitions are observed to be unpolarized ($\pi\sigma$), only the bimolecular $P6_3/mmc$ (D_{6h}^4) structure can be eliminated by the polarized far infrared spectra of these ions. The Pr^{3+} electronic transitions, on the other hand, appear to be almost totally polarized (π or σ rather than $\pi\sigma$) as predicted for the hexagonal $P6_3/mcm$ (D_{6h}^3) structure. However, since the $66\text{-}69\text{ cm}^{-1}$ electronic transition of Pr^{3+} in PrF_3 (almost purely π -polarized) is also visible in the σ -polarization, the precise selection rules require unpolarized ($\pi\sigma$) electronic transitions. The most reasonable assumption is that the Pr^{3+} site is approximated by a slightly twisted pseudo-mm (C_{2v}) site as is found in the $\overline{P3}c1$ structure.

The Zeeman splitting of the Er^{3+} electronic transition reveals at least two and probably three magnetically distinguishable lanthanide sites. There is no conclusive evidence for more than three magnetically distinguishable lanthanide sites, but more are possible if the electronic transitions happen to be obscured by the strong channel spectra observed. Thus, the experimental results presented in this chapter are completely consistent with the trigonal $\overline{P3}c1$ structure proposed in Chapter III.

However, the magnetic resonance results reviewed earlier in this chapter consistently require six magnetically distinguishable

lanthanide sites. Therefore, they are inconsistent with either the hexagonal $P6_3/mcm$ or the trigonal $P\bar{3}cl$ structures. In a recent publication by R. P. Lowndes, J. F. Parrish, and C. H. Perry,⁽¹²⁰⁾ the authors proposed that this problem could be resolved by considering the properties of the 1651 Shubnikov groups⁽¹²¹⁻¹³⁰⁾ in which the anti-identity operator is associated with a reversal of the magnetic field. Table 4.7 lists significant properties of the six magnetic space groups associated with the conventional (Fedorov) $P\bar{3}cl$ lattice space group. To the extent that magnetic effects can be ignored, all of these magnetic space groups have identical electrical and mechanical properties. They are all magnetically ordered except the paramagnetic $P\bar{3}cl'$ structures. If the splitting of the Kramers degeneracy is assumed to be on the order of 100 gauss (approximately 0.02 cm^{-1}), the magnetically ordered $P\bar{3}'c'l$ and $P\bar{3}'cl$ structures are adequate to explain the magnetic resonance measurements and to reconcile them with the macroscopic properties of the tysonite lanthanide fluorides.

However, the assumption of a magnetically ordered crystal structure is not necessary. A much simpler explanation has been suggested by M. B. Schulz,⁽⁹⁷⁾ C. D. Jeffries,⁽⁹⁷⁾ and K. Lee.⁽¹⁰³⁾ They propose that the tysonite lanthanide fluorides have a multiply twinned $P\bar{3}cl'$ magnetic structure. The two halves of each twin is a horizontal mirror image of the other with

TABLE 4.7

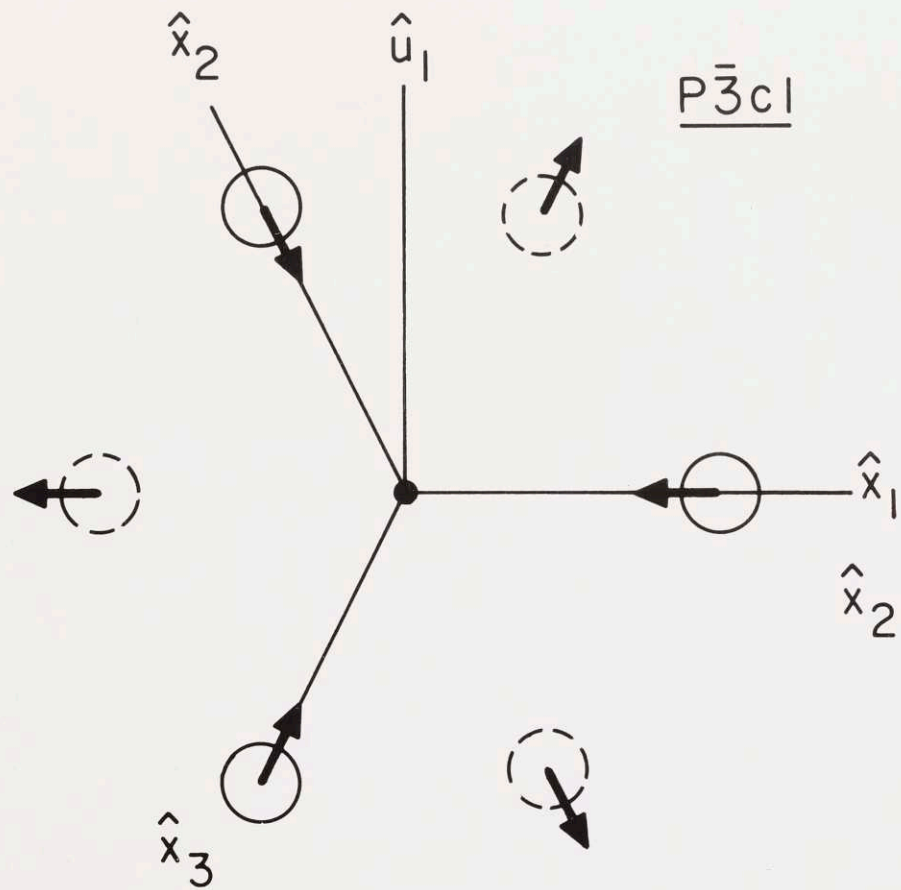
Group properties of the $P\bar{3}c1$ magnetic space groups

Magnetic space group	Magnetic crystal class	Number of Magnetically Distinguishable Lanthanide sites	Number of independent constants*		
			Pyro-magnetism $H_i = a_i T$	Magneto-electric Polarizability $H_i = a_{ij} E_j$	Piezo-magnetism $H_i = C_{ijk} \sigma_{jk}$
$P\bar{3}c1$	$\bar{3}m$	3	0	0	2
$P\bar{3}c1'$	$\bar{3}m1'$	3	0	0	0
$P\bar{3}'c1$	$\bar{3}'m$	6	0	1	0
$P\bar{3}'c'1$	$\bar{3}'m'$	6	0	2	0
$P\bar{3}c'1$	$\bar{3}m'$	3	1	0	4
$P_c \bar{3}c1$	$\bar{3}m$	†	0	0	2

* H_i = magnetic field; a_i = pyromagnetic tensor; T = temperature; a_{ij} = magnetoelectric polarizability; E_j = electric field; C_{ijk} = piezomagnetic tensor; σ_{jk} = stress tensor.

† See text. No proper magnetic representation for the atomic sites occupied in the tysonite lattice.

Figure 4.7: Magnetic ordering permitted in the $P\bar{3}c1$ and $P\bar{3}'c'1$ magnetic space groups.

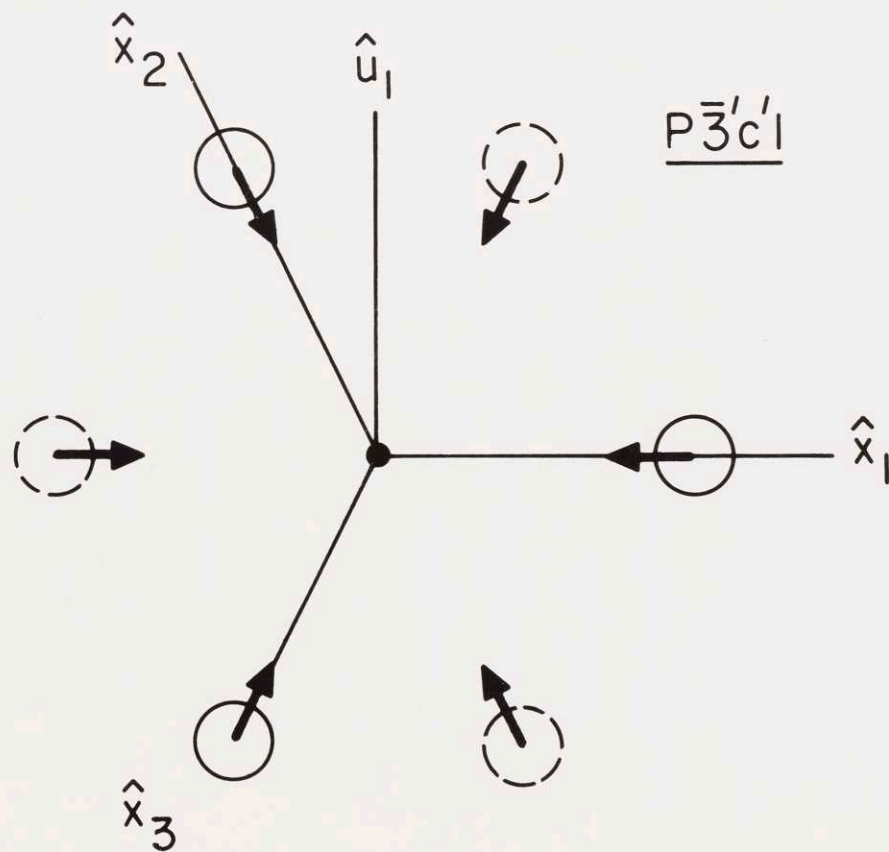


\bigcirc = LANTHANIDE ION
AT $z = + 1/4$

\bigcirc = LANTHANIDE ION
AT $z = -1/4$

\bullet = FLUORINE ION WITH
 D_3 SYMMETRY

\rightarrow = LOCAL INTERNAL
MAGNETIC FIELD



identical electrical and mechanical properties but with reversed magnetic properties. Their proposal is simple, in that it will apply to paramagnetic ions infinitely diluted in LaF_3 and sufficient, in that it will account for the ERP measurements of Eugene Y. Wong, Oscar M. Stafsudd, and David R. Johnston⁽¹¹⁵⁾ if one assumes that the optic axis is not quite perpendicular to the applied magnetic field in their measurements. The only problem remaining, if the structure is indeed a twinned $\overline{P3c1}$ lattice, is to explain how the slightly twisted pseudo-mm lanthanide site adequate for the Pr^{3+} spectra will predict the strongly twisted (45°) g-tensor of Nd^{3+} and Er^{3+} in LaF_3 . It is conceivable that the paramagnetic ions tend to pair, even when highly diluted by LaF_3 , resulting in a magnetic field independent splitting as found for the NMR of ^{19}F .⁽¹⁰³⁾ If so, the crystal may be both mechanically twinned and magnetically ordered over very short distances (approximately 1 nm).

CHAPTER V

SUMMARY

Since tysonite was first identified⁽¹³¹⁻¹³³⁾ in the 1880's, it and the other rare-earth fluorides have been subject to many different investigations. This thesis reviews most of the prior research and makes several new experimental contributions to understanding the tysonite fluorides of lanthanum, cerium, praseodymium, and neodymium. Moreover, the experimental study of the infrared properties of the tysonite lanthanide fluorides illustrate several experimental and theoretical problems associated with measuring uniaxial dielectric response functions.

The low temperature, far infrared reflectance of LaF_3 , CeF_3 , PrF_3 , and NdF_3 show five (possibly six) restrahlen peaks in the π -polarization ($E \parallel c$) and ten (possibly eleven) in the σ -polarization ($E \perp c$). A sixth, π -polarized, fundamental, infrared active, lattice mode is almost certainly located between 30 cm^{-1} and 40 cm^{-1} , but it is so weak that it has been observed only in transmission, so far. An eleventh, σ -polarized, fundamental infrared active, lattice mode is almost certainly located between 120 cm^{-1} and 130 cm^{-1} , but it is so weak that it has not been clearly observed in all four materials. The TO and LO frequencies of the fifteen strongest fundamental, infrared active, lattice modes at all three observation temperatures are listed in

Tables 3.1 for π -polarized modes and 3.2 for σ -polarized modes. Table 3.3 lists the two features tentatively identified as fundamental, infrared active, lattice modes along with several electronic transitions and spurious features due to the observation geometry.

The infrared active frequencies and the reported Raman active frequencies ⁽⁵⁴⁾ appear to be mutually exclusive implying that the tysonite space group includes the spatial inversion operator. The low temperature infrared results together with the low temperature Raman results identify 23 doubly degenerate and 11 nondegenerate fundamental lattice modes out of a total of 69 possible fundamental optical lattice modes at the center of the Brillouin zone of a crystal with six formula units of LaF_3 . This leaves only 12 nondegenerate, optically silent, lattice modes which have not been located. When correlated with all of the previous reports of the electrical and mechanical properties of the tysonite lanthanide fluorides, the most recent infrared results seem to be consistent only with the hexamolecular, trigonal-hexagonal, $\overline{\text{P3cl}}$ ($\text{D}_{3\text{d}}^4$) space group. At room temperature the fluorine ions with the lowest point group symmetry begin to migrate and the infrared results can be approximated reasonably well by a more symmetrical, hexagonal, $\text{P6}_3/\text{mcm}$ ($\text{D}_{6\text{h}}^3$) space group originally proposed by Oftedal. ⁽³⁹⁾

The selection rules of the far infrared electronic transitions of the non-Kramers ion of Pr^{3+} in the four tysonite host

lattices are approximated very well by the $mm (C_{2v})$ lanthanide site in the hexagonal $P6_3/mcm$ space group. However, the exact selection rules require a slight distortion from perfect mm site symmetry to either $2 (C_2)$ or $m (C_s)$ site symmetry. Unfortunately, infrared measurements can not yield sufficient detail to distinguish trigonal modifications from hexagonal modifications of the $P6_3/mcm$ structure.

The selection rules of the far infrared electronic transitions of the Kramers ions of Nd^{3+} and Er^{3+} in the four tysonite host lattices are consistent with any of the proposed space groups except the hexagonal $P6_3/mmc (D_{6h}^4)$ bimolecular pseudo-unit-cell structure. Moreover, the Zeeman splitting of the Nd^{3+} and Er^{3+} electronic transitions reveal conclusive evidence for at least two and probably three magnetically distinguishable lanthanide sites. Thus, the far infrared electronic spectra presented in this thesis are completely consistent with although they do not require an untwinned $\overline{P3}c1$ structure.

Magnetic resonance studies of LaF_3 doped with various paramagnetic lanthanide ions have consistently revealed six magnetically distinguishable lanthanide sites, whereas the $P6_3/mcm$ and the untwinned $\overline{P3}c1$ structures permit only three. Moreover, although the Zeeman spectra presented in this thesis reveal no more than three magnetically distinguishable lanthanide sites, some Zeeman transitions may have been missed and these results

do not conclusively forbid six magnetically distinguishable lanthanide sites. A multiply twinned $\overline{P3cl}$ crystal structure is the simplest explanation to reconcile the reported hexagonal magnetic resonance measurements with the trigonal $\overline{P3cl}$ crystal structure required by velocity of sound, X-ray diffraction, Raman, and infrared measurements.

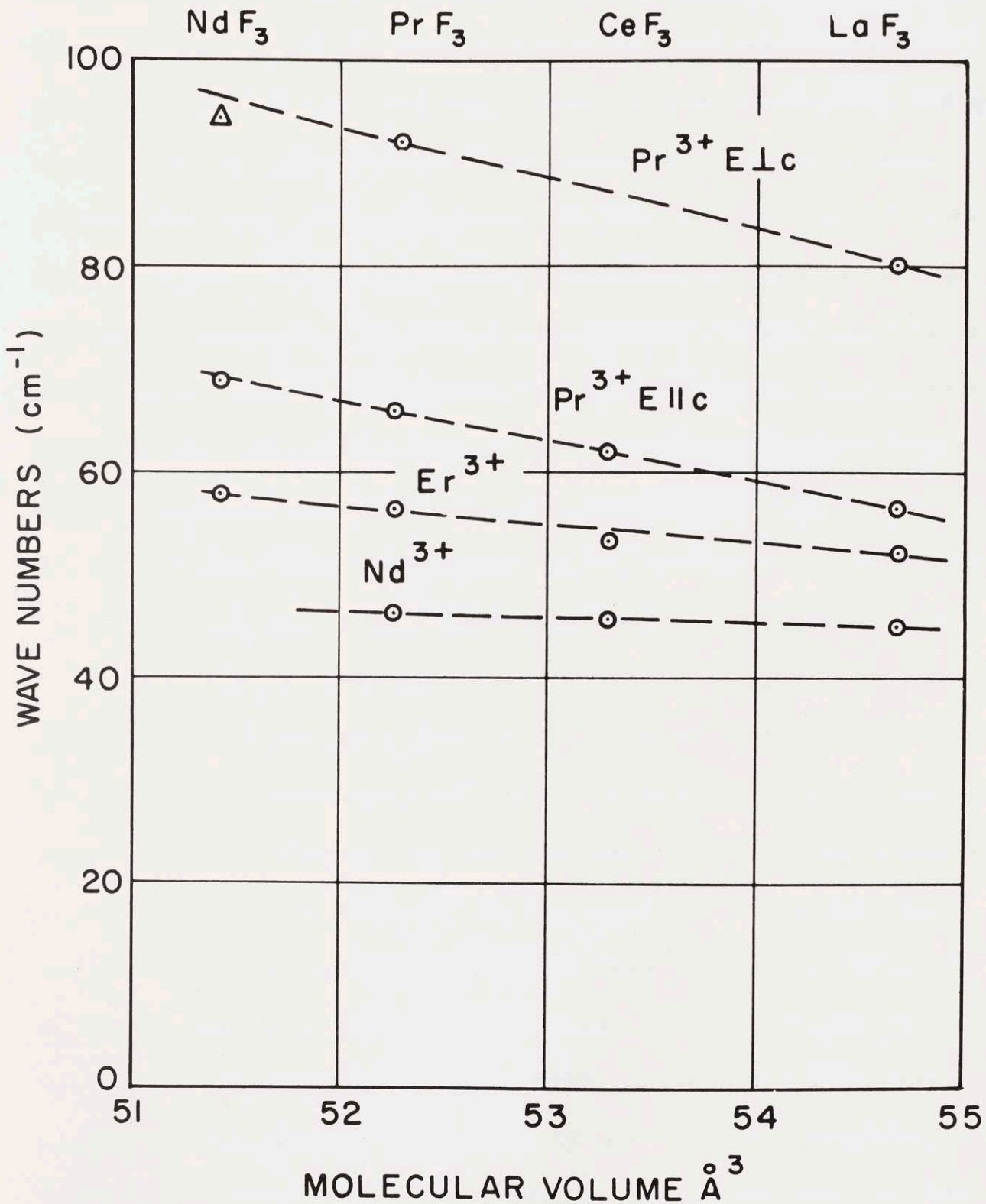
Figure 5.1 summarizes the electronic transition frequencies below 100 cm^{-1} as a function of host lattice. The higher frequency transitions vary faster but the variation does not seem to follow any simple power-law as a function of the lattice parameters. However, since the frequency changes are easily measurable, a further study of some of the other, higher frequency, electronic transitions as a function of the host lattice will enable one to determine both the values of the crystal field parameters and their variation as a function of interionic distances. These values and their variations could then be used to support or discredit some of the ligand field theories discussed in Chapter IV.

Two observations reported in this thesis were rather unexpected when first discovered in the spectra but were easily predicted in retrospect.

The electronic transitions below 100 cm^{-1} of Pr^{3+} in PrF_3 and to some extent of Nd^{3+} in NdF_3 are clearly visible in reflectance. When the electric dipole strengths of these

Figure 5.1: Frequencies of the Pr^{3+} , Nd^{3+} , and Er^{3+} electronic transitions below 100 cm^{-1} as a function of the tysonite host lattice.

ELECTRONIC TRANSITIONS
IN FOUR HOST LATTICES



electronic transitions observed in transmission in 1% concentrations are scaled up to 100% concentrations, one can easily show that near the transition frequency both the real and imaginary parts of the dielectric response function will be strongly affected and that the reflectance will change measurably. Nevertheless, other experimenters have attempted to observe these transitions only in transmission and have tacitly assumed that the electronic transitions were too weak to be observed in far infrared reststrahlen spectra. Perhaps this direct observation in reflectance of the moderately strong Pr^{3+} electronic transitions in PrF_3 will stimulate reflectance studies of the intermediate strength electronic transitions like Nd^{3+} in NdF_3 or the moderately weak, fundamental, infrared active, lattice mode transition between 30 cm^{-1} and 40 cm^{-1} in the π -polarization.

Some features characteristic of the LO (longitudinal optic) modes of the σ -polarized dielectric response function are clearly visible in the nominally π -polarized reflectance and transmittance spectra. Whereas one can show that a slight misalignment (less than five arc degrees) of the crystal's optic axis with respect to the polarizer or analyzer will lead to an absolute change in the value of the reflectance or transmittance of less than 1%, a corresponding misalignment of the optic axis with respect to the propagation vector of the infrared radiation forces the extraordinary dielectric response function (but not

the ordinary dielectric response function) to have zeros at all of the zeros of both the π -polarized and the σ -polarized dielectric response functions. The strengths of the zeros and their associated poles depend upon the angle between the optic axis and the propagation vector. For small angles, the strengths of the undesired poles and zeros are proportional to the square of the angle so that it is possible to minimize although not to completely eliminate these effects. However, the simple angular dependence of this effect makes it possible to conveniently eliminate probable spurious features from the π -polarized reflectance and transmittance spectra of conventionally oriented samples. Moreover, by deliberately misaligning the optic axis of a sample so that it is not quite perpendicular or parallel to the propagation vector and observing only the extraordinary dielectric response function, it is possible to study in transmission some strongly infrared active LO modes as if they were weak TO resonances in the orthogonally polarized dielectric response function.

REFERENCES

1. L.F. Johnson, J. Appl. Phys., 34, 897(1963).
2. W.F. Krupke and J. B. Gruber, J. Chem. Phys., 41, 1225(1964).
3. G. Hass, J.B. Ramsey, and R. Thun, J. Opt. Soc. Am., 49, 116(1959).
4. J.B. Mooney, Infrared Physics, 6, 153(1966).
5. Optovac, Inc., North Brookfield, Massachusetts.
6. C.H. Perry, R. Geick, and E.F. Young, Appl. Opt., 5, 1171 (1966).
7. L. Mertz, Transformations in Optics, Wiley, (1965).
8. L. Mertz, Infrared Physics, 7, 17(1967).
9. D.R. Bosomworth and H.P. Gush, Can. J. Phys., 43, 729(1965).
10. J.F. Parrish, Quarterly Progress Report, 90, Research Laboratory of Electronics, M.I.T., pp 37-45; also QPR, 91, p. 47.
11. P.M. Morse and H. Feshbach, Methods of Theoretical Physics, McGraw-Hill Book Company, Inc. New York, 1953, p. 372.
12. E.A. Guillemin, Synthesis of Passive Networks, John Wiley and Sons, New York, 1957, p. 303.
13. G. Andermann, A. Caron, and David A. Dows, J. Opt. Soc. Am., 55, 1210(1965).
14. D.M. Roessler, Brit. J. Appl. Phys., 16, 1119(1965).
15. D.M. Roessler, Brit. J. Appl. Phys., 16, 1359(1965).
16. D.W. Berreman, Appl. Opt., 6, 1519(1967).
17. D.W. Berreman and F.C. Unterwald, Phys. Rev., 174, 791(1968).
18. J.M. Ziman, Principles of the Theory of Solids, Cambridge University Press, 1964.

19. C. Kittel, Introduction to Solid State Physics, John Wiley and Sons, Inc., New York, 1966.
20. A.S. Barker, Jr., "Infrared Dielectric Behavior of Ferroelectric Crystals", Ferroelectricity, ed. E.F. Weller, Elsevier Publishing Company, Amsterdam, 1967, pp 213-250.
21. A.S. Barker, Jr., Phys. Rev. 136, A1290(1964).
22. A.S. Barker, Jr., and J.J. Hopfield, Phys. Rev., 135, A1732 (1964).
23. R. Geick and C. H. Perry, "Analysis of Reflection Spectra by means of a fit with a Classical Dispersion Formula", Quarterly Progress Report, 77, Research Laboratory of Electronics, M.I.T., pp. 41-48 (15 April 1965).
24. R.A. Smith, F.E. Jones, and R.P. Chasmar, The Detection and Measurement of Infra-Red Radiation, Oxford University Press, Amen House, London, 1957, pp. 380-385.
25. C. Christiansen, Annalen der Physik und Chemie, 259, 298 (1884).
26. C. Christiansen, Annalen der Physik und Chemie, 260, 439 (1885).
27. M. Born and E. Wolf, Principles of Optics, The Macmillan Company (Pergamon Press), New York, 1964.
28. M.A. El'yashevich, Spektry Redkikh Zemel, Gosudarstvennoe Izdatel'stvo Tekhniko-Teoreticheskoi Literatury, Moskva, 1953. Spectra of the Rare Earths, State Publishing House of Technical-Theoretical Literature, Moscow, 1953. U.S. Atomic Energy Commission translation AEC-tr-4403, Office of Technical Services, Department of Commerce, Washington, D.C., April, 1961.
29. F.H. Spedding and A.H. Daane, ed. The Rare Earths, John Wiley and Sons, Inc., New York, 1961.
30. B.G. Wybourne, Spectroscopic Properties of Rare Earths, Interscience Publishers (Div. John Wiley and Sons, Inc.) New York, 1965.
31. H.M. Crosswhite and H.W. Moos, eds. Optical Properties of Ions in Crystals, Interscience Publishers, New York, 1967

32. D. Brown, Halides of the Transition Elements, V. 1; Halides of the Lanthanides and Actinides, John Wiley and Sons, Ltd., London, 1968.
33. A.F. Wells, Structural Inorganic Chemistry, Oxford University Press, Amen House, London E.C. 4, 1962.
34. I. Oftedal, Z. Physik, Chem., 5B, 272(1929).
35. A. Zalkin and D.H. Templeton, J. Am. Chem. Soc., 75, 2453 (1953).
36. R.E. Thoma and G.D. Brunton, Inorg. Chem., 5, 1937(1966).
37. O.N. Carlson and F.A. Schmidt, "Preparation of the Rare-Earth Fluorides", The Rare Earths, ed. F.H. Spedding and A.H. Daane, John Wiley and Sons, Inc., New York, 1961, pp. 77-88.
38. A. Sher, R. Solomon, K. Lee, and W.M. Muller, Phys. Rev., 144, 593(1966).
39. I. Oftedal, Z. Physik, Chem., 13B, 190(1931).
40. K. Schlyter, Arkiv. Kemi, 5, 73(1953).
41. E. Staritzky and L.B. Asprey, Anal. Chem., 29, 856(1957).
42. H.E. Swanson, N.T. Gilfrich and G.M. Ugrinic, Standard X-Ray Diffraction Powder Patterns, 5, National Bureau of Standards, Circular 539, p. 52 (October 21, 1955).
43. H.E. Swanson, N. T. Gilfrich, and M.I. Cook, Standard X-Ray Diffraction Powder Patterns, 7, National Bureau of Standards, Circular 539, p. 21 (September 27, 1957).
44. H.E. Swanson, N.T. Gilfrich, M.I. Cook, R. Stinchfield and P.C. Parks, Standard X-ray Diffraction Powder Patterns, 8, National Bureau of Standards, pp 17-18 (1 April 1959).
45. H.E. Swanson, et al., Standard X-ray Diffraction Powder Patterns, 8, National Bureau of Standards, p. 36 (1 April 1959).
46. M. Mansmann, Z. Anorg. Allgem. Chem., 331, 98(1964).
47. M. Mansmann, Z. Krist., 122, 375(1965).

48. A. Zalkin, D.H. Templeton and T.E. Hopkins, Inorg. Chem., 5, 1466(1968).
49. M. Mansmann and W.E. Wallace, Journal de Physique, 25, 454 (1964).
50. C. deRango, G. Tsoucaris, C. Zelwer, C. R. Acad. Sc. Paris, 263C, 64(1966).
51. G.G. Koerber, Properties of Solids, Prentice-Hall, Inc., Englewood Cliffs, New Jersey, 1962.
52. C. Krischer, Appl. Phys. Letters, 3, 310(1968).
53. H.H. Caspers, R.A. Buchanan, and H.R. Marlin, J. Chem. Phys., 41, 94(1964).
54. R.P. Bauman and S.P.S. Porto, Phys. Rev., 161, 842(1967).
55. H.E. Rast, H.H. Caspers, S.A. Miller, and R.A. Buchanan, Phys. Rev., 171, 1051(1968).
56. E.U. Condon, G.H. Shortley, The Theory of Atomic Spectra, Cambridge University Press, 1935. Reprinted New York, 1967.
57. G.D. Jones and R.A. Satten, Phys. Rev., 147, 566(1966).
58. N.F.M. Henry and K. Lonsdale, eds., International Tables for X-ray Crystallography, Vol. I. Symmetry Groups, The Kynoch Press, Birmingham, England, 1965.
59. M. Goeppert Mayer, Phys. Rev., 60, 184(1941).
60. R. Latter, Phys. Rev., 99, 510(1955).
61. C.A. Coulson and C.S. Sharma, Proc. Phys. Soc., 79, 920(1962).
62. B. Bleaney, P.M. Llewellyn, and D.A. Jones, Proc. Phys. Soc., 69B, 858(1956).
63. B.G. Wybourne, J. Chem. Phys., 32, 639(1960).
64. E.Y. Wong, J. Chem. Phys., 35, 544(1961).
65. H.H. Caspers, S.A. Miller, H.E. Rast, and J.L. Fry, Phys. Rev., 180, 329(1969).

66. A.Kiel, T. Damen, S.P.S. Porto, S. Singh, F. Varsanyi, Phys. Rev., 178, 1518(1969).
67. J.A. Koningstein and O.S. Mortensen, Nature, 217, 445(1968).
68. J.A. Koningstein, J. Chem. Phys., 46, 2811(1967).
69. J.A. Koningstein and O. S. Mortensen, Phys. Rev. Letters, 18, 831(1967).
70. J.A. Koningstein, J. Opt. Soc. Am., 56, 1405(1966).
71. J.Y.H. Chau, J. Chem. Phys., 44, 1708(1966).
72. J.T. Hougen and S. Singh, Proc. Roy. Soc. (Lon.), A277, 193(1964).
73. R.J. Elliott and R. Loudon, Phys. Letters, 3, 189(1963).
74. E.Y. Wong, O.M. Stafsudd, and D.R. Johnston, J. Chem. Phys., 39, 786(1963).
75. J. D. Jackson, Classical Electrodynamics, John Wiley and Sons, Inc., New York, 1962.
76. M.T. Hutchings and C.K. Ray, Proc. Phys. Soc., 81, 663(1963).
77. G. Burns, Phys. Rev., 128, 2121(1962).
78. R.E. Watson and A.J. Freeman, Phys. Rev., 133, A1571(1964).
79. D.K. Ray, Proc. Phys. Soc., 82, 47(1963).
80. C.J. Lenander and E.Y. Wong, J. Chem. Phys., 38, 2750(1963).
81. B. Bleaney, Proc. Roy. Soc. (Lon.), A277, 289(1964).
82. G. Burns, J. Chem. Phys., 42, 377(1965).
83. M.M. Ellis and D.J. Newman, J. Chem. Phys., 47, 1986(1967).
84. S.S. Bishton, M.M. Ellis, D.J. Newman, and J. Smith, J. Chem. Phys., 47, 4133(1967).
85. M.M. Ellis and D.J. Newman, J. Chem. Phys., 49, 4037(1968).
86. M.M. Curtis, D.J. Newman, and G.E. Stedman, J. Chem. Phys., 50, 1077(1969).

87. C. K. Jørgensen, R. Pappalardo, and H-H Schmidtke, J. Chem. Phys., 39, 1422(1963).
88. C.E. Schäffer and Chr. K. Jørgensen, Molecular Physics, 9, 401(1965).
89. H.E. Rast and H.H. Caspers, "Fluorescence and Infrared Absorption of Sm^{3+} in LaF_3 ", NOLC Report 672, pp 1-29, (April-June 1966).
90. R.A. Buchanan, H.E. Rast, and H.H. Caspers, J. Chem. Phys., 44, 4063(1966).
91. D.A. Jones, J.M. Baker, and D.F.D. Pope, Proc. Phys. Soc. 74, 249(1959).
92. H.E. Rast, H.H. Caspers, and S.A. Miller, J. Chem. Phys., 47, 3874(1967).
93. J.H. Van Vleck and M. H. Hebb, Phys. Rev., 46, 17(1934).
94. H.A. Kramers, Proc. Acad. Sci. Amst., 36, 17(1933).
95. J. Becquerel, W.J. deHaas, J. van den Handel, Physica, 1, 383(1934).
96. J.M. Baker and R.S. Rubins, Proc. Phys. Soc., 78, 1353(1961).
97. M.B. Schulz and C.D. Jeffries, Phys. Rev., 149, 270(1966).
98. V. Saraswati and R. Vijayaraghavan, Phys. Letters, 21, 363 (1966).
99. V. Saraswati and R. Vijayaraghavan, J. Phys. Chem. Solids, 28, 2111(1967).
100. K. Lee and A. Sher, Phys. Rev. Letters, 14, 1027(1965).
101. L. Shen, Phys. Rev., 172, 259(1968).
102. M. Goldman and L. Shen, Phys. Rev., 144, 321(1966).
103. K. Lee, Solid State Communications, 7, 367(1969).
104. A.G. Lundin, S.P. Gabuda, and A.I. Lifshits, Soviet Physics-Solid State, 8, 1495(1966) from Fizika Tverdogo Tela, 8, 1889(1966).

105. A.G. Lundin, S.P. Gabuda, and A.I. Lifshits, Soviet Physics-Solid State, 9, 273(1967) from Fizika Tverdogo Tela, 9, 357(1967).
106. K. Lee, "BD3. Temperature Dependence of F^{19} NMR in CeF_3 ", Bulletin of the American Physical Society, 11, 718(1966).
107. K. Lee and A. Sher, Phys. Rev., 150, 168(1966).
108. L.O. Andersson and W.G. Proctor, Helvetica Physica Acta, 38, 360(1965).
109. E.V. Sayre and S. Freed, J. Chem. Phys., 23, 2066(1955).
110. W.M. Yen, W. C. Scott, and A. L. Schawlow, Phys. Rev., 136, A271(1964).
111. H.H. Caspers, H.E. Rast, and R.A. Buchanan, J. Chem. Phys., 43, 2124(1965).
112. R.A. Buchanan and M.A. Butler, NAVWEPS 8852, pp 33-44, (Jan-Mar 1966).
113. A. Hadni, P. Strimer, C. R. Acad. Sc. Paris, 265B, 811(1967).
114. Y.K. Chow, Z. Phys., 124, 52(1947).
115. E.Y. Wong, O.M. Stafsudd, D. R. Johnston, Phys. Rev., 131, 990(1963).
116. H.H. Caspers, H.E. Rast, and R.A. Buchanan, J. Chem. Phys., 42, 3214(1965).
117. C.K. Asawa and M. Robinson, Phys. Rev., 141, 251(1966).
118. S.A. Johnson, H.G. Freie, A.L. Schawlow, W.M. Yen, J. Opt. Soc. Am., 57, 734(1967).
119. W.F. Krupke, J. B. Gruber, J. Chem. Phys., 39, 1024(1963).
120. R.P. Lowndes, J.F. Parrish, and C.H. Perry, Phys. Rev., 182, 913(1969).
121. N.V. Belov, N.N. Neronova, and T.S. Smirnova, Soviet Physics--Crystallography, 2, 311(1957). Translation of Kristallograffia, 2, 306(1957).
122. A.M. Zamorzaev, Soviet Physics-Crystallography, 2, 10 (1957). Translation of Kristallograffia, 2, 15(1957).

123. A.M. Zamorzaev and E.I. Sokolov, Soviet Physics-Crystallography, 2, 5(1957). Translation of Kristallograffia, 2, 9(1957).
124. R. R. Birss, Proc. Phys. Soc., 79, 946(1962).
125. S. Bhagavantam and P. V. Pantulu, Proc. Indian Acad. of Sciences, 59, 1(1964).
126. S. Bhagavantam and P. V. Pantulu, Proc. of the Indian Acad. of Sciences, 63, 391(1966).
127. A.P. Cracknell, Advances in Physics, 17, 367(1968).
128. A.P. Cracknell, Proc. Camb. Phil. Soc., 65, 567(1969).
129. A.P. Cracknell, J. Physics. C, 2, 500(1969).
130. E.P. Wigner, Group Theory and its Application to the Quantum Mechanics of Atomic Spectra, trans. by J.J. Griffin (from german), Academic Press, New York and London, 1959.
131. O.D. Allen and W.J. Comstock, The Amer. J. of Sci., 119, 390(1880).
132. E.S. Dana, The Amer. J. of Sci., 127, 479(1884).
133. E.S. Dana, Zeitschrift für Krystallographie und Mineralogie, 9, 283(1884).

BIOGRAPHICAL NOTE

John Frederic Parrish was born on 14 January 1943 in Los Angeles, California. He graduated with honors from Buena Park High School, Buena Park, California in June 1960. He attended Loyola University of Los Angeles, Los Angeles, California from September 1960 to June 1964. While there he was a member of the Honors Program and elected to membership in Alpha Sigma Nu, the Jesuit college scholastic honor fraternity. He attended Massachusetts Institute of Technology, Cambridge, Massachusetts from September 1964 to September 1969. He was awarded a National Science Foundation Graduate Fellowship from September 1964 to September 1968. He was elected to associate membership in the Sigma Xi in April 1967 and full membership in April 1968.

Degrees: Bachelor of Science (B.S.) in Physics,
 Magna Cum Laude, in June 1964 from
 Loyola University of Los Angeles
 Los Angeles, California

 Master of Science (S.M.) in Physics,
 in June 1967 from
 Massachusetts Institute of Technology
 Cambridge, Massachusetts

S.M. Thesis title: "Lattice Vibrational Spectra of Several Mixed Crystals of CdS and CdSe.

Internal Publications of the Research Laboratory of Electronics, M.I.T.:

J. F. Parrish and C. H. Perry, "Lattice Vibrations in CdS/Se Mixed Crystals". QPR 85, (15 April 1967), pp 42-47.

J. F. Parrish and C. H. Perry, "Optical Phonons in CdS_xSe_{1-x} Mixed Crystals". QPR 87, (15 Oct 1967), pp. 25-35.^{1-x}

J. F. Parrish, "On the Dielectric Response Function". QPR 90, (15 July 1968), pp. 37-45. QPR 91, (15 Oct 1968), p. 47.

R. P. Lowndes, J. F. Parrish, and C. H. Perry, "Optical Phonons and Symmetry of Tysonite Lanthanide Fluorides". QPR 92, (15 January 1969), pp. 92-110.

J. F. Parrish, R. P. Lowndes, and C. H. Perry, "Far Infrared Electronic Transitions in Tysonite Lanthanide Fluorides". QPR 92, (15 January 1969), pp. 110-116.

External Publications:

J.F. Parrish, C.H. Perry, O. Brafman, I.F. Chang, and S.S. Mitra, "Phonons in Mixed-Crystal System CdS_xSe_{1-x}". II-VI Semi-conducting Compounds: 1967 International Conference, ed. by D. G. Thomas, W. A. Benjamin, Inc., New York, 1967, pp. 1164-1184.

J.F. Parrish, R.P. Lowndes, and C.H. Perry, "Far Infrared Electronic and Vibronic Transitions of Nd³⁺ in the Tysonite Lanthanide Fluorides". Physics Letters, 29A, (21 April 1969), pp. 133-134.
Also in Physics Letters, 29A, (19 May 1969), pp. 270-271.

R.P. Lowndes, J.F. Parrish, and C.H. Perry. "Optical Phonons and Symmetry of Tysonite Lanthanide Fluorides". Physical Review, 182, (15 June 1969) pp. 913-922.